MSc thesis APPLIED MATHEMATICS

"Physics based modelling of the impact of Unicom settings on the illumination pupils of EUV lithography machines"

TIM KLIJNJAN

ASML & Delft University of Technology

Supervisors

J. Tan (ASML) Dr. N. Budko (TUD)

January, 2024 Veldhoven

Abstract

Extreme Ultraviolet lithography is a vital step in the production of cutting edge computer chips that drive emergent technologies like AI, VR and the internet of things [1]. Careful control of Ultraviolet light beams by EUV machine modules such as the Unicom, Uniformity correction module, enable extremely precise printing of nano-scale structures on these chips.

This thesis focuses on the construction of a model that predicts the impact of the Unicom on EUV illumination in ASML's lithography machines. Such a model could be used in a predictive maintenance scheme to prevent a fraction of unscheduled machine downtime, which can be estimated to cost ASML's customers around 38 million dollars per machine per year [2–4]. Similar problems have been tackled before [5, 6], but both existing models disregard multiple properties of the EUV machine and are incompatible with the type of measurements obtained by ASML. Therefore, the question remains how an accurate Unicom model can be constructed.

In this thesis, a physics based Unicom model was developed that can be fine-tuned to machine specific measurements. Significant reductions of up to 90.3% of prediction errors were obtained by using the model. Overall, making use of the model provided better or equivalent predictions when compared to not using the model for all but one of the investigated indicators of prediction quality. For the latter indicator errors remained within the desired bound, but further investigation is needed to discover why the Unicom model adversely affected this indicator. With an average execution time of 31.4 s, the created Unicom model in general enables swift and substantial accuracy gains.

Contents

1 Notation

Table 1 contains an overview of some abbreviations and notation introduced in this thesis. To illustrate subscripts and superscripts a dummy variable A is used.

EUV	Extreme Ultra Violet
DUV	Deep Ultra Violet
Unicom	Uniformity correction module
WL	Wafer Level
RL	Reticle Level
UL	Unicom Level
FFI	Field Facet Image

$\mathbb{I}$	static bitmap intensities
$\mathbb{J}$	y-integrated bitmap intensities
$\mathbb{j}$	y-integrated parcellated intensities
$\mathcal{M}$	static Unicom model
${}_{\mathcal{M}}A$	A calculated from output of $\mathcal{M}$ without additional data
A^*	A obtained from a scanning measurement
$A^\perp$	A is normalized
$\mathbf{d}$	vector with y-positions of all Unicom fingers
$A^{\mathbf{0}}$	A with all Unicom fingers extracted
$A^{\mathbf{d}}$	A with all Unicom fingers positioned according to $\mathbf{d}$
A^u	A at UL
A^r	A at RL
$A^\odot$	A at the center of the pupil

Table 1: Some abbreviations and notation introduced in this thesis.

2 Introduction

Through time, advances in technology have increased living standards around the globe. Recently, a lot of big advances have been and will continue to be made within the area of computing: Artificial Intelligence, AI, has been a very hot topic for the past few years; Virtual and Augmented Reality promise to immerse people into enhanced experiences of the world and through the internet of things, devices become smarter by communicating with one another [1]. Increased demand for computing power means there is a need for ever more powerful and thus more complex chips to perform the computational tasks. These chips consist of billions of transistors, electrical components that act as switches by blocking current when switched off or letting current pass when switched on. Transistors are made using photolithography, an optical printing method that uses light to create images. The EUV, Extreme Ultra Violet, lithography machines of ASML form an essential part in the chain of production for these complex chips. Hence, improving the capabilities of the EUV machine will enable the creation of innovative new computing technologies and in doing so change lives everywhere.

To improve EUV machine capabilities, this thesis first investigates the way the machine works and subsequently seeks to improve that process. Since the EUV machines are vastly complex, the scope of the thesis is to create a model capable of predicting the optical effects of one of the modules in the machine: the Uniformity correction module, or Unicom. For the printing step performed by EUV machines it is important that the bundle of light that ends up at the wafer on which a chip is printed, contains a precise image of the structures that need to be printed. To create these precise images, the light bundle needs to have uniform intensity when it hits the reticle, object of which an image is created. The Unicom exists to ensure that the required uniformity can be achieved by the machine. Creating an optical Unicom model will enable better understanding of the impact the Unicom's settings have on the light that arrives at the wafer. This opens the door to accurate real time monitoring of the light that hits the reticle in EUV machines and aids in predicting when machine maintenance is needed. As costs due to unscheduled machine downtime for customers can be estimated to be 38 million dollars per machine per year [2–4] the value of preventing even a fraction of the downtime becomes apparent. Additionally, insight into the effects of the Unicom can be used to improve multiple measurement and calibration routines that in turn would increase a machine's production and precision.

The Unicom model constructed in this thesis seeks to combine knowledge of the EUV machine's design with geometrical optics and fine tuning based on measurement data. Validation of the model's accuracy is performed by comparing model predictions to measurements. Although some previous works on modeling modules similar to the Unicom exist [5, 6], the existing models tackle problems that do not accurately account for how the EUV machine physically works. Furthermore, the measurements available for EUV machines differ from information assumed known by these existing models. Therefore, a novel model is constructed.

Because a part of the machine's design as well as the collections of measurement data are secret intellectual property of ASML, certain values and geometries presented here are only to serve as an example and deviate from reality. For this reason, this thesis also does not contain visualizations the pupils and slits outputted by the model, which were consulted regularly during model setup and validation. However, the examples presented still illustrate the way the model works. Furthermore, values presented to indicate the model's performance still concern the real model for the actual design and data.

In Chapter 1 of this thesis a table with notation is presented to aid the reader in subsequent chapters. The current chapter introduces the general goal of the thesis and provides a social context to the problem at hand. Chapter 3 is concerned with the theory of the photolithographic process and the EUV machine. This theory is used in Chapter 4 to elaborate on the business case for a Unicom model, further specify the goal for the model to construct in this thesis and discuss existing literature. Chapter 5 is where the building blocks of the model are explained and choices in the setup of the model are elaborated upon. Chapter 6 presents and discusses the performance of the model, which is assessed by comparing to machine measurements. In Chapter 7 a recap of the thesis's results is presented accompanied by conclusions and some directions for future research are suggested.

3 Photolithography theory

In this chapter theory regarding the photolithography process will be presented. First, how the lithography step fits into the general process of producing computer chips is explained. After this general overview, key optical requirements to make lithography possible are presented within the context of physics. Subsequently, these physical requirements are connected to concepts within ASML's EUV lithography systems. Along the way, an already established simulators will be introduced. This chapter is concluded by elaborating upon measurement routines which supplied the data used to construct the Unicom model and in which the Unicom model could be integrated in the future. The exact goal of this thesis will be stated in Chapter 4 using the definitions presented in the current chapter.

This thesis is concerned only with modeling the impact of a single module of ASML's EUV lithography systems called the Unicom on the quality of machine output. However, it is essential to know how other parts of the EUV machine work to understand in what ways the Unicom might impact machine and thereby chip manufacturing performance. The information in this chapter will be EUV specific, but EUV processes in part build upon DUV, Deep Ultra Violet, technologies and thus might share some commonalities.

3.1 Principles of photolithography

Although the process of photolithography is not used exclusively during the process of manufacturing computer chips, in this thesis the lithography step will only be considered within the context of producing these chips. Manufacturing chips is by far the biggest use case of photolithography and although the context may be different when producing for instance MEMS, micro-electromechanical systems, the lithography step itself stays largely the same [7].

Lithography in chip production

The production of integrated circuits, also called ICs or chips, is a complex technical process involving many steps, one of which is lithography. An example of what the manufacturing process might look like depending on a chip's design, as can be seen in Figure 3.1.

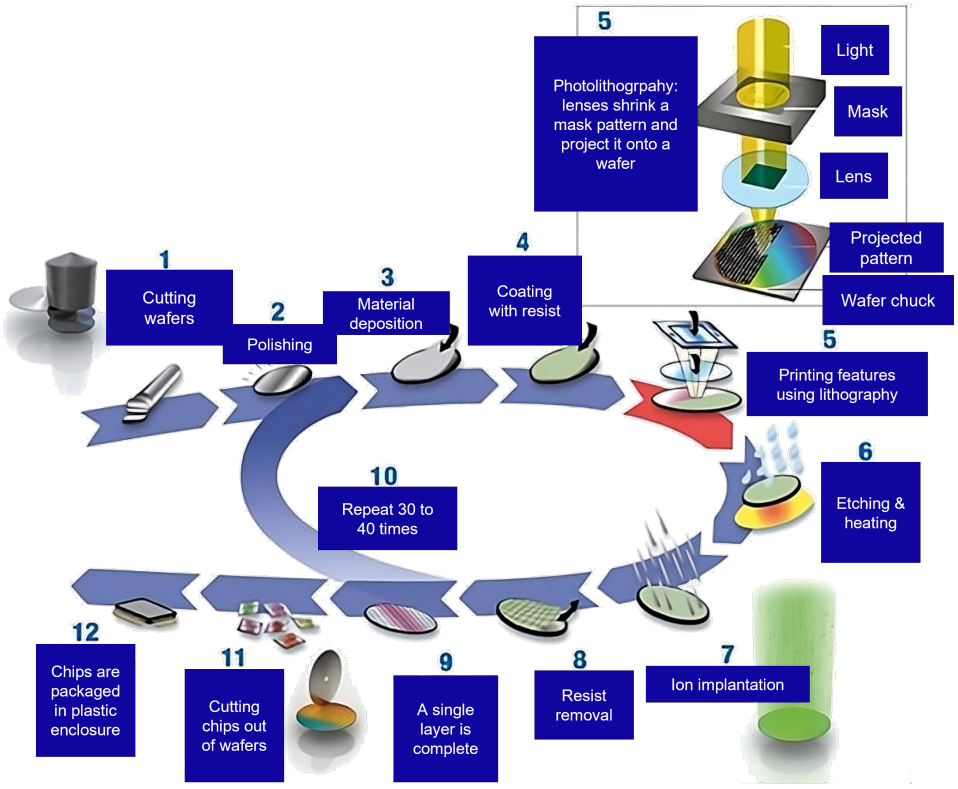

Fig. 3.1: Example of the manufacturing process of a chip. Adapted from [8].

Chips are printed on disks, called wafers, which are most often made from silicon crystals. To build chips, materials are deposited layer by layer onto the wafer. Right before the lithography step these wafers are coated a chemical substance called resist. The lithography step prints the design patterns for a chip's structures in this resist, enabling the coordinated removal of a part of the resist. The remaining resist protects the area of the wafer below it during a subsequent step like etching. The etching step removes the unprotected part of the layer that was deposited onto the wafer the wafer was coated with the resist.

Building the 3D structure of a chip layer by layer requires multiple printing runs over the same area, many of which require a lithography step. This repeated need for the complex lithography step accounts for a large part of the manufacturing costs of ICs. Furthermore, the need for lithography means that bottlenecks can occur in the chip production process when the number of wafers (layers) a lithography machine can process per hour is low. Hence, next to increasing the accuracy of lithography machines, increasing throughput of these machines is of paramount importance to ASML's customers. To achieve both goals it is important to understand how a lithography machine works and how optical properties of the system are closely intertwined with the pattern printed in the resist.

Printing in resist

Critical to the output of the lithography machine is the resist. Resist changes in chemical properties when the amount of light that is projected onto the resist supersedes a certain threshold. The amount of light that ends up on a part of the resist is called the dose: $D(x, y) = \int I(x, y, t)\, dt$, where $D(x, y)$ is the dose in J/m^2 received by point (x, y) of the resist and $I(x, y, t)$ is the intensity of the light incident on that point of the resist in W/m^2 at any specific time t. When the intensity is constant over time the dose is simply given by $D(x, y) = I(x, y) \cdot T$ with T the total exposure time of the resist to the temporally constant intensity $I(x, y)$. The intensity $I(x, y, t)$ ending up at the resist is commonly called the aerial image.

Since a resist layer has a certain thickness, just below the threshold there exists a range of dosage for which the resist layer is chemically changed only to a certain depth. This effect of partial chemical change is usually quite complex, depending on various properties of the type of resist that is used. However, in this chapter the transition between partial and complete exposure will be depicted as linear since this eases the explanation of key concepts within lithography. Two common types of resist are positive and negative resist, meaning that crossing the dose threshold will either chemically soften or harden the resist respectively. Subsequently, the soft parts of the resist can be removed during a process called development to leave a protective layer on a deliberately selected part of the wafer.

ICs contain structures comprised of very small patterns, called features. Modern chips like those produced using TSMC's $3nm$ node (manufacturing processes are also called nodes), use features close to $24nm$ according to predictions made in [9]. Admittedly, the $24nm$ is larger than the marketing term for the node, but this is still approximately 3000 times smaller than the width of a human hair. The reason that tiny features are desirable is that smaller structures can be packed to higher densities, increasing an ICs performance, size and power consumption being equal. However, the quality with which structures are printed remains essential because having too many defective structures on a chip will stifle its performance or cause it to not work at all.

The need for tiny but high quality features, means that a very high resolution is required when printing designs during the lithography step. Therefore, not only should the possibility exist to alter the chemical properties of the resist in a very local manner, the light beam produced by the lithography machine should also be very stable and precisely concentrated to form the right aerial image. Shaping such a stable and precise beam of light is far from trivial and the required aerial image depends upon the features to be printed.

Features

The features, which comprise the structures on an IC in theory could have any shape. However, in practice, many standardized features do exist because they are useful for example during the production of a certain type of transistor. Furthermore, the existence of standardized features enables comparisons between different lithography machines by comparing the smallest sized features that a machine can accurately produce. Two standard features for comparing machine performance for example could be lines-and-spaces and contact holes, both of which are shown in Figure 3.2.

The distance between two lines combined with the width of a line is called pitch. The minimum pitch

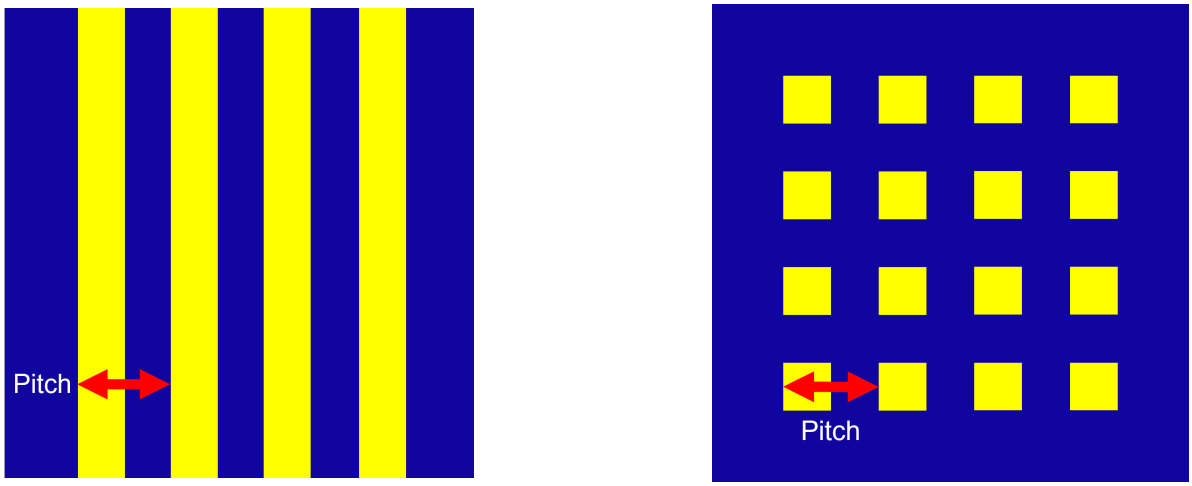

(a) Lines-and-spaces **(b)** Contact holes

Fig. 3.2: Two examples of standard features with their pich (red arrow). Yellow and blue indicate areas of the resist receiving a dose higher or lower than the threshold respectively.

that can be achieved by a machine determines how densely transistors can be packed together on a chip. If a higher density of transistors can be achieved, performance of chips can be improved. Hence, lowering this minimum pitch, or pitch resolution, of a lithography machine is actively pursued. However, pitch resolution is limited by physical factors as becomes apparent from inspecting the Rayleigh resolution equation [10]:

$$pitch\ resolution = k_1 \frac{\lambda}{NA}, \tag{3.1}$$

where λ is the wavelength of the light a machine uses, k_1 is a parameter which depends on the specific lithography process and NA is a dimensionless number called numerical aperture, which indicates over which range of angles an optical system can accept light to produce output. Based on the maximum input angle θ_{max}, see Figure 3.3, the NA is defined as:

$$NA = n \sin(\theta_{max}), \tag{3.2}$$

with n the index of refraction of the medium in which a lens is placed.

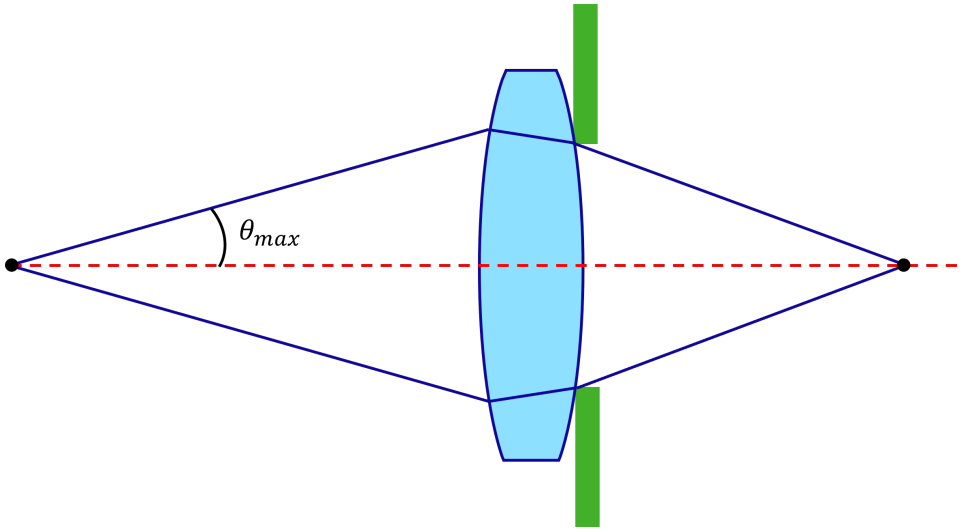

Fig. 3.3: Illustration of an optical system comprised of a lens followed by an aperture stop (green). The angle θ_{max} determines the NA of the system.

With Equation 3.1 in mind, a better *pitch resolution* can be obtained by decreasing λ, increasing the NA of the system or improving the lithography process in a way that decreases k_1. Changes in λ are quite challenging from a physical point of view since using a different wavelength of light requires a different light source, also changing the optical behavior of the light for smaller wavelengths, which can pose new issues. Increasing the NA is difficult from a practical point of view: to obtain a larger NA increasingly larger lenses or mirrors are required. Larger lenses and mirrors are harder to produce and need more space in the lithography machine, meaning the machines might get larger than the spaces that can be allocated to them within chip factories. The value of k_1 however, depends on the optical methods used to generate the image of features in the first place. To create such small images diffraction is used.

Diffraction

Diffraction is the phenomenon of waves changing direction when they encounter changes in the medium through which they travel. Most often this change in medium presents itself in the form of a material that obstructs the original direction of propagation of the waves, but changes in for instance refractive index of the medium can also cause diffraction. The classical example often given to illustrate diffraction is that of a wave moving through a slit, a hole in a barrier material that blocks the path of the wave, as depicted in Figure 3.4.

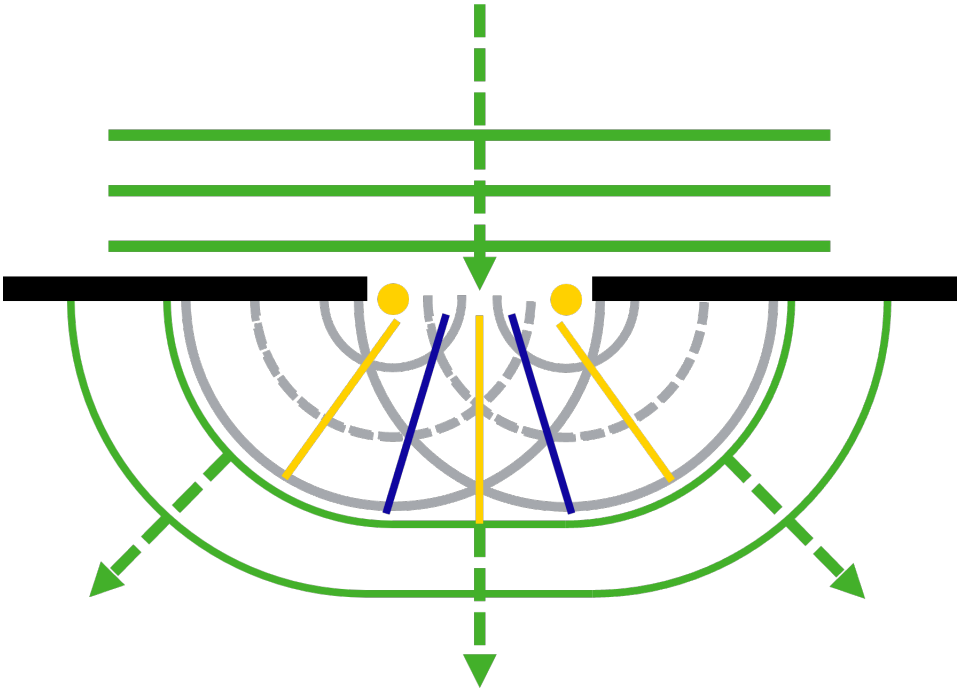

Fig. 3.4: Illustration of the Huygens-Fresnel principle for a plane wave moving through a slit. The total wave (green) after the slit is the sum of the waves from the point sources (yellow dots). The gray lines represent maxima and minima (dashed) of the spherical waves that create constructive and destructive interference at the yellow and blue lines respectively. Adapted from [11].

According to the Huygens-Fresnel principle the way a wave front propagates through space can be found by replacing the wave front by infinitely many point sources of infinitesimal size. These point sources output spherical waves that can be added together to obtain the total wave front on the other side of for instance a slit. This addition of individual waves into a total wave is called superposition. When adding two waves, they can either support or work against each other. Phrased differently, the waves show either constructive or destructive interference, as illustrated in Figure 3.5.

One of the places where interference patterns emerge is when waves encounter periodical structures, called diffraction gratings. Within EUV lithography, a carefully designed reflective diffraction grating, called a mask or reticle, is used as a blueprint of the features to be printed on a chip. Through use of

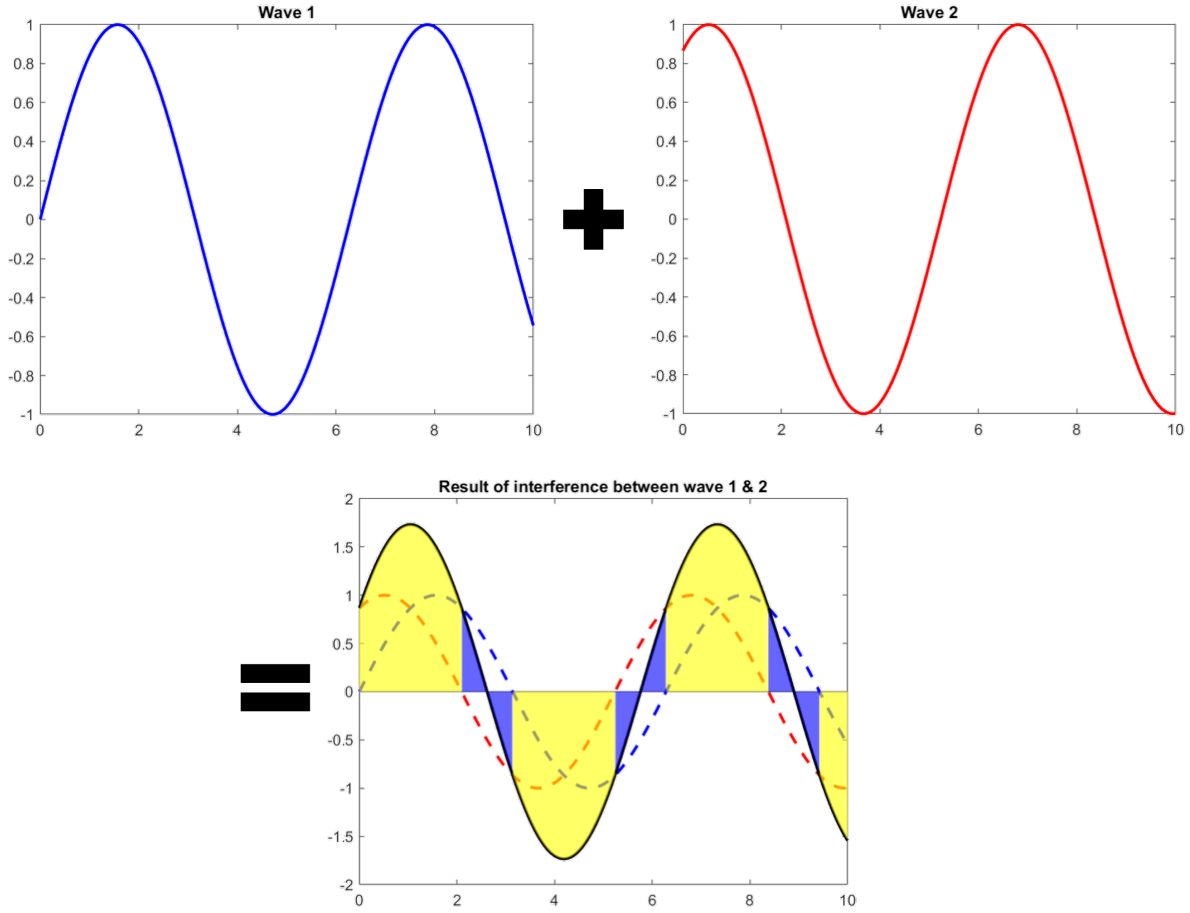

Fig. 3.5: Two waves and the result of interference between them. The colored areas mark constructive (yellow) and destructive (blue) interference respectively. Note that the y-axis is scaled by a factor of 2 in the wave created by interference.

these reticles, interference patterns can be created. These patterns are transformed back by a system of mirrors into demagnified, images of the blue print on the reticle. An example of such an interference pattern created by a diffraction grating and its final projection onto the resist is shown in Figure 3.6. Note that the aerial image is given in intensity and the thresholds indicate a dose, but assuming that the aerial image is constant over time, the curve of the received dose will have the same shape. Since the grating shown is considered to be an infinitely repeating pattern of lines-and-spaces, superposition of all wave fronts the results in an electric field, T_m, which has maxima and minima of infinitesimal width and is zero elsewhere. The reason for this is that light interacts with the grating in a way that resembles a Fourier transform (see Appendix A). Under specific conditions regarding the distance from the mask and the size of its features, the Fraunhofer diffraction integral gives the diffraction pattern [10]:

$$\begin{aligned} T_m(f_x, f_y) &= \int_{\infty}^{\infty} \int_{\infty}^{\infty} E_i(x,y) t_m(x,y) e^{-2\pi i(f_x x + f_y y)}\, dx\, dy \\ &= \mathcal{F}\{E_i(x,y) t_m(x,y)\}, \end{aligned} \tag{3.3}$$

where $f_x = nx'/(z\lambda)$ and $f_y = ny'/(z\lambda)$ are spatial frequencies found in the plane of observation, $x' - y'$, which is a distance z away from the mask, with n the index of refraction for the medium around the mask and λ the wavelength of the monochromatic light incident on the mask; $E_i(x,y)$ is the incident electric field for the point (x,y) on the mask, $t_m(x,y)$ is the E-field transmittance function of the mask and $\mathcal{F}\{\cdot\}$ is the Fourier transform.

One of the properties of the Fourier transform is that it transforms an infinite periodic series of block waves into an infinite series of delta pulses (see Appendix A). The distance between these pulses, or

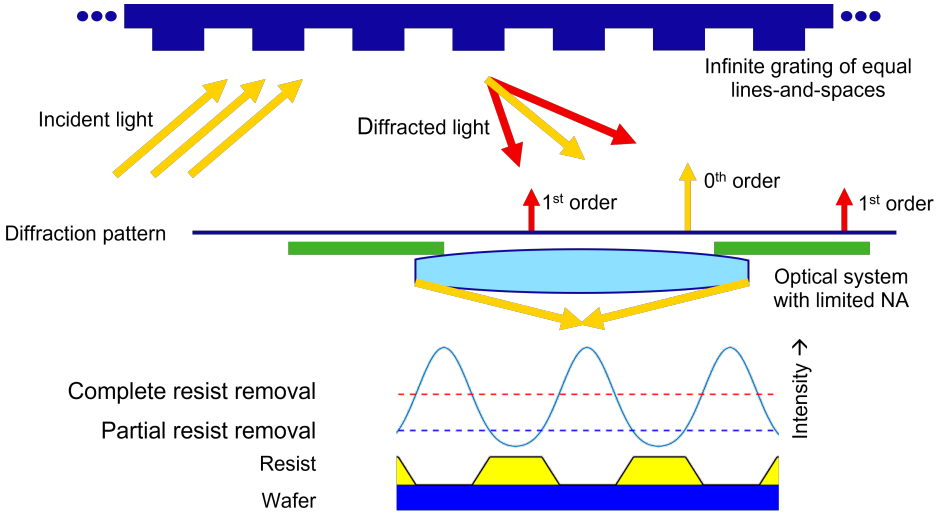

Fig. 3.6: Example of an infinite grating of lines-and-spaces illuminated under an angle. Vertical arrows represent the maxima of the electric field resulting from diffraction, which only consists of delta pulses. The orders captured by the optical system are transformed into a lower resolution image of the grating, given by the intensity curve (blue, enlarged). The final pattern in resist (black curve, enlarged), depends on the image intensity, the complete removal dose threshold (red dashed line) and the partial removal threshold (blue dashed line) of the resist.

diffraction orders, is inversely proportional to the pitch of features on the mask. Hence, if the pitch of the features becomes smaller, the diffraction orders will be further apart. This is important because the optical system will project a sharper image if more diffraction orders enter it. The dependence of image resolution on the number of diffraction orders entering the optical system, results from the interaction between mirrors or lenses and light, which can be described by an inverse Fourier transform [10]:

$$E(x,y) = \mathcal{F}^{-1}\{T_m(f_x,f_y)P(f_x,f_y)\}, \tag{3.4}$$

where $E(x,y)$ is the electric field in the image plane of the mirror or lens, $\mathcal{F}^{-1}$ is the inverse Fourier transform (see Appendix A) and $P(f_x,f_y)$ is the pupil function, which describes which spatial frequencies can be imaged by a mirror or lens and is defined as:

$$P(f_x,f_y) = \begin{cases} 1, & \sqrt{f_x^2+f_y^2} < \frac{NA}{\lambda} \\ 0, & \sqrt{f_x^2+f_y^2} > \frac{NA}{\lambda}. \end{cases} \tag{3.5}$$

As becomes apparent from Equation 3.5, the spatial frequencies that enter a mirror or lens are bounded by the wavelength of the light and by the size of the NA. Frequencies within the part of the domain of the pupil function that give a 1 are in the NA of a mirror or lens, the other frequencies are out of the NA. To form any kind of image of the mask, at least two diffraction orders need to enter the optical system. If only one order would be used for imaging a constant intensity would end up at the wafer, because no interference would be observed. To image small pitch features with diffraction orders that are far apart, getting multiple orders to enter the optical system becomes a challenge because higher diffraction orders start to move to out of the NA. This is where oblique illumination can be used to shift diffraction orders back into the NA.

Oblique illumination

When illuminating the reticle with a beam of normally incident light the created diffraction orders are centered around the zero frequency. Therefore, as structures on the reticle get smaller, both first orders of the diffraction pattern will be located outside of the NA as the distance between the zeroth and one of the first orders is larger than the NA. However, the optical system has a maximum angle in both directions and hence can accept a total distance of $2NA$. Thus, by shifting the location of all the

diffraction orders in the frequency domain, it would still be possible to capture at least two orders and create an image. Since the interaction between light and a grating is described by a Fourier transform, the frequency shift property of a Fourier transform illustrates how by changing the angle of incidence the diffraction orders shift, placing one of the second orders back into the NA. If $g(x, y)$ and $G(f_x, f_y)$ are a function and its Fourier transform then the following holds:

$$\mathcal{F}\{g(x,y)e^{i2\pi(xf'_x+yf'_y)}\} = G(f_x - f'_x, f_y - f'_y), \tag{3.6}$$

where f'_x and f'_y are the shift in frequency in the f_x- and f_y-direction respectively. This shows that if a factor of $e^{i2\pi(xf'_x+yf'_y)}$ could be incorporated into the input of the Fourier transform in Equation 3.3, a frequency shift of $-f'_x$ and $-f'_y$ could be obtained for the diffraction orders. Now as it happens, by changing the angle the incident light makes with the reticle, often such a factor can be achieved. For a plane wave with a magnitude of one which is tilted with respect to the x- and y-axis for example, instead of $E_i(x, y) = 1$, the incident electric field becomes $E_i(x, y) = e^{i2\pi(sin(\theta'_x)x/\lambda+sin(\theta'_y)y/\lambda)}$, with θ'_x and θ'_y the tilt angles in x- and y-direction respectively. Thus illuminating under an angle makes shifting the frequency of diffraction orders back into the NA and thereby printing smaller pitch features possible.

Apart from capturing at least two diffraction orders, from an imaging perspective it is also desirable to capture as much intensity as possible in the diffraction orders being used. As the intensity of the aerial image gets amplified, dose thresholds of the resist can be surpassed in less time, leading to more throughput of the lithography machine. However, the intensity of light that can be projected on a spot on the reticle is limited by physical as well as practical considerations. For one, the light source will never produce a infinitely small bundle of light with an infinitely high intensity, nor is this desirable because the optical parts of a lithography machine would degrade very quickly due to the gigantic amounts of localized energy they would receive. Furthermore, from a practical standpoint a machine should be able to project light onto the reticle under an angle that generates the best image for a diverse range of features. Since different feature types and sizes lead to various diffraction patterns, to capture the most information from this pattern and produce the sharpest image, sometimes smaller and sometimes larger angles are optimal. Moreover, most masks do not contain a single repeated feature, but multiple different features. Hence, in practice instead of one illumination angle, a range of illumination angles is used. For each angle in this range, the path of the light towards the reticle has a different length. These different path lengths lead to partial incoherence of the total light beam: diffraction orders only show interference with diffraction orders produced by light which is incident on the reticle with the same angle. Thus a range of angles produces a range of diffraction orders and each set of diffraction orders resulting from one angle produces the same aerial image. As a result, the total aerial image is simply the sum of the images for all angles and a higher intensity image is obtained.

Uniformity of illumination of the reticle

A light beam hits an area of the reticle instead of just one spot. To ensure that the features printed on the wafer are the same independent of location in the beam of light projected onto the resist, the aerial image should consist only of the features to be printed and not be influenced by intensity changes that depend on location in the projection beam. During exposure of the resist, the wafer as well as the reticle move in the y-direction in such a way that a point on the wafer is illuminated by a scan of all y-positions with a fixed x-coordinate in the illumination bundle. As a result, the observed illumination is integrated in y. Thus, only spatial dependencies of the scan integrated intensity in the x-direction cause problems for the creation of accurate aerial images on the wafer. Some of the ways, in which spatial components of image intensity might impact the printed features are shown in Figure 3.7. There it can be seen that spatially dependent components of the image intensity can cause parts of the resist to be under or over exposed, creating features with the wrong size or not even printing features at all. If the intensity of the light beam with which the reticle is illuminated already contains a spatially dependent component, a projected beam without such a component cannot be attained. Therefore, a requirement for high quality lithography is spatial uniformity of the intensity of the illumination beam incident on the reticle. For a large part, the uniformity of the illumination beam, results from the set up of the mirrors that reflect the light from the light source towards the reticle.

Mirrors

EUV light has the property that it is quickly absorbed by most materials. Because of this absorption

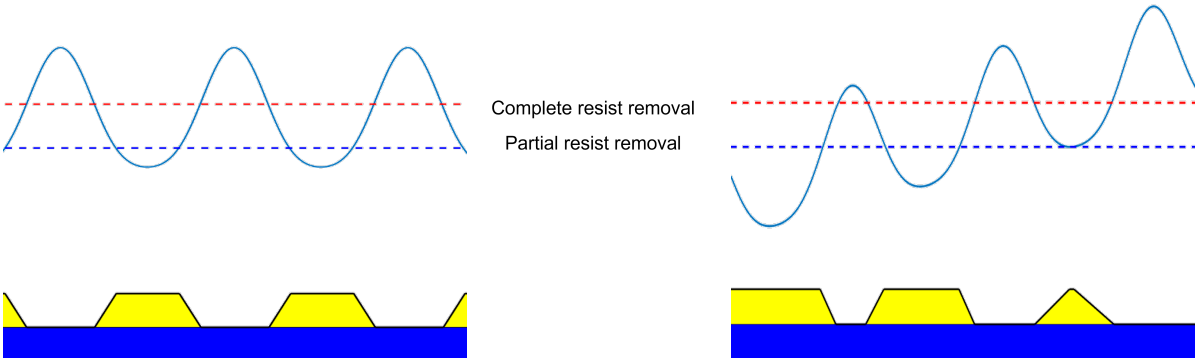

(a) Spatially uniform illumination.

(b) Spatially dependent illumination.

Fig. 3.7: Two examples of an aerial image (blue curve) and its corresponding print in resist (yellow) on a wafer (blue). The dashed lines indicate the complete (red) and partial (blue) dose threshold of the resist. In (a) a constant pattern is printed but in (b) linear spatial dependency of intensity causes an irregular print.

lenses are not fit to be used in combination with EUV light. Thus, mirrors are used in EUV lithography machines to transform light from the light source to an illumination beam with the desired angular distribution and uniformity that hits the reticle in the desired location. Then, after diffraction of the light from the reticle, another set of mirrors is used to shrink and focus the light into a smaller image which is projected onto the wafer. Next, where these mirrors are located with respect to other parts of the EUV machine and how the beam illuminating the reticle is created are discussed.

3.2 Machine layout

An EUV lithography machine is highly complex, not only because the physics behind it are intricate, but possibly even more so because it consists of an enormous amount of parts. However, to know how light moves through the machine only 5 sections of the machine, or modules, need to be understood: the source, the illuminator, the top module (containing the reticle stage), the projection optics box (or POB) and the bottom module (containing the wafer stage). Where these modules are located in the machine can be seen in Figure 3.8.

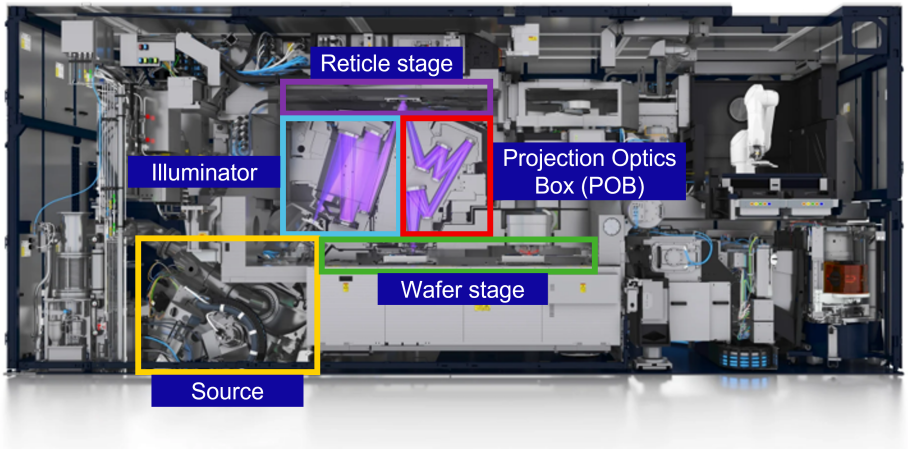

Fig. 3.8: Inside of an EUV lithography machine [12]. The five outlined sections of the machine that interact with the EUV light beam are: the source (yellow), the illuminator (blue), the reticle stage (purple), the Projection optics box (red) and the wafer stage (green).

The source is where EUV light is created by hitting droplets of tin with laser light of a larger wavelength.

Repeatedly hitting droplets results in a pulsed light source with a frequency of $50kHz$. The pulsed EUV light is reflected towards the illuminator and filtered as to only keep light with a wavelength of $13.5nm$. Subsequently, the light beam is manipulated in the illuminator to obtain light with the desired angular distribution and a spatially uniform intensity. To obtain the needed angular distribution the light which enters the illuminator at the intermidiate focus (IF) is split up into multiple beams by the Field Facet Mirrors (FFM), see Figure 3.9. These separate beams are projected onto the Pupil Facet Mirrors (PFM) to reflect each beam under the desired angle further along the illuminator mirrors towards the Reticle. At the reticle stage the separate beams, or Field Facet Images, overlap again to illuminate the same area of the reticle. Once diffracted by the reticle, the light enters the POB where the light is focused into a reduced size image of the reticle onto the wafer that is kept in the right position by the wafer stage.

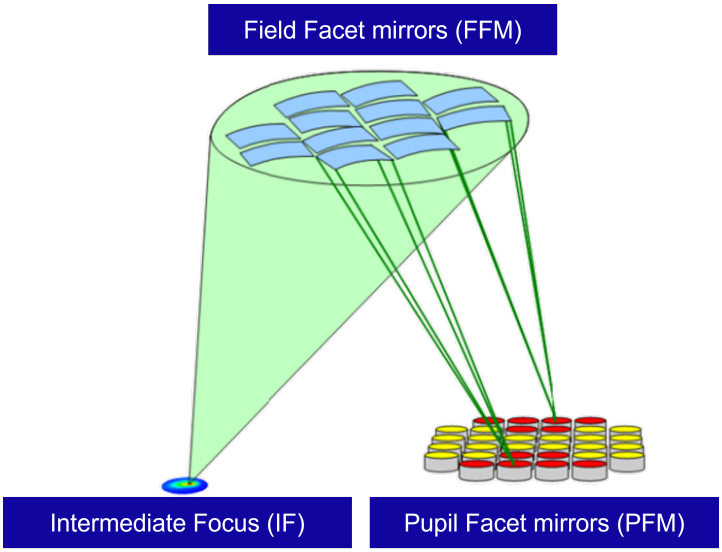

Fig. 3.9: EUV lithography Field Facet Mirror (FFM) and Pupil Facet Mirror (PFM) setup in the illuminator [13]. Light enters the illuminator through the Intermediate Focus (IF). After reflection by the FFM and PFM, the light is reflected further through the illuminator towards the reticle.

3.3 Pupils

For the imaging of features on the reticle onto the resist, illumination of the reticle under a range of angles is needed to capture multiple diffraction orders and get a sharp image. This angular distribution of light beams is produced by the configuration of the FFM and the PFM and is called the illumination pupil. The pupil is often characterized in σ-space, which is defined as:

$$\begin{aligned} \sigma^x &= \frac{M_x}{NA}\sin(\theta^x_{RL}) \\ \sigma^y &= \frac{M_y}{NA}\sin(\theta^y_{RL}) \end{aligned}, \tag{3.7}$$

with M_x and M_y the reciprocals of the magnification of the lithography system in x- and y-direction respectively, and θ^x_{RL} and θ^y_{RL} the angles in x- and y-direction of the light incident on the reticle respectively. An example of such a pupil in σ-space is given in Figure 3.10. Ideal pupils, describing the optimal angular distribution of light for a specific reticle, are approximated by configuring the FFM such that light reflected from the PFM resembles the design pupil. These pupils produced by the EUV machine are comprised of separated illuminated areas called spots. Each spot corresponds to a different bundle of light being propagated from the FFM to the PFM and further along the illuminator towards the reticle. To obtain the desired configuration between the FFM and PFM, mirror positions are actively controlled.

For complicated reticle designs with a collection of different features, different parts of the pupil have a high impact on different features being printed. Therefore, the intensity and exact angle of each of the beams comprising the pupil to a great extent determines the quality of the image printed in the resist. The method used to predict if the positions and intensities of spots comprising a pupil will result in proper images in resist is based on the Pupil Qualification Function, or PQF. Although the bundles of light hitting the PFM can be considered spot shaped, for the light hitting the reticle this is definitely not the case. At the reticle each bundle of light has diverged again to illuminate a larger area of the reticle, which is required to obtain diffraction patterns and speeds up the lithography process by printing a larger part of the feature design at once. The area illuminated by a beam of light originated from a spot on the PFM has a specific curved shape that depends on the shape of the FFM. Thus, the separate bundles of light are called Field Facet Images, FFIs, and together illuminate an area on the reticle called the illumination slit. After diffraction and propagation through the POB an area of the same slit shape but of shrunk down size on the wafer is exposed to an aerial image. Therefore, the image quality depends on a delicate interplay between the pupil configuration and the properties of the illumination slit.

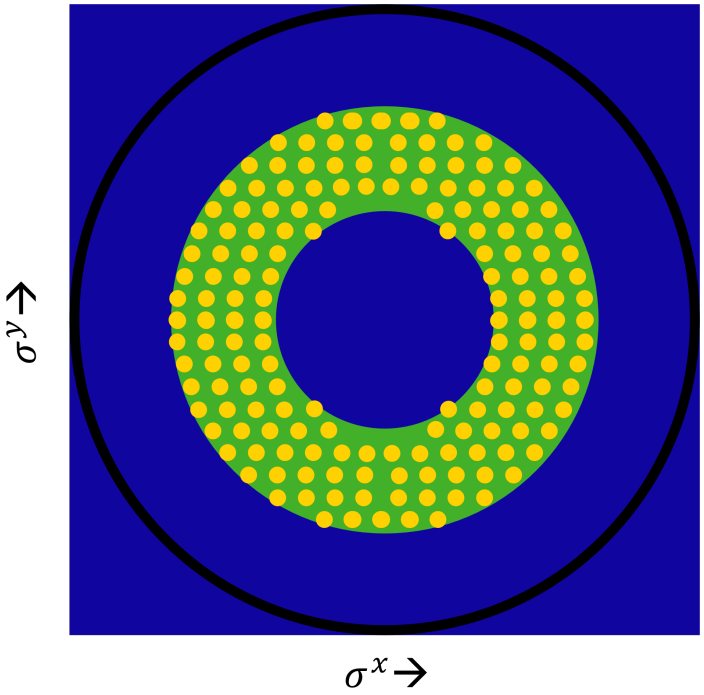

Fig. 3.10: Example of a pupil in σ-space. The FFM is configured in such a way that the beams reflected from the PFM (yellow) approximate the ideal pupil (green). The black line indicates the boundary of the pupil.

3.4 Slits

It is important to note that the previously mentioned slits are cross-sections of conic bundles of light with a specific curved shape. Although they do share the name of the gaps found in diffraction gratings, they are non-related and should not be confused. Here a more detailed description of all separate cross-sections, or Field Facet Images and their combined cross-section that forms the total slit will be given.

Field Facet Images
Since the light reflected from a Pupil Facet originates from a Field Facet with a curved shape, this bundle of reflected light is called a Field Facet Image, or FFI. Each FFI originates from a separate Pupil Facet and at that Facet is roughly focused into one spot. After reflection from a Pupil Facet, light originating

from such a spot diverges into a cone of light with a curved shape. After propagation through the illuminator this cone of light has a predefined size and illuminates the reticle at an area specified by the machine's design. This divergence of spots into slit shaped cones of light is simultaneously occurring for all spots originating from the PFM. However, whilst the spots themselves diverge into slits, the ensemble of all FFIs is converging to in the end illuminate an area on the reticle called the total slit, see Figure 3.11.

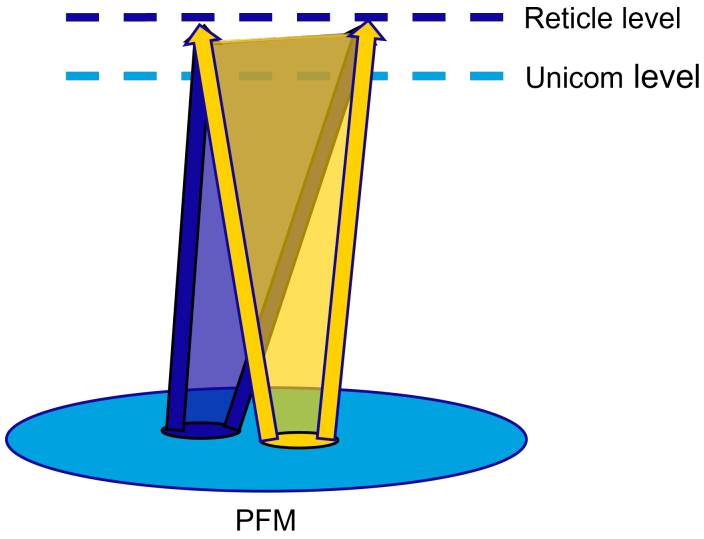

Fig. 3.11: Illustration of two FFIs (yellow and blue) originating from separate Pupil Facets. Each FFI on its own is a diverging bundle of light but the ensemble of all FFIs converges towards reticle level. Before its arrival at the reticle, the total slit passes the Unicom.

Total slit

The total slit, subsequently just called slit, is comprised of the addition of all the FFIs, which are mutually incoherent due to their different path lengths resulting form the setup to acquire different illumination angles. Thus, the slit intensity is simply the sum of all separate FFI intensities:

$$I^s(x,y) = \sum_{i=1}^{n} I_i^{FFI}(x,y), \tag{3.8}$$

where $I^s(x,y)$ is the slit intensity at the point (x,y) at the reticle, $I_i^{FFI}(x,y)$ is the intensity at the same position on the reticle contributed by the FFI originating from spot i in the pupil and the sum is taken over all n pupil spots. Admittedly, the reticle will not have the same profile of features everywhere and strictly speaking the slit is not located precisely on the reticle but on a fictive plane within the machine called reticle level, RL, which is where the nominal position of the reticle's surface is located according to the machine's design. Nonetheless, the variation in path length resulting from the different heights of features on the reticle does not impact measurements of Uniformity because of the feature independent setup of the measurement method.

By design, not all FFIs overlap perfectly on RL, rather, they are set up to overlap partially to create an area of the slit with highly uniform y-integrated intensity in the x-direction. Here y-integrated intensity means the total intensity present in the slit at a fixed x-position. With this area of overlapping FFIs the reticle is illuminated during wafer processing. This windowed part of the slit used for exposure is also the area that is measured in the measurement routines mentioned later on in this work, and unless stated otherwise will be what the word slit is subsequently used for. Along the long side of the slit on the x-axis, a number of measurement locations are defined, which are called Field Points, FPs. An example of how FFIs combine into a slit is depicted in Figure 3.12 with the difference in position of the FFIs exaggerated for illustrative purposes.

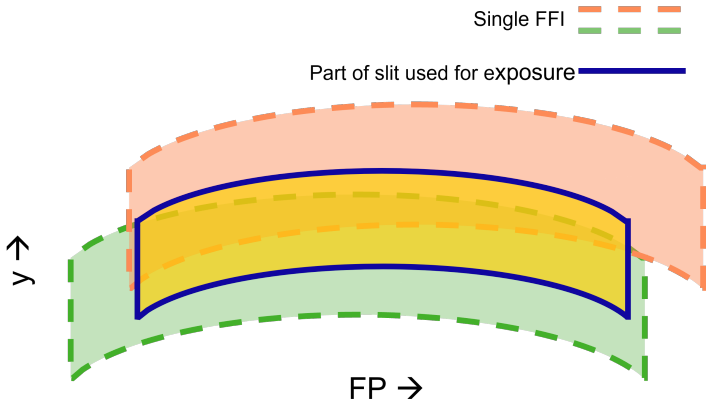

Fig. 3.12: Illustration of two FFIs on RL (orange and green) which together form a total slit. The windowed highly uniform part of the total slit used for exposure is indicated in yellow.

Fly's eye integration

Fly's eye integration is a method used in lithography systems to create a uniform bundle of light from a not necessarily uniform source of light [14]. With fly's eye integration ,the non-uniformity of the source can be averaged out. This averaging is achieved by first dividing the bundle of light emitted from the source into many parts and subsequently projecting all these parts onto the same area. If the partial beams are small enough, the illumination they contain can be considered spatially uniform and hence the sum of these beams will also be uniform. Even if the partial beams are not completely uniform, their sum can still be uniform is a symmetric source is used. (For a more detailed description of Fly's eye integration see [14])

Returning to EUV lithography, the overlap of FFIs creates a highly uniform intensity throughout the slit, precisely because the overlap is part of fly's eye integration. This uniformity is achieved by overlaying the FFIs from Field Facets that are located at different positions within a radially dependent distribution of light that hits the FFM. Apart from achieving uniformity, overlapping the FFIs, which each are associated with a different angle in the pupil, also creates a slit which at most of its interior contains the entire angular distribution of light required to optimally print an image of the reticle. Although the sum of intensities of FFI's has approximately uniform intensity due to the use of a symmetric source, individual FFIs do not have a uniform intensity. As a result of the overlap of FFIs, pupils with a different intensity distribution and slightly different spot positions are observed when investigating different positions in the slit. When measuring these pupils, a pinhole is placed at a single position in the slit that allows only the light at that position to pass. The light that passes the pinhole is propagated further through the machine and allowed to diverge in order to measure the pupil. During measurement the entire area surrounding the pupil is measured. Therefore, an algorithm is needed to identify pupil spots from a pixel image of the pupil and subsequently assign a location in σ-space and associated intensity to each identified spot. The algorithm that identifies the pupil spots is called parcellation.

3.5 Parcellation

Parcellation is the method that determines from pixel images of pupils, how many pupil spots are found, in which location in σ-space thes spots are measured and how high their associated intensities are. The input for parcellation is a pixel image, called a bitmap, of the measured pupil, in which each pixel is associated with a σ^x, σ^y and intensity value. When supplied with a bitmap, the algorithm outputs for each identified pupil spot the σ^x, the σ^y and the intensity value, I^p, that is associated with that pupil spot. The algorithm was constructed with one of the two types of measurements that will be described at the end of this chapter in mind: the scan integrated measurement. For the static measurement type parcellation is less accurate in recognizing pupil spots. The parcellation algorithm is of importance to the results of this thesis because PQF calculations are used to verify the accuracy of the model that was constructed and the PQF calculations in turn require parecellated pupils as input.

3.6 PQF

The Pupil Qualification Function, or PQF, is a method to predict if a pupil (or collection of pupils at different FP locations in the slit) will allow for the projection of a high quality aerial image onto the wafer. To this end, during PQF 7 parameters are calculated, which have been confirmed to have a strong correlation with imaging quality [15]. After calculation, a check is performed for each of these parameters in order to verify that they are within the specified range for which image quality is expected to be up to standard (in spec). Important to note is that whether these parameters are within spec only indicates if the quality of a pupil is high enough to produce small enough deviations in image formation when compared to the image design.

The input to PQF calculations consists of following:

1. σ^x, σ^y and I^p for each pupil spot in one or multiple parcellated scan integrated pupils (when multiple pupils are used they need to be from different FPs in the slit).
2. Reference design pupil.
3. Use case of features to be printed.

The output of PQF calculations consist of 7 vector parameters, for which a value is given at various pitches for the use case feature. Additionally, for each of the 7 vector parameters the maximum absolute value over pitch calculated. PQF values result from the evaluation of multiple non-linear and discontinuous functions, hence their dependence on the input pupils can be considered a project on its own.

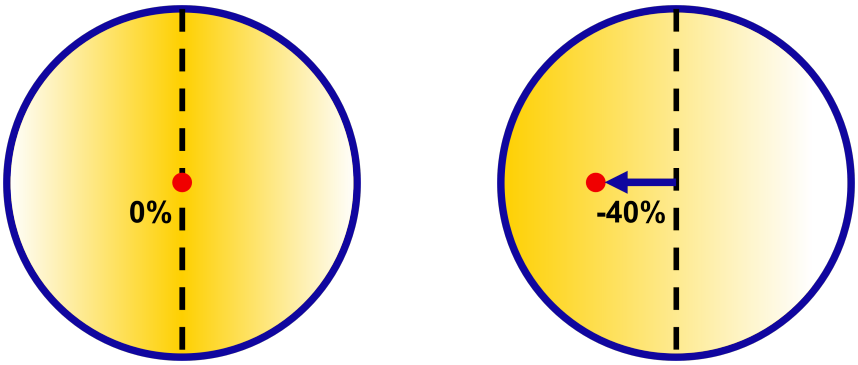

(a) Reference design pupil. **(b)** Measured pupil.

Fig. 3.13: Illustration of a reference and a measured pupil showing the center of gravity of their intensity distribution (red dot). The percentages denote the dummy PQF parameter that quantifies the relative shift of the center of gravity in the σ^x-direction.

As a simplified example, A dummy PQF parameter might quantify the location of the center of gravity of the intensity distribution in a pupil with respect to the reference design pupil. In Figure 3.13 a reference design pupil and a measured pupil with the respective centers of gravity of their intensity distributions are shown. The presented dummy PQF parameter looks at the shift of the center of gravity of the measured pupil in the σ^x-direction. Thus, when quantifying PQF as a percentage of the radius of the pupil, the parameter can become negative for shifts to the left and positive for shifts to the right. In reality shifts would be required to be small in both directions, giving a positive and negative tolerance, or spec, of equal magnitude for this PQF parameter.

With PQF, the expected impact on the imaging of features due to changes in the pupil can be quantified. Since slit uniformity, SU, corrections are actively performed in the machine by a module called the Uniformity correction module, Unicom, PQF proves to be an important tool to verify if the pupil quality is still within spec after SU-corrections are applied.

3.7 The Unicom

The Uniformity correction module, Unicom, is a module situated a small distance below the reticle next to the illumination beam, see for example Figure 3.14. The function of the Unicom is to correct scan

integrated slit intensity profiles from non-uniform to flat, an example of such a correction can be seen in Figure 3.15.

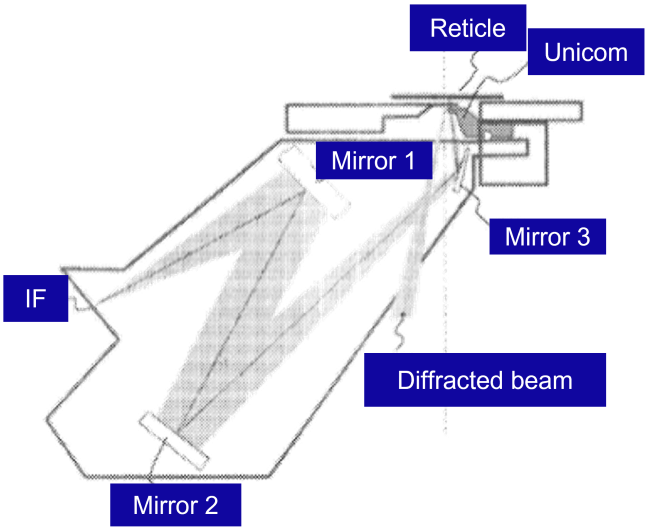

Fig. 3.14: Illustration the illuminator from the side, with the IF, a couple of mirrors, the Unicom, the reticle and the diffracted beam indicated. Reproduced from [16].

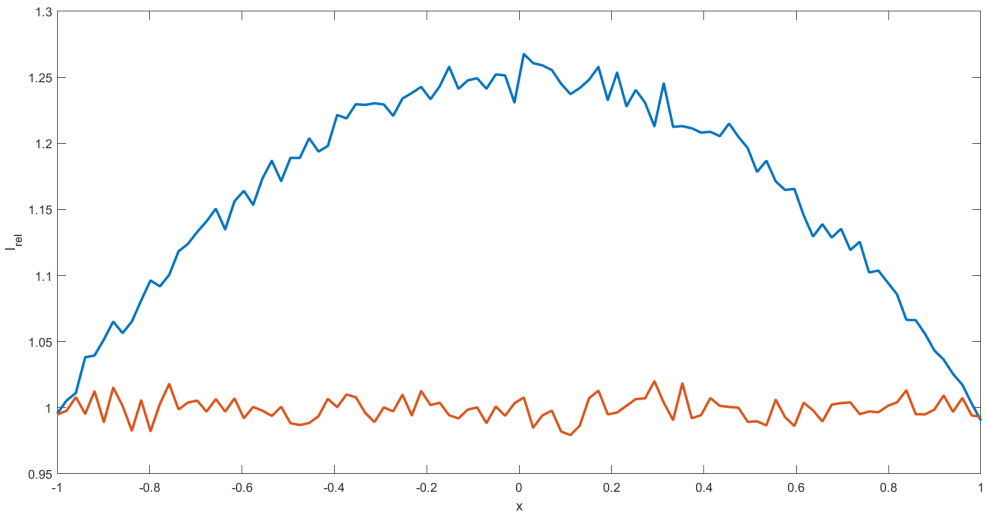

Fig. 3.15: Example of y-integrated slit intensity before (blue) and after SU-correction (orange). Intensities are plotted relative to the lowest intensity in the uncorrected slit, disregarding the simulated noise, for different x-positions in the slit with -1 indicating the left side of the slit and 1 the right.

To perform SU-corrections, first a slit profile is measured and subsequently Unicom settings are calculated that correct the slit profile to be uniform in the x-direction. The Unicom consists of a device with multiple movable fingers that can be partially inserted into the illumination beam, in the y-direction, independently of each other as illustrated for example in Figure 3.16 [16, 17]. The Unciom fingers are situated in two different planes in the z-direction (height), see for example Figure 3.17. Creating multiple planes of fingers allows for space between the fingers in each plane, while at the same time all light between adjecent fingers can be blocked by a finger situated in another plane. Space between fingers is needed such that adjacent fingers do not rub against each other whilst moving. Rubbing Unicom

fingers would create loose particles, which cause damage to the mirrors and reticle in EUV lithography machines.

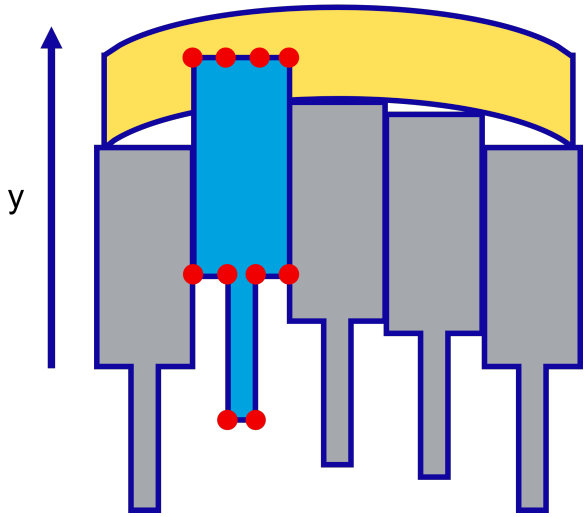

Fig. 3.16: Illustration of a top down view of five Unicom fingers with one finger inserted (light blue) and the other fingers extracted from the slit at UL. Red dots show a possible configuration of vertices describing the inserted finger.

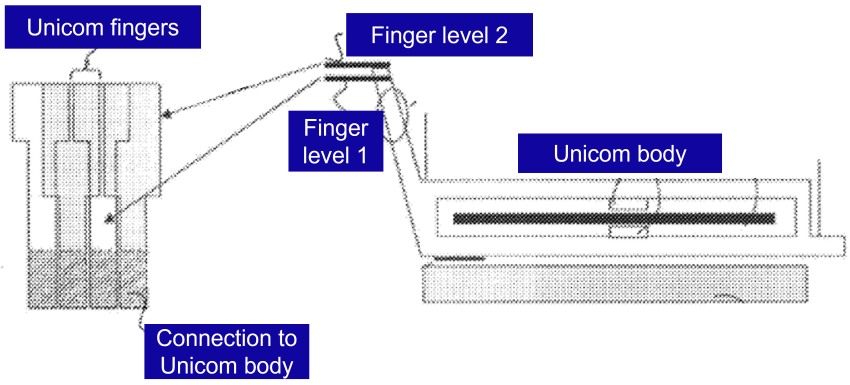

Fig. 3.17: Side view of the Unicom and a top view of a section of the two layers of fingers. Reproduced from [16].

When a finger is inserted into the slit at Unicom level, UL, it blocks a certain part of the illumination beam from reaching RL, hence lowering the intensity at the corresponding location in the slit. The amount of the intensity that is blocked depends on which part of each of the FFIs is blocked by the Unicom fingers. Because the FFIs as an ensemble are converging to the slit on RL and the FFIs themselves are diverging whilst propagating under various angles, complete blockage of light in an area of the total slit at UL does not necessarily mean that all light will be blocked in the same area of the total slit at RL. On the contrary, depending on the pupil, which determines the angle under which each FFI moves past the Unicom, at the boarder of the blocked part of the total slit at RL a gradual decrease of intensity will be observed rather than a discrete cut-off. This is simply the result of unblocked beams at UL being propagated under an angle that makes them illuminate parts of the slit that are above the profile of the Unicom fingers.

Since the Unicom fingers block intensity in the FFIs depending on the (x_i^u, y_i^u) position of the fingers in the Unicom plane, where the subscript i indicates plane in which the fingers are contained, at certain positions in the slit pupil spots will be blocked removing some illumination angles from that part of

the slit. This shows, that when correcting SU, a side effect is that pupil intensity is also changed. By investigating the blockage of intensity, $I(\sigma^x, \sigma^y, x, y)$, in the slit at RL, the effects of Unicom movements on the pupil and its PQF can be understood and predicted. Enabling such predictions can also have serious benefits to the operation of the Unicom by calculating optimal finger positions that make a trade off between SU and PQF. Furthermore, many measurement routines either depend on Unicom movements or are specifically designed to measure the Unicom's impact on the pupil or SU, meaning that accurate predictions of the Unicom's impact could shorten or replace measurement routines, allowing for more machine throughput. For ASML's customers this would also open the door to accurate predictions of how pupil quality changes over time with the Unicom's impact taken into account. Such predictions of quality changes over time could be used to plan required maintenance actions in advance instead of when a machine's output becomes sub-par, thus reducing the costs incurred by unexpected machine downtime. From a design aspect as well, a Unicom model could offer the possibility to get insight into the effects of different Unicom designs on imaging performance. This creates the opportunity to further optimize the Unicom's design and more thoroughly investigate the impact manufacturing or integration mistakes have on the EUV machine's performance. One model that already has some implementation of a prediction method for the EUV Unicom's impact is Pupil Predictor.

3.8 Pupil Predictor

Pupil Predictor is an model implemented by one of ASML's suppliers that can calculate many properties regarding pupils for different positions in the slit. Pupil Predictor predicts based on design information of the EUV machine and interpolation performed on the results of previously completed ray-tracing simulations. It also has a functionality to calculate scan integrated pupils which are adjusted to take a inputted Unicom finger insertion into account. However, since the Unicom is made by ASML, this functionality was implemented with limited knowledge about the Unicom and this is believed to have lead to a logical, considering the circumstances, yet inaccurate implementation. An investigation into where discrepancies with reality might stem from can be found in Appendix C.

3.9 Measurement Routines

A Unicom model to predict the impact of Unicom finger position on pupil quality has to produce predictions which are reasonably close to reality. Therefore, such a model will have to be verified against measurement data. Here some measurement routines will be introduced, from which either data that was used during verification of the Unicom model constructed in this thesis was obtained, or in which a version of a the developed Unicom model could be integrated to improve machine throughput.

Static vs Scanning measurements

For many measurements two types exist: a static and a scan integrated (scanning) version. For a static measurement, quantities relating to one position (x, y) in the slit are measured and sensors remain stationary. During scanning measurements quantities are measured with the measurement devices moving along the y-direction of the slit such that one measurement's results are based on a line scan of the slit with a fixed x-position. The difference between the part of the slit that is measured during both types of measurements is illustrated in Figure 3.18.

During a series of static measurements more information on the dependency of a measurement quantity on the location in the slit can be inferred. However, scan measurements might resemble the situation during wafer processing more closely as the image ending up on a wafer is produced by the same scanning motion through the slit. Further benefits of scan measurements are that for each x-position only one measurement has to be performed instead of multiple with different y-positions, thus scan measurements of the slit take up less time than the multiple static measurements that would be required. Hence, from a throughput perspective, scan measurements are preferred but come at the price of obtaining less spatial information. Although the scan measurements are performed during a motion which is similar to the motion during wafer processing, they might be impacted more by random effects in the machine when compared to combining multiple static measurements at a fixed x-position but different y-positions. The amount of energy passed from source to the machine is roughly kept constant during both measurement types to determine measurement time. Therefore, assuming the presence of zero mean ergodic in mean noise in the measurements, in the combination of static measurements,

which individually have the same measurement time as a scan measurement, this noise will likely be averaged out to a certain degree.

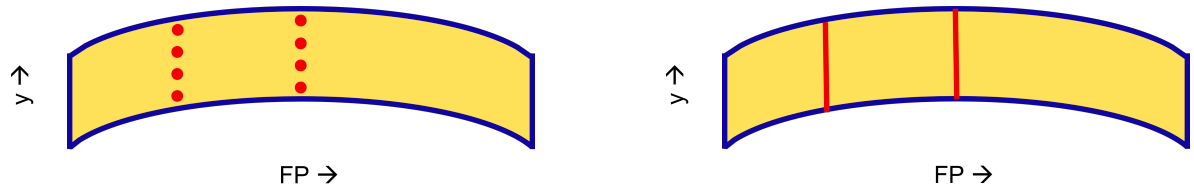

(a) Static measurement positions.

(b) Scan measurement positions.

Fig. 3.18: Example of measurement positions (red) in the slit for a static (a) and scanning (b) measurement routine. During the static measurement routine one measurement is performed for each location indicated by a red dot. During the scanning measurement routine the same FP positions are measured but by performing a single scan over the red line.

ISPQ & IPD

Both the Illumination System Pupil Qualification test, ISPQ [18], and the EUV Illuminator Pupil Diagnostics test, IPD [19], can be used to measure pupils in static or scanning mode. During these tests the Unicom fingers can manually be set to fully extracted from the slit at UL, set to a specified pattern or configured automatically based on the OFP and Uniformity Update functionalities described shortly. The main output of both tests consists of a bitmap pupil per measurement position.

Both ISPQ and IPD measurements can be used as input for a model that predicts the impact of Unicom settings on pupils. To use these measurements as input, the Unicom fingers should be fully extracted during measurement. To verify a Unicom model's performance, the pupil predicted by the Unicom model for specific Unicom settings can be compared to measurements of the same pupil with those exact settings activated on the actual Unicom. If a Unicom model, given measurements with the Unicom fingers extracted, is able to accurately predict the pupils that are observed when the Unicom are inserted, additional ISPQ and IPD runs to investigate the impact of the Unicom's settings on pupils could (partially) be replaced by the model's simulations.

OSD

The Optical surface diagnostics test for EUV with added POP measurements, OSD, measures a set of basis pupils from which digital versions of all other pupils can be constructed. If these basis pupils are measured with the Unicom fingers extracted, all pupils without Unicom effects could be constructed. By subsequently a Unicom model the Unicom's effects could then be corrected for to achieve more accurate predictions for pupils which are impacted by the Unicom. Currently no such Unicom corrections can be added to these constructed pupils because no accurate model to predict the Unicom's impact on pupils is available.

OFP

The OFP test optimizes the Unicom finger position per pupil shape in order to improve slit uniformity for each pupil shape. The optimal Unicom finger positions are found by iterating through consecutive steps of measuring the slit profile and predicting the Unicom finger positions that would result in a uniform slit profile. If better predictions of the effect of Unicom finger positions on the slit profile could be given by a Unicom model, a smaller number of required iterations to get the slit uniformity within spec might be achievable. The resulting finger positions are stored and used for Unicom initialization when switching pupil settings. Additionally, measurements containing the scan integrated intensities, at the x-location of the Unicom fingers, are stored for multiple insertion depths of individual fingers. At set moments during production the finger positions are optimized again by performing Uniformity Update.

Uniformity Update

Uniformity Update, UU, is a functionality that is developed to correct for slit uniformity drifts over

different timescales [20]. During this correction the Unicom fingers are moved such that optimal SU results. Therefore, having good predictions of the impact of Unicom fingers on the intensity that ends up in the slit is crucial.

3.10 Overview

With the concept of static measurements of pupils through a pinhole in mind, a connection between pupils, the slit and the effects of inserted Unicom fingers can be made. A simplified illustration of two FFIs passing the Unicom whilst propagating to RL to form at RL can be seen in Figure 3.19. Subsequently at the location of the pinhole, the pupil is measured by a sensor located at wafer level. The overview is not exact but serves to illustrate that the location of the pinhole fixes a (x, y)-coordinate pair in the slit for which the measured pupil contains information about the (σ^x, σ^y)-coordinate pair and thus of the angles under which different FFI propagate at the pinhole. Additionally, the pupil spots contains information about the intensity of the associated FFIs at the pinhole. Due to the different points of origin of the FFIs (at the PFM) and the difference in their propagation angles as well as the divergence of each FFI, the Unicom fingers might block the light in one FFI from reaching the pinhole but not the light in another FFI. Therefore, predicting the effects of the insertion depth of Unicom fingers on pupils at different locations in the slit using measurements becomes a non-trivial task.

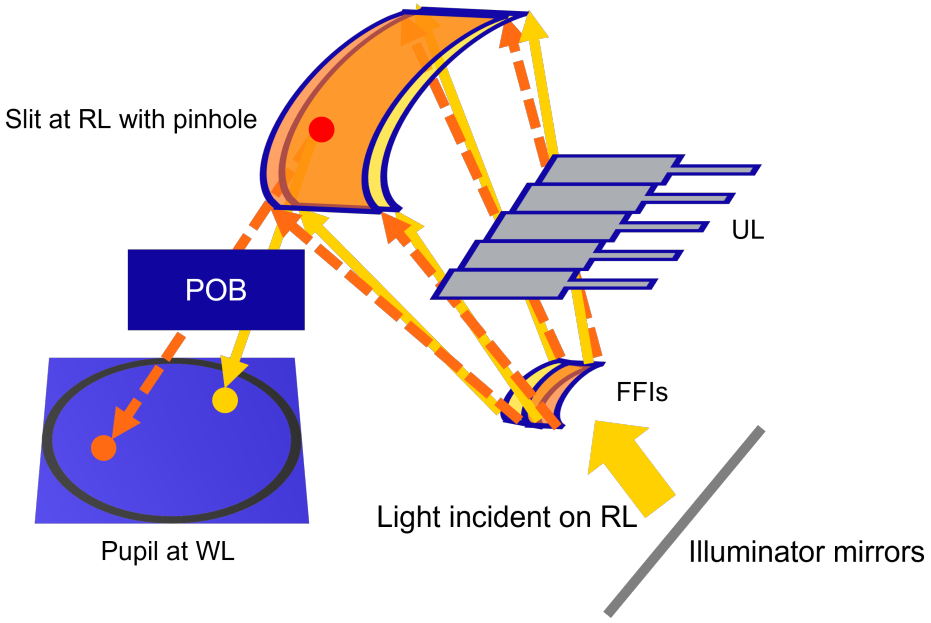

Fig. 3.19: Simplified illustration of 2 FFIs passing the Unicom whilst propagating to RL. The pupil measured at Wafer Level (WL) through the red pinhole contains information about the propagation angles of the FFIs at the pinhole and can be affected by inserted Unicom fingers.

4 Goal and background

In this chapter the business case for a Unicom model will be presented. Next, the exact goal for the model that is constructed in this thesis will be specified using concepts from the previous chapter. With the goal of the thesis in mind, similar problems described in literature are explored to provide context to the problem at hand.

4.1 Business case for a Unicom model

A model that is able to accurately predict the effect of the Unicom fingers on pupils can increase the value ASML's customers can get out of ASML's lithography machines and allow for more accurate qualification of imaging by the machine. There are three main categories of applications for such a model:

1. Real time quality monitoring & predictive maintenance.
2. Speedup of existing routines.
3. Integration in internal & external design processes.

For each of these categories an explanation of how a Unicom model could be used and what its impact would be is presented below.

Real time quality monitoring & predictive maintenance
The intensity distribution of pupils and how this distribution changes throughout the slit has a high impact on quality of printed features that a lithography machine produces. Therefore, it is beneficial to ASML and its customers to know if the quality of pupils a machine produces is up to par when deciding if re-calibration or maintenance routines need to be executed. However, from a production perspective, it is desirable to limit the amount of measurement time required for quality assurance to a minimum, since lithography machines are not processing wafers during this measurement time. Thus, with the availability of an enormous amount of different pupil settings and Unicom finger configurations, which change regularly, it becomes unpractical to perform pupil measurements for every single setup.

Hence, to monitor pupil quality after each change of pupil or Unicom settings whilst upholding throughput, predicting pupil quality by using measurements performed on a small set of basis pupils is necessary. To this end, any pupil can be constructed from these basis pupils which are measured with the Unicom fingers extracted. Subsequently, the impact of any configuration of the Unicom fingers on the constructed pupil can be accounted for by a Unicom model, resulting a prediction of any pupil produced by the machine. Once a prediction for a pupil is available, its PQF parameters can be calculated to check if the quality of this pupil is in spec. This procedure allows for increased throughput by limiting the number of executions of calibration and maintenance routines to precisely those instances for which these routines are predicted to have significant impact on keeping pupil quality in spec.

Building upon the real time monitoring of pupil quality, predictive maintenance becomes possible. Whereas during real time quality monitoring the necessity of maintenance actions are assessed for the present moment, predictive maintenance would allow for scheduling these maintenance steps in advance. The ability to schedule maintenance is beneficial because lithography systems are part of a production process involving many other machines. As a consequence, unscheduled machine downtime of a lithography machine can easily cascade into idle time for many other machines, rapidly ramping up costs for ASML's customers. If on the other hand machine downtime is expected in advance, customers can design scheduled use of their machines accordingly and incur a far smaller reduction in the throughput of their production process. By obtaining and storing real time pupil quality assessments, trends in pupil quality can be investigated and used to predict when maintenance actions will be due.

To give a rough estimate of the impact of unscheduled downtime on EUV lithography machines, as of 2016 average unscheduled downtime of the NXE:3300B lithography machine was reported to contain about 50% of total machine downtime [2]. More recently, in 2021 ASML reported an average downtime for EUV machines of about 12% during their talk about Installed Base Service Strategy on investors day [3]. Additionally, nominal costs of unscheduled downtime can be \$20 per second [4]. Thus, a rough estimate of the costs of unscheduled machine downtime becomes: $\$20 \cdot 3600$ s/h $\cdot 24$ h/day $\cdot 365$ day/y $\cdot$ 12% downtime $\cdot$ 50% unscheduled downtime / downtime $\approx \$38 \cdot 10^6$ per machine per year. Although

pupil or Unicom related issues are not necessarily the largest contributors to this downtime, preventing even a fraction of the downtime would have significant impact for ASML's customers.

Speedup of existing routines
During setup of an EUV lithography machine for production, but also especially during the production itself, many algorithms are used to calibrate and qualify the machine's performance. Two of these algorithms, OFP and UU [20, 21], are used to calibrate the Unicom fingers in a way that optimizes slit uniformity. These algorithms involve an iterative process in which a chain of consecutive measurement, prediction and finger movement steps is repeated multiple times as to obtain the desired SU and finger calibration.

Currently, predictions of the impact of finger movements are often made based on slit intensity measurements of situations where a single finger is inserted to various depths. However, neighboring fingers overlap and light that is already blocked by one finger will not be blocked again by its neighbor. Therefore, the predicted optimal locations of fingers are not truly optimal and additional iterations during finger calibration are needed. If instead predictions could take the optimum of the joint profile of fingers into account, fewer iterations might be needed and the time needed for calibrations could be reduced.

Since in each point (x, y) in the slit the intensity of the slit consists of all intensity in the pupil at (x, y), a Unicom model that predicts the impact of the Unicom on pupils also predicts the impact of the Unicom on the slit. By design, such a Unicom model may be constructed to account for the joint effect of all of the Unicom fingers. Thus, a Unicom model could speedup existing routines by reducing the number of iterations needed to calibrate the positions of the Unicom fingers to their true optimum, allowing for increased machine throughput.

Integration in internal & external design processes
When designing parts for lithography machines, investigating the impact of a part's design on machine performance is crucial. The impact of a part's design on machine performance often depends on the interaction between that part and other pieces of the machine. If a Unicom model allows the user to input different Unicom designs, the impact of different Unicom designs on pupils and slits could be studied digitally. This would allow to quickly test multiple Unicom designs without the costs associated to manufacturing parts of the design. Additionally, the results of such tests can be used during similar design processes for other machine parts.

Conversely, the impact of the design machine parts on the Unicom could also be investigated using a Unicom model. A Unicom model could for instance allow for inputs regarding illumination angles, distances between the reticle and the Unicom fingers or to the intensity distributions of pupils. If design changes in other parts of the machine would impact any of these inputs of the Unicom model, the impact of the Unicom on pupils and SU could quickly be re-evaluated. Moreover, when machine parts deviate from their design due to the manufacturing or assembly process, the impact of these deviations can be calculated.

Additionally, a Unicom model could have beneficial impacts on the design processes of customers, as well as suppliers. When verifying that, with a new mirror setup, pupils and slits can be created which meet certain criteria, the Unicom could also be taken into account. This means that more accurate predictions of the performance of new setups will be available, which enables designers to make more informed decisions. For customers, predicted pupils with the effects of the Unicom accounted for could now be made available. These predicted pupils could then serve as input for lithography simulations used by customers to design their production processes. To enable these improvements in supplier and customer design phases, only the impact of the Unicom needs to be know, hence exact designs would not need to be shared between the involved parties.

4.2 Goal of the Unicom model

In this thesis a Unicom model will be developed from the perspective of real time quality monitoring of pupils. However, the resulting model will likely simultaneously be useful in satisfying the two other business cases presented in Section 4.1. With quality monitoring of pupils in mind, the goal of the Unicom model can be stated as follows:

"Given a collection of reticle level pupil measurements with the Unicom fingers extracted from the slit and a vector of positions for the Unicom fingers after insertion, predict the collection of reticle level pupil measurements with the Unicom fingers inserted".

Or, mathematically speaking:

"Given $\mathbf{I^0}$ *and* $\mathbf{d}$*, predict* $\mathbf{I^d}$*"*,

where $\mathbf{I^0}$ is a collection of measurements of the pupil at reticle level without Unicom finger insertions, $\mathbf{d}$ is a vector containing the displacement in y-direction of each of the Unicom fingers with respect to the fully extracted positions and $\mathbf{I^d}$ is the collection of reticle level pupil measurements with Unicom fingers inserted to the positions specified by $\mathbf{d}$.

The goal above seems very clear and concise, however, upon closer inspection it is still somewhat ambiguous. For instance, measurements can be performed in a static or in a scanning setup and the measurements can be used in bitmap or in parcellated format. Furthermore, different pupil settings obviously lead to differences in pupil measurements. Additionally, changing settings of machine parts, swapping machine parts, or even using a different machine altogether, can cause discrepancies between $\mathbf{I^0}$ and $\mathbf{I^d}$ which are not due to the displacement, $\mathbf{d}$, of the Unicom fingers. Therefore, the requirements on the input of the model and the possible settings for which it performs predictions should be specified. Hence, the scope of this thesis is restricted to predicting measurements with inserted Unicom fingers from measurements with extracted Unicom fingers, where only the positions of the fingers of the Unicom have changed.

Admittedly, these conditions will never hold exactly and two measurements, $\mathbf{I^d}(t_1)$ and $\mathbf{I^d}(t_2)$, will differ because they need to be measured at two different moments in time t_1 and t_2. Even if $\mathbf{d}$ is identical for both measurements and measurement noise is disregarded, effects such as drifts of mechanical parts, of the plasma source and degradation of mirrors, will still cause differences between both measurements as $\Delta t = t_2 - t_1$ increases. Although some calibration routines that counteract the effects of drifts and degradation exist, these will also change the machine's settings meaning that they will change the state of the machine. Nevertheless, ASML's machines are able to print features with a certain consistency, therefore the variation between $\mathbf{I^d}(t_1)$ and $\mathbf{I^d}(t_2)$ can still be expected to be contained. Thus accurate predictions for $\mathbf{I^0}$ based on $\mathbf{I^d}$ will likely be possible. However, the accuracy found during verification of a Unicom model will remain inherently limited by these non-Unicom related differences between measurements used as input for the model and measurements representing the desired model output.

With regard to the possibilities for different types of measurements and data formats described as in and output of the Unicom model, 16 combinations of static/scanning and bitmap/parcellated input and output measurements exist, but the number of options for which it makes sense to try to develop a Unicom model is lower. For example, when inputting parcellated data for $\mathbf{I^0}$ one cannot reasonably expect to predict $\mathbf{I^d}$ in bitmap format without additional assumptions about spot shapes. These assumptions would be needed because bitmaps contain information about the intensity distributions of pupil that is no longer present in a parcellated pupil, in which each pupil spot has only one intensity and one location. The assumed spot shapes will not be equivalent to the actual spot shapes and will thus introduce errors into the model that can be prevented by choosing a different combination of input and output data for the model.

In the same way it does not make sense to look for a prediction of static measurements based on scanning measurements because static measurements contain information about how the intensity distribution of the pupil depends on the y-position in the slit, whereas for scanning measurements this information is lost due to the integration in the y-direction. Furthermore, since the parcellation algorithm is ill-suited for static pupils, combinations of static measurements with the parcellated data type should currently also not be used. These restrictions leave 6 possible combinations of in and output

data for the model as shown in Table 2.

	$\mathbf{I^0}$ measurement type	$\mathbf{I^0}$ data type	$\mathbf{I^d}$ measurement type	$\mathbf{I^d}$ data type
1	static	bitmap	static	bitmap
2	static	bitmap	scanning	bitmap
3	static	bitmap	scanning	parcellated
4	scanning	bitmap	scanning	bitmap
5	scanning	bitmap	scanning	parcellated
6	scanning	parcellated	scanning	parcellated

Table 2: Feasible combinations of measurement and data types for input, $\mathbf{I^0}$ (extracted fingers), and output data, $\mathbf{I^d}$ (inserted fingers), of a Unicom model.

Of the combinations in Table 2, 4-6 are desirable from a practical point of view because these do only require a collection of scanning measurements, which are less time consuming to perform than collections of static measurements. For the impact of the Unicom on pupil quality, and thus the predictive maintenance business case, scanning bitmaps would be available as input and scanning parcellated pupils would be required as output. Since, scanning bitmaps can be converted into scanning parcellated pupils, this means that obtaining an accurate Unicom model for any one of the combinations 4-6 would be sufficient.

In the context of this thesis, the prediction accuracy is quantified using PQF deltas that describe the difference between the PQF-values of the prediction by the model and the PQF-values of the desired output:

$$\boldsymbol{\delta}_v^{\text{PQF}} = \mathbf{PQF}_v^{\text{model}} - \mathbf{PQF}_v^{\text{meas}}, \tag{4.1}$$

where $\mathbf{PQF}_v^{\text{model}}$ is the $7 \times m$ matrix with each row containing the values of a PQF-parameter for the prediction by the model at the v-th Field Point (FP) in the slit over m different pitches of the PQF reference feature, $\mathbf{PQF}_v^{\text{meas}}$ is a similar matrix containing the PQF-values for the measurement used a desired output of the model and $\boldsymbol{\delta}_v^{\text{PQF}}$ contains the differences between the entries of both PQF-matrices. Important to note is that not all PQF-parameters depend on the FP, but to enable similar calculations for all parameters these FP-independent parameters will be placed as identical rows in $\mathbf{PQF}_v^{\text{model}}$ for different values of v.

In the current investigation, the prediction error of a Unicom model would be considered small enough if the $\boldsymbol{\delta}_v^{\text{PQF}}$ is contained within 10% of the PQF spec of a machine for all FPs. Therefore, the maximum absolute deviation of $\boldsymbol{\delta}_v^{\text{PQF}}$ from zero over all v and all m pitches is of interest:

$$\boldsymbol{\varepsilon} = \max_v \max_{\text{pitch}} |\boldsymbol{\delta}_v^{\text{PQF}}|, \tag{4.2}$$

where $\boldsymbol{\varepsilon}$ is the 7×1 vector with its entries the maximum absolute PQF error over FPs and pitch and the absolute value is taken element wise. The prediction errors of a Unicom model would thus be small enough in the context of this thesis if the following condition is satisfied:

$$\boldsymbol{\varepsilon} \leq \mathbf{PQF}_{10\%}^{spec}, \tag{4.3}$$

where $\mathbf{PQF}_{10\%}^{spec}$ is the 7×1 vector containing 10% of the maximum allowed value for each PQF parameter.

The Unicom finger insertions happen by movement in the y-direction in the slit. Therefore, the dependency of measured pupils on their y-position in the slit is likely to play a crucial role in any Unicom model. Since combinations 4-6 only use scanning measurements, which are y-integrated, setting up an accurate Unicom model for these combinations might be infeasible. Nevertheless, the goal of this thesis is to construct a Unicom model to perform predictions for at least one of the input-output pairs 4-6 in Table 2 satisfying Equation 4.3.

4.3 Similar problems in literature

DUV, Deep Ultra Violet, lithography is one of the topics for which research treating problems similar to modeling the Unciom's impact on pupils in EUV lithography might be found. In some of ASML's

DUV machines a device called the Unicom (XL) is present [22, 23]. EUV and DUV Unicoms show some similarities as both modules attenuate illumination beams using fingers that can be inserted into a slit at UL. However, DUV uses a different optical setup build with lenses and DUV pupils are smooth instead of comprised of Pupil spots. Therefore, EUV and DUV illumination beams are different. Moreover, DUV Unicoms contain a different setup of fingers with geometries that are not identical to those of the fingers in EUV modules. DUV setups may also include filters, which are not contained in EUV Unicoms because they would absorb almost all EUV light. Thus, although there are some similarities between the EUV and DUV Unicom and methods used in a DUV Unicom model could be of interest when setting up an EUV Unicom model, care should be taken to take the differences between EUV and DUV systems into account.

When investigating previous work on models of slit uniformity corrections it is important to differentiate between models that describe the effects of a uniformity correction devices on the slit and models that describe how to design an optimal slit for IC production within a given space of all slit profiles a machine can produce. For instance, [22] describes an optimization algorithm for the slit profile resulting after taking the Unicom into consideration, but this calculates optimal slit profiles to use during production based on constraints of the type of slit profiles that can be created using the Unicom. One of the reasons why possible intensity profiles of the slit are limited is that the Unicom fingers are not of infinitesimal width and will therefore block quantized parts of slit intensity. In [22] the constraints on possible DUV slit profiles are assumed to already be known. However, these constraints do only specify limits on the slits that can be created and do not detail how the Unicom interacts with the slit or pupils.

On the other hand, in [5] a model is developed that calculates the effects insertions of fingers into an illumination beam have on slit uniformity. The problem solved there is similar to the extend that fingers are inserted to a certain depth into an illumination beam which consists of light moving in multiple directions which are specified by a pupil. The fingers are also inserted at a correction plane (in this thesis unicom level), but effects are studied at reticle level. However, there are some notable differences between the problem solved in the mentioned article and the problem at the center of this thesis. First, the article considers a DUV optical system with lenses and a smooth pupil instead of an EUV system with mirrors and a pupil consisting of multiple pupil spots. The second difference is that this thesis investigates the effects of the Unicom on pupils instead of on the integrated slit profile. This means that the intensities of spots in the pupil should not be summed to a single intensity value for a spot (x, y) in the slit, but be kept as separate spots with each their own intensity. Third and perhaps most important, in this thesis pupil intensities and angles at RL are assumed to be available as measurements, whilst in the article pupils at UL are considered to be known. The pupils at RL and at UL are related and can be mapped to one another, but the pupils are not identical. In reality, the mapping from EUV pupils at RL to pupils at UL depends on the (x, y)-location in the slit. However, the DUV model in [5] does not account for such (x, y) dependent effects. Hence, to map EUV pupils from RL to UL a new mapping would have to be created. Additionally, for the EUV Unicom, a single step mapping just to UL would not be sufficient since multiple fingers are inserted at multiple finger levels.

In [6] a model is introduced to calculate the impact of a uniformity correction using dynamic gray filters through which DUV light is passed. For EUV lithography, passing light though such a filter is not possible because almost all the EUV light would be absorbed by the filter. Nevertheless, the use of a convolution to model the effects of the filters on the light beam might still provide an elegant method to setup a model for the EUV Unicom fingers. However, as the pupil in EUV changes throughout the slit a convolution that assumes a constant pupil shape is not viable.

A model for uniformity corrections based on static filters has also been developed [24], but in this thesis precisely the effect of movable Unicom fingers on the pupil are of interest. Additionally, this model for static filters relies on the same method of convolution as the model for dynamic filter corrections mentioned in [6].

Currently, the movements of Unicom fingers in DUV as well as EUV machines are based on predicted impact on SU, which in turn is based a certain type of measurements [25, 26]. However, these measurements express the effect individual fingers have on SU for a certain amount of insertion. A model to directly predict the impact of the profile of all Unicom fingers on EUV pupils has not been developed yet.

Other areas of optics that share some similarities with the effect the Unicom has on the slit in-

clude the creation of laser beams with a spatially flat intensity profile, which are called flat top or top hat beams. Such flat top intensity profiles are achieved by using beam homogenizers. In fact in EUV lithography machines, mirror configurations already use the fly's eye effect to function as a beam homogenizer and the Unicom is used to aid in the creation of an even flatter y-integrated slit profile. An investigation of laser beam homogenizing is presented in [27], there the suggestion is made that a combination of a fly's eye setup, there called a Köhler integrator, and a random diffuser often produces laser beams with the best homogeneity. However, for the problem at hand no diffuser is present and it is not the output of the fly's eye system that is of interest (that output is in fact already available as measurements with the Unicom fingers extracted). Instead, the effects of the Unicom on the beam passed by the fly's eye setup is the subject of the investigation. What sets the Unicom apart from other beam homogenizers is that the Unicom is only needed to create a flat y-integrated slit profile along the x-direction in the slit. At the same time, the Unicom needs to be flexible enough to correct bundles of light with different angular distributions of illumination beams. Therefore, modelling the Unicom's effects is a different task than the modelling of a traditional beam homogenizer. Those traditional systems consist of different components which have a fixed effect on a predefined bundle of light. Additionally, traditional homogenizers often need to create a flat beam profile in both the x and y-direction. This sets the problem of Unicom modelling apart from the modelling of most other applications where flat top beams are involved like laser micro-machining [28], laser surgery [29] and annealing of photovoltaics [30].

Taking a broader view, most software packages that perform optical simulations, like Zemax [31] and COMSOL [32], are able to calculate how light interacts with objects in the path of a beam of light. The effect of the Unicom fingers falls under the category of partial obstruction of a light beam, which is also the way aperture stops work. However, in this case the light beam is a complicated collection of separate beams and the obstruction happens in an intentionally spatially dependent manner. Therefore, a physics based simulation of the optical effects of the Unicom on pupils would involve combining measurements, Unicom settings and machine design into one simulation and could not be solely handled by a generic optical simulation software. As none of the currently available models are directly applicable to the problem at hand, further investigation into finding a suitable way to model the effects of the Unicom on pupils is warranted.

5 Model setup

In this chapter the Unicom model is build up from its constituent parts, which are introduced one by one. After introducing the model parts, first the setup of the static Unicom model, $\mathcal{M}$, and then the setup of the scanning pupil prediction scheme, SPPS, are presented. $\mathcal{M}$ and SPPS form the main results of this thesis. The final part of this chapter specifies the metrics used in Chapter 6 to verify the accuracy of $\mathcal{M}$ and SPPS.

5.1 Model-type selection

The first step in modelling the impact of the Unicom on pupils consists of choosing a type of model. Since modelling of the Unicom involves measurement data and the propagation of electromagnetic waves, both a data driven as well as a physics based approach could be attempted.

Data driven modelling
First, consider purely data driven modelling, for instance by using deep learning. Purely data driven models, like deep learning, do not assume prior knowledge of the system that is modelled, rather they infer relations within a system based on a data set consisting of input-output data pairs for the model. Advantages of such a data driven method include its flexibility, allowing for the modelling of complicated systems for which interactions are not necessarily well understood, as well as the capability for quick computations once a model is setup. Additionally, since the model learns to predict behavior of a system without prior knowledge, the resulting model might provide new insight into how a system behaves in a certain situation, even though interpreting overall model behavior is likely to be difficult. Drawbacks of such a data driven model are that the model would involve a large amount of parameters to tune, hence model setup would require a large data set. Furthermore such a data set would have to include data points sufficiently distributed over the possible inputs for which the model has to preform predictions.

In the context of Unicom modeling input-output data pairs for model setup would consist of $\mathbf{I^0}$ and the position of Unicom fingers, $\mathbf{d}$, as input and the corresponding $\mathbf{I^d}$ measurement as output. In their most condensed form the input and output measurements are parcellated scanning measurements, both consisting of a matrix $\mathbb{j}$, where $\mathbb{j}_{i,v}$ gives the intensity of the i-th pupil spot measured at the v-th field point. The order of the dimensions of $\mathbb{j}$ would be $10^2 \times 10^1$ and the number of entries in the vector $\mathbf{d}$ would be of the order 10^1. However, the effect of the Unicom on RL pupils on depends on where the light belonging to the pupil spots passed the Unicom. Since the propagation of light associated to a pupil spot is captured by the pupil shape dependent (σ^x, σ^y) coordinates of the spot, these coordinates should be used by the model. Thus, with an intensity, σ^x and σ^y input in $\mathbb{j}$ for each pupil spot, a purely data driven model would consist of roughly 10^3 to 10^4 elements. Therefore, assuming the effect of the Unicom on pupils is non-trivial, it is likely that a large number of measurements would be needed to set up an accurate fully data driven model.

Meanwhile, the number of currently available measurements is limited to a number which is too low for a purely data driven approach. Acquiring the additional measurements needed would involve high monetary costs and require a lot of measurement time on existing machines which is a scarce commodity. Moreover, the available data is limited only a subsection of all possible pupils. A large number possible pupils may never have been used before but also for these pupils prediction capabilities should be created since they could be used in a future production process. Additionally, configurations with multiple Unicom fingers simultaneously fully inserted or extracted are unlikely to have been measured. Hence, purely data driven approach is currently infeasible.

Physics based modelling
The second category is physics based modeling. When it comes to optical modeling there are four main options of modeling approaches to consider: numerical models, physical optics (PO), geometrical optics (GO) and quantum optics (QO). Since for the problem at hand the effects of the Unicom on light in the machine is to be investigated on system level instead of particle level, quantum optical modeling is not applicable.

A numerical model would consist of calculating a solution to Maxwell's equations or a derivative thereof like the Helmholtz equation. Supplied with the appropriate boundary conditions a numerical solver could potentially give a very precise description of the effects of the Unicom fingers on the

bundle of light. Because the FFIs can all be considered mutually incoherent and the EUV light has a wavelength of 13.5nm, which is very small compared to the size of the Unicom, direct numerical solving of the Maxwell's equations becomes both infeasible as well as unnecessary. Infeasible, because the fingers of the Unicom are optically large compared to the light's wavelength leading to high computational cost due to the large domain size. Unnecessary, since EUV light is readily absorbed by most materials, thus it is expected that the Unicom fingers simply block all light that hits them and no notable other effects occur to alter the slit. If no notable wave based effects like changes in polarization are to be expected, solving differential equations that approximate the Maxwell's equations or PO based treatment of the problem are both also not necessary. Therefore the model developed in this thesis makes use of geometrical optics, involving ray tracing and combines this with a parameter based method to allow for flexibility of the model. The parameter can be used to shift the extracted position of all the Unicom fingers simultaneously by the same amount. The extracted positions of fingers might vary between machines due to the manufacturing and calibration process of separate machines. Benefits of such a model are that it is easier to interpret, allows for quick modifications due to changes in machine design and is capable of investigating SU as well because it calculates the effects of the Unicom on a beam of light based on physical concepts.

Because of the choice for a physics based modelling approach, it makes sense to construct a model based on as much of the relevant and available physical information as possible. Static pupils contain more physical information than scanning pupils. Whereas a scanning measurement only contains the y-integrated intensity of the pupil measured at a x-position in the slit, a static measurement also indicates how the pupil intensity changes in the y-direction. As an example: a scanning measurement just indicates that the intensity of a pupil spot is 100% but only from multiple measurements at different places along the y-direction does it become clear that the intensity is distributed as $20\%, 40\%, 30\%, 10\%$ over four equidistant measurement points. These intensity distributions through y might be different for different FFIs as illustrated in Figure 5.1. Since the Unicom fingers are inserted in the y-direction, knowing how intensity is distributed through y provides information that is essential in determining how much light is blocked by a Unicom finger. Therefore, in this thesis a static Unicom model that predicts the effects on static pupils when inserting Unicom fingers, and that uses static pupil measurements, will be constructed.

However, the impact of the Unicom on scanning pupils is still of great interest because during chip production identical scans through the slit are performed. A direct approach in modelling the Unicom's impact on scanning pupils using scanning measurements will not work because these measurements do not provide the distribution of intensity in the y-direction of the slit. Nevertheless, if a static Unicom model can be constructed that accurately predicts the effects of the Unicom on static pupils, the predicted effects on static pupils may be similar to the effects on scanning pupils. To transfer predicted effects on static pupils to scanning pupils, at least some form of integration through y would be needed. If integrating all static measurements through y at a fixed x-position in the slit results in a pupil similar to the scanning measurement, the predicted static pupils by the static model can be integrated in similar fashion to obtain a prediction for a scanning pupil. If the integrated static measurements differ from the scanning measurements, a more advanced method of integration or a way to introduce information from a scanning measurement might be needed when predicting the effect of the Unicom on scanning pupils. Thus, in this thesis a scheme will be created involving integration through y and a few other tricks, enabling the use of the static Unicom model's predictions when predicting the Unicom's effects on scanning pupils.

5.2 Obtaining data

In order to setup a static measurement based Unicom model, two types of static bitmap pupil measurements are needed. The first consists of an array $\mathbb{I}^{\mathbf{0}}$ with size $N_{\sigma^x} \times N_{\sigma^y} \times N_x \times N_y$, where $\mathbb{I}^{\mathbf{0}}_{i,j,v,w}$ gives the intensity for the pixel in the j-th row and i-th column of the bitmap pupil measured at the v-th x-position and the w-th y-position in the slit where all Unicom fingers were extracted. The second, consists of a similar array of measurements $\mathbb{I}^{\mathbf{d}}$ with the only difference being that these measurements were performed with the Unicom fingers inserted to the positions specified by $\mathbf{d}$. The former array is used as input of the model and the latter is used to compare to model output for verification of the model's performance. Both measurements need not necessarily be measured at exactly the same x- and y-positions in the slit, but some overlap should exist such that model output and measurements can

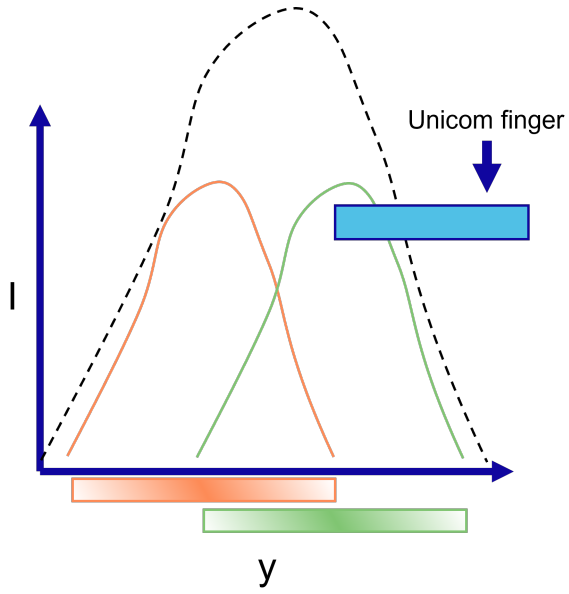

Fig. 5.1: Illustration of the slit intensity profile through y of two FFIs (orange and green) and joint intensity profile of the FFIs (dashed) for fixed x. The fraction of an FFI's intensity that is blocked by the Unicom finger depends on that FFI's intensity profile through y.

be compared without the involvement of interpolation methods. Further requirements are that both measurements are performed for the same pupil, as a change in pupil implies a change in beam shape, which hence impacts the effects created by the Unicom. Additionally, the same lithography machine should be used during both measurements since machine to machine variations due to their manufacturing process are likely to have effects on the beam shape, its position and the position of the Unicom.

To utilize a static Unciom model in the setup and verification of a model that predicts the effect of the Unicom in scanning pupils, two additional types of scanning measurements are required. These two types of scanning measurements are essentially equivalent to the two types of static measurements, with the only difference that the last dimension of the arrays are dropped and the arrays consist of entries $\mathbb{J}^{*\mathbf{d}}_{i,j,v}$ which give scanning intensities. Again the measurement with Unicom fingers extracted will serve as input to the model and the measurement with Unicom fingers inserted is used for the purpose of verification. Here as well, measurements should be performed on the same machine with the same pupil setting as the static measurements.

A MATLAB script was setup to comb the database of available measurements to first find the required static measurement pairs and preferably subsequently find a compatible pair of scanning measurements. In order to do this, the script first identifies if static measurements have been performed on a machine with the Unicom fingers fully extracted. This is done by opening ISPQ/IPD measurement files and extracting the measurement type as well as the Unicom finger positions. If a static retracted Unicom measurement is found the machine number and pupil type are stored alongside the location of the file. In the next run the script finds static measurements where the Unicom fingers have been inserted that correspond to the previously found measurements with the fingers extracted. This is done by checking the measurement type, machine number, pupil type and non-zero finger positions. In two subsequent runs the algorithm finds corresponding scanning measurement pairs.

Since both the static measurement type and measurements with the Unicom fingers fully extracted are mainly used for investigative purposes by ASML, few measurements of either type exist. In combination with the requirements of measurements being performed on identical machines with equal pupil settings this meant that at the time of investigation no complying static ISPQ measurement pairs were found. The restriction that limited the search most was the full extraction of the Unciom fingers in one of the measurements. However, one pair of static IPD measurements as well as a corresponding scanning measurement set could be obtained. These were produced in the past, exactly for an investigation regarding Unicom's impact. This set of IPD measurements was used during the setup and verification of the Unicom model presented in this thesis.

5.3 Data pre-processing

Here the first step will be made in describing the parts of the Unicom model. These parts will be described as processing blocks, consisting of a collection of processing steps. To some extent both the processing blocks as well as the processing steps are modular and can be used to build Unicom models with different configurations. At the end of this chapter the configuration of the final iteration of the Unicom model constructed in this thesis will be presented. Notable previous iterations of the model can be found in Appendix B.

Zero forcing
Both the static as well as the scanning IPD measurements contain negative values for intensity for some pixels, this is simply an artifact of the way measurements are performed and stored. However, negative intensities are non-physical and likely to lead to strange behavior when used for setup of or predictions with a Unicom model. Therefore, the first step of pre-processing consists of setting these negative values to an intensity of zero. This is unlikely to have adverse effects on calculations, like parcellation, which involve local sums of pixel intensity, because the magnitudes of these negative intensity values are 10^2 times smaller when compared to the magnitudes of pixels on which pupil spots are measured. When added, the magnitude of negative intensity in the used static measurement was 1.7% of the magnitude of added positive intensity.

Data filtering
A subsequent step in pre-processing for static data is choosing for which (x, y) positions in the slit measured bitmap pupils should be included in calculations. Pupils measured close to the curved y-edges of the slit are measured at the tails of the total intensity profile through y, as depicted in Figure 5.1, which leads to lower signal to noise ratios as well as higher impact of measured stray light on the bitmap pupil. Hence, a case could be made to exclude these measurements when using a Unicom model. For some early iterations of the static Unicom model this option was investigated. However, in later iterations of the Unicom model a decision was made to include the bitmap pupils from the edges of the slit as well. The reason for the inclusion is that, although the distribution of intensity in such an edge pupil might be less accurately measured on its own, these pupils do indicate the tails of the FFIs's intensity distributions through y. Therefore, they include important information about the amount of light that is blocked at the transition from the middle of the slit to the borders of the slit, which is mainly important when looking at the amount of light blocked by the Unicom for a scanning pupil that is measured over the full y range. Furthermore, whereas the distribution of intensity in edge pupils might be impacted by a larger ratio of noise, in relation to pupils which are adjacent in y the intensity values of all their pixels are fairly small. This means that in combination with the availability of multiple other pupil measurements on the slope of an FFI's intensity profile through y, the impact of noise on the y-integrated intensity of an FFI (and thus pupil spot) will be limited. Meanwhile, including these measurements prevents the need for extrapolation to determine intensity contained in the tail parts of an FFI's intensity profile. As the intensity drop at the x-boarders of the total slit at RL fall outside of the used part of the slit, the problem with decreasing signal to noise ratios is not encountered in the x-direction and in particular all scanning pupil measurements can be used without this pre-processing step.

Slit interpolation
Since the Unicom model in this thesis is based on the spatially dependent effects of the Unicom fingers on the illumination beam, it is logical to consider methods to include as much spatial information as possible. The number of static measurements in both the x- and y-direction in the slit is limited to such a degree that the spatial knowledge about where Unicom fingers are located inside the slit at UL is far more precise than the step size between two adjacent pupil measurements. Therefore, if the blocked part of the light in pupils would only be calculated at the measurement positions, the more precise knowledge of the Unicom finger positions would be discarded. Discarding this information would result in unnaturally discrete behavior of the model for y-integrated pupils. For instance, consider the situation in Figure 5.2. If a Unicom finger would be positioned in y such that it just misses the bundle of light ending up at the second measured y-position in the slit, then up to the precision of known Unicom finger positions the domain in y where the intensity ends up being 0 is known. However, due to the

larger step size between measurements only the intensity in the pupil on the edge of the slit will be zero and during integration over y the intensity between the two measurement points is greatly overestimated because some weighted average of the two measurement intensities, which is blind to the exact finger position, is considered over the first interval. On the other hand, interpolation of the measurements will produce errors in intensity when compared to the exact intensity profile on the machine, so a trade off can be made between interpolation errors and errors due to effectively discarding resolution of the Unicom finger positioning.

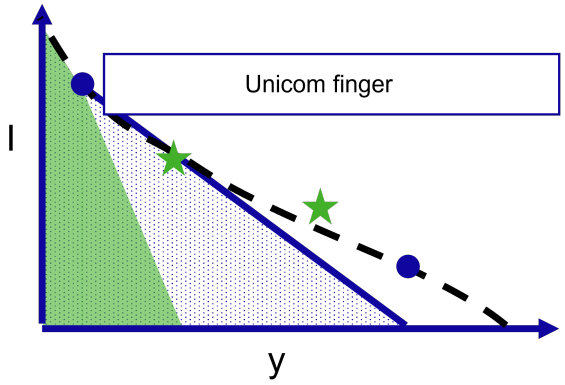

Fig. 5.2: Illustration of the area obtained after integration through y with only the original measurements (blue dots, blue dotted area) and with interpolation of measurements (green stars & blue dots, green area). The areas are obtained after forcing measurements to zero where the Unicom finger is inserted. The dashed line indicates the exact intensity profile.

To pick the interpolation method for interpolation of the slit the methods 'linear', 'nearest', 'cubic', 'makima' and 'spline' of MATLAB's griddedInterpolant function were considered, their exact descriptions can be found in [33]. Performance of these methods were investigated by generating interpolated FFI intensity profiles over the entire slit. This was done for parcellated static pupil measurements which, although not all pupil spots are parcellated properly everywhere in the slit, guarantee for most FFIs that a slit profile can be created without the larger dependency on the exact location of pupil spots that is present for pixels in a bitmap pupil. Even though the slit is curved, its curvature is known from design and pupil measurements are performed in such a way that measurement points form a rectangular grid with one step size in the x- and another step size in the y-direction when the curvature is removed. By design the slit also has approximately, but not exactly, the same intensity profile in y in this rectangular coordinate system at different x-positions. Hence, interpolation can be performed on a rectangular grid and the shape of the intensity profile that it should approximate is well understood. The shape of such an intensity profile in y-direction consists of flat tails followed by a steep increase in intensity and a smoothly varying top surface. Therefore, an interpolation method should be able to flatten tail regions as well as capture a steep slope and a smoothly varying surface.

On the criterion of requiring a smoothly varying surface both the 'linear' and 'nearest' interpolation method are excluded. The 'linear' interpolation method connects measurement points using linear surfaces, which at connecting edges introduce sharp changes in gradients. When using the 'nearest' method, values at gridpoints that are evaluated with interpolation are obtained by picking the value of the measurement that is closest which makes the interpolation non-smooth. Left are the 'cubic', 'makima' and 'spline' interpolation methods. All of the remaining methods are able to handle smoothly varying surfaces as well as steep slopes. However, the 'cubic' and 'spline' method have a tendency to suffer from undulation when steep slopes are introduced even though the top surface of the intensity profile is only varying slowly. The 'makima' or modified Akima method is precisely designed to somewhat mitigate these undulations whilst still being able to generate smoothly varying surfaces. The original Bi-variate Akima piecewise cubic interpolation method is introduced in [34] and the modifications made in the 'makima' method can be found in [35].

The static Unicom model constructed in this thesis employs the modified Akima method to interpolate the intensity profiles of the FFIs through the entire slit. In this context bitmap pupils are used

and instead of every pupil spot being associated to an FFI, there is an FFI for each pixel of the bitmap. Hence, there are $N_{\sigma^x} \times N_{\sigma^y}$ FFIs, $\text{FFI}_{i,j}$. This likely makes FFIs more dependent on pupil spots moving in the pupil when changing location in the slit because small movements will mean that spots move from one pixel to the next. However, pupil spots fill up multiple pixels at once and the movements of spots that depend on the measurement position in the slit are quite slow, thus changes in bitmaps FFIs will with the right resolution still be smooth. The interpolation method leaves the intensity at measurement points unchanged. Hence, to allow for direct comparison of the model output with pupils measured with the Unicom finger inserted, the model gives the user the option to input, ω, the number of times the grid spacing is halved in both directions. Thus if the user specifies $\omega = 3$ times refinement, the grid spacing is reduced by $2^3 = 8$ times and values on grid points between the original measurements will have been obtained through modified Akima interpolation.

Slit shaping
After interpolation the grid of the slit is transformed to account for the shape of the slit. During this process, only the (x, y) coordinates are altered leaving the intensity values unchanged. Subsequent calculations of the effects of the Unicom on the slit are performed on the curved grid. This transformation has no impact on the energy density over scans through y.

5.4 Unicom mask creation

To model the spatial effects of the Unicom on the light beam, the shape and location of the Unicom fingers need to be know. The setup of Unicom fingers considered in this thesis consists of two levels of fingers, the first of which is located a little lower in the z-direction in the machine (and is thus encountered first by the light) than the second.

Vertex calculation
The Unicom fingers are 3D objects, but due to their shape often only a couple of 2D profiles in the XY-plane need to be considered at different heights, z, to fully capture the effects of the fingers on the light beam. A simple diagram depicting how two levels of Unicom fingers might already be described by 4 2D profiles is shown in Figure 5.3.

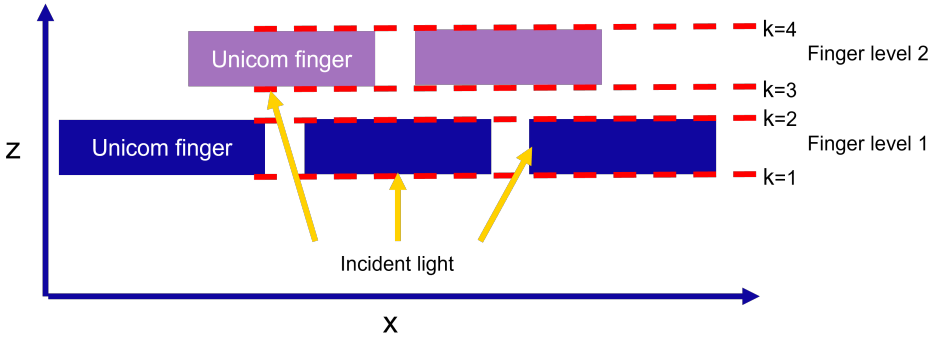

Fig. 5.3: Crossection, XZ-plane, of 2 levels of Unicom fingers and incident light with various angles. Red dashed lines indicate the top and bottom XY-profiles for both levels of Unicom fingers which are labelled by k.

Under the conditions that the angles of the incident light are sufficiently small in comparison to the ratio of the width (x-direction) or the length (y-direction) of the fingers and their height, all light blocked by a finger will either also hit the bottom or the top 2D profile of the same finger. Since the fingers are designed to be wide and long to be able to block light and the maximum and minimum angles of the incident light are small, in the Unicom model the fingers are described by a limited number of 2D profiles containing multiple fingers. The coordinates of vertices of the Unicom fingers in these profiles can be described as:

$$\mathbf{X}^u_k(\mathbf{0}) = \begin{pmatrix} x^u_{k,1}(\mathbf{0}) & x^u_{k,2}(\mathbf{0}) & \cdots & x^u_{k,a(k)\cdot N(k)}(\mathbf{0}) \\ y^u_{k,1}(\mathbf{0}) & y^u_{k,2}(\mathbf{0}) & \cdots & y^u_{k,a(k)\cdot N(k)}(\mathbf{0}) \end{pmatrix}, \tag{5.1}$$

where $\mathbf{X}_k^u(\mathbf{0})$ is a $2 \times L(k) = a(k) \cdot N(k)$ matrix, with the first row containing the x-coordinates of each vertex describing the fingers in the k-th 2D profile for fully extracted fingers, $\mathbf{0}$, the second row contains the corresponding y coordinates, the superscripts ^{u} indicate that these coordinates belong to profiles at UL, $a(k)$ gives the number of vertices needed to describe a single Unicom finger in the 2D profile, which might depend on the profile in question and $N(k)$ is the number of fingers in the profile.

The second piece of information that is needed for a full geometrical description of the Unicom is the z-coordinate, height, of each of the Unicom profiles in the machine. Defining these with respect to RL, the following is obtained:

$$\mathbf{\Delta z} = \begin{pmatrix} \Delta z_1 \\ \Delta z_2 \\ \vdots \\ \Delta z_M \end{pmatrix} = \begin{pmatrix} z^r - z_1^u \\ z^r - z_2^u \\ \vdots \\ z^r - z_M^u \end{pmatrix}, \tag{5.2}$$

where $\mathbf{\Delta z}$ is the vector of M entries of the differences in height z between RL and the k-th Unicom profile and the superscript ^{r} indicates that a coordinate belongs to RL. The coordinates of the vertices of the Unicom fingers can be calculated using the equations that specify them for a specific machine in the corresponding design files.

Finger insertion

To setup the moved profile of the fingers, described by a vector $\mathbf{d}$ with N_v entries (equal to the total number of fingers of all Unicom levels) indicating distance moved with respect to the fully extracted ($\mathbf{0}$) position, addition of an entry in $\mathbf{d}$ to all y coordinates corresponding to the same finger suffices:

$$\mathbf{X}_k^u(\mathbf{d}) = \mathbf{X}_k^u(\mathbf{0}) + \begin{pmatrix} \mathbf{0}_{N(k)}^\intercal \otimes \mathbf{e}_{a(k)}^\intercal \\ \mathbf{d}(k)^\intercal \otimes \mathbf{e}_{a(k)}^\intercal \end{pmatrix}, \tag{5.3}$$

with $\mathbf{d}(k)$ the entries of $\mathbf{d}$ corresponding to the fingers in profile k, $\mathbf{e}_{a(k)}$ the vector of $a(k)$ ones and $\otimes$ the Kronecker product (see Appendix A).

Note that during the setup of the description of the Unicom model a few additional assumptions have been made. The obvious ones are that the manufactured Unicom fingers perfectly resemble the design of the Unicom fingers and that these designs can accurately be captured by a limited number of vertices. More implicit assumptions are that the position of the Unicom fingers after movement can be considered static, that the height of the Unicom fingers does not change when they are moved and that effects like expansion of the fingers when they are heated up by insertion into the EUV beam only has negligible effects on their profiles. These effects although present, were stated by designers of the Unicom to be of limited importance to the blocking of light by the Unicom and as such are omitted in this thesis during the setup of the Unicom model.

5.5 Unicom shadow projection

With the measurements of the pupils processed and the description of the Unicom set up, the effect of the Unicom on the pupils can be modelled. There are two equivalent ways to go about this: the first involves mapping the grid of measurements at RL to UL to figure out where intensities are blocked and the second involves mapping the vertices of the Unicom on UL to RL. In both cases a mapping needs to be performed for each combination of angles θ^x and θ^y belonging to one FFI.

For the Unicom model in this thesis, using a mapping of the Unicom finger profiles from UL to RL was chosen due to its computational efficiency. The design of the Unicom considered in this thesis guarantees that the number of vertices in all Unicom profiles combined is lower than the number of points on the interpolated measurement grid. Although mapping the Unicom to RL or mapping the measurements to UL are equivalent when calculating the effect of the Unicom on pupils, mapping a lower number of points will result in faster computations. Therefore, the Unicom model maps the Unicom profiles from UL to their FFI dependent shadows on RL.

Simple projection

Now assume that the conic divergence of FFIs is accounted for by the movement of pupil spots in the measured bitmaps, which depend on the (x, y) location in the slit. Then the translation in x- and

y-direction of a point in a Unicom profile when mapping it to its shadow is given by the tangent of the angle multiplied by the distance traveled in z as depicted for the x direction in Figure 5.4. The translation function thus becomes:

$$\mathbf{g}(\sigma^x, \sigma^y, \Delta z) = \Delta z \begin{pmatrix} \tan(\theta^x(\sigma^x)) \\ \tan(\theta^y(\sigma^y) + \text{CRAO}) \end{pmatrix}, \tag{5.4}$$

with the vector function $\mathbf{g}$ giving the translation of the (x, y) coordinate pair, CRAO the chief ray at object, which denotes the angle in y direction under which the full illumination beam is tilted when propagating to the reticle and $\theta^x(\sigma^x)$ and $\theta^y(\sigma^y)$ are the angles in x- and y-direction respectively belonging to the FFI under consideration. θ^x can be found from:

$$\theta^x(\sigma^x) = \arcsin\left(\frac{\sigma^x NA}{M_x}\right), \tag{5.5}$$

and θ^y can be obtained from:

$$\theta^y(\sigma^y) = \arcsin\left(\frac{\sigma^y NA}{M_y}\right), \tag{5.6}$$

where the definitions of σ-space coordinates, given in Equation 3.7 are simply inverted with $n = 1$ because the light propagates through vacuum in the machine.

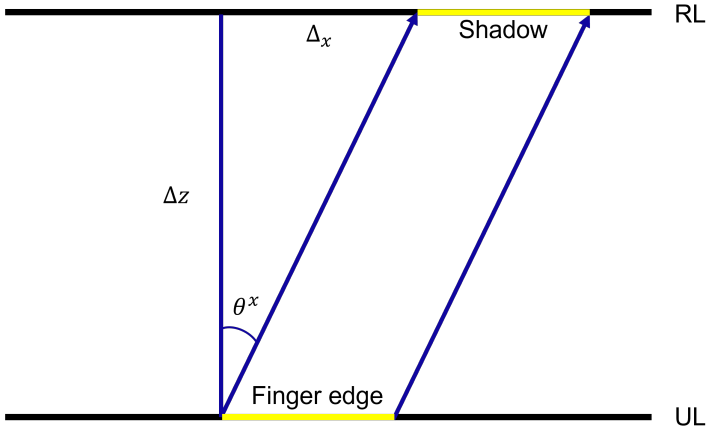

Fig. 5.4: Geometry of the projection of the edge of a Unicom finger (yellow) from UL to its shadow (yellow) on RL based on the angle θ^x and the distance between the two planes.

Utilizing the function $\mathbf{g}$, the vertices of the Unicom profiles at UL can now be mapped to the vertices of their shadows on RL for each FFI:

$$\widehat{\mathbb{X}}^r_{i,j,k}(\mathbf{d}) = \mathbf{X}^u_k(\mathbf{d}) + \left(\mathbf{g}(\sigma^x_i, \sigma^y_j, \Delta z_k) \cdot \mathbf{e}^{\mathsf{T}}_{a(k)\cdot N(k)}\right), \tag{5.7}$$

with $\widehat{\mathbb{X}}^r_{i,j,k}(\mathbf{d})$ the $2 \times a(k) \cdot N(k)$ matrix of vertices of the shadow of the k-th Unicom profile in $\text{FFI}_{i,j}$ with the finger positions specified by $\mathbf{d}$. Note that here σ^x_i and σ^y_j depend on the indices i and j because $\text{FFI}_{i,j}$ corresponds to a pixel in the pupil bitmap, which is located at a specific σ^x and σ^y position in the pupil.

Advanced projection

Although the simple projection of Unicom fingers to their shadows is insightful, the assumption that the conic divergence of FFIs is accounted for by the movements of pupil spots throughout the pupil might not be fully warranted. The pupil measurements are performed at wafer level, meaning that light has already passed the POB. One of the functions of the POB is to remove some spatial dependence of the propagation of light in the slit on the (x, y)-position in the slit. Although measurements used had already been processed to resemble pupils at RL, the divergence of FFIs has not been taken into account in this pre-processing. Therefore, divergence of the FFIs is not yet accounted for and should

be added. The vector description of light moving from the slit at RL further through the machine to the POB is given by [36]:

$$\begin{pmatrix} x \\ y \\ z \end{pmatrix} = \begin{pmatrix} x^r \\ y^r \\ z^r \end{pmatrix} + \mu \begin{pmatrix} \sin(\theta^x + \gamma(x^r)) \\ \cos(\theta^x + \gamma(x^r)) \cdot \sin(\theta^y + \beta(y^r) + \text{CRAO}) \\ \cos(\theta^x + \gamma(x^r)) \cdot \cos(\theta^y + \beta(y^r) + \text{CRAO}) \end{pmatrix}, \tag{5.8}$$

where $\gamma(x^r)$ and $\beta(y^r)$ are the spatially dependent contribution to the propagation angle of a FFI, which describe the divergence of a FFI as shown in Figure 3.19 and μ is a scalar multiplier. $\gamma(x^r)$ is given by:

$$\gamma(x^r) = \arctan\left(\frac{x^r}{x_c}\right), \tag{5.9}$$

with x_c the distance from the slit on RL to its point of convergence in x, which is called the entrance pupil. Similarly $\beta(y^r)$ can be found from:

$$\beta(y^r) = \arctan\left(\frac{y^r + M_y \cdot \text{BBO}}{y_c}\right), \tag{5.10}$$

with BBO the distance from the long side of the smallest rectangular box that fits around the slit to the center point of that box and y_c the distance from the slit on RL to its point of convergence in y.

Since Equation 5.8 is specified for points on RL, whereas a mapping is needed from known Unicom vertices on UL to RL, the vector description needs to be reworked to be able to input a starting point, in this case a Unicom vertex, at a different height z. To this end, first the description for the central vectors of pupils can be considered by setting θ^x and θ^y to zero and subsequently dividing the vector of direction by its third entry. By setting μ to $-\Delta z$, a set of equations to map from a point at RL to its corresponding point on UL can be found:

$$\begin{aligned} \begin{pmatrix} x^{u\odot} \\ y^{u\odot} \\ z^{u\odot} \end{pmatrix} &= \begin{pmatrix} x^{r\odot} \\ y^{r\odot} \\ z^{r\odot} \end{pmatrix} - \Delta z \begin{pmatrix} \tan(\gamma(x^{r\odot}))/\cos(\beta(y^{r\odot}) + \text{CRAO}) \\ \tan(\beta(y^{r\odot}) + \text{CRAO}) \\ 1 \end{pmatrix} \\ &= \mathbf{x}^{r\odot} - \Delta z \begin{pmatrix} x^{r\odot}/(x_c \cos(\beta(y^{r\odot}) + \text{CRAO})) \\ \tan(\beta(y^{r\odot}) + \text{CRAO}) \\ 1 \end{pmatrix} \end{aligned}, \tag{5.11}$$

where the superscript $\odot$ indicates that the origins of pupils are being considered and in the last line the expression for $\gamma(x^{r\odot})$ was plugged in to further simplify the equation. By calculating the inverse function of this system of equations, the function $\mathbf{f}(\mathbf{x}^{u\odot}, \Delta z) = \mathbf{x}^{r\odot}$ can be obtained to map the center point of pupils on UL to the corresponding point on RL, this is called pupil origin mapping. Here the $\mathbf{x}$ vectors contain the x, y and z coordinates. Using the first two outputs of the vector valued function $\mathbf{f}$, a function can be constructed to give the translation in x- and y-direction when mapping from a point on UL to a point on RL including the dependency on the angles in the pupil:

$$\mathbf{h}(\mathbf{x}^u, \sigma^x, \sigma^y, \Delta z) = \Delta z \begin{pmatrix} \tan(\theta^x(\sigma^x) + \gamma(f_1(\mathbf{x}^u, \Delta z)))/\cos(\beta(f_2(\mathbf{x}^u, \Delta z)) + \text{CRAO}) \\ \tan(\theta^y(\sigma^y) + \beta(f_2(\mathbf{x}^u, \Delta z)) + \text{CRAO}) \end{pmatrix}, \tag{5.12}$$

where $\mathbf{h}$ is a vector valued function with its first entry the translation in the x-direction and its second entry the translation in the y-direction, f_1 and f_2 indicate the first and second entry respectively of the vector outputted by the vector valued function $\mathbf{f}$. Utilizing $\mathbf{h}$, the coordinates for the shadows of the vertices of the Unciom fingers for $\text{FFI}_{i,j}$ with finger insertion v under advanced projection can be calculated through Unicom profile mapping:

$$\mathbb{X}^r_{i,j,k}(\mathbf{d}) = \mathbf{X}^u_k(\mathbf{d}) + \begin{pmatrix} \mathbf{h}(\mathbf{x}^u_{k,1}(\mathbf{d}), \sigma^x_i, \sigma^y_j, \Delta z_k) & \cdots & \mathbf{h}(\mathbf{x}^u_{k,a(k)\cdot N(k)}(\mathbf{d}), \sigma^x_i, \sigma^y_j, \Delta z_k) \end{pmatrix}, \tag{5.13}$$

with $\mathbb{X}^r_{i,j,k}(\mathbf{d})$ the $2 \times a(k) \cdot N(k)$ matrix of vertices of the shadow of the k-th Unicom profile in $\text{FFI}_{i,j}$ with the finger positions specified by $\mathbf{d}$. Note that implicitly the number of vertices given for the Unicom profiles was assumed to be sufficiently high to capture the slowly varying yet non-linear spatial dependency of the advanced projection of Unicom fingers. This would ensure that the small distortion effects on the shape of the fingers's shadows with respect to the actual shapes of the fingers are accounted for.

5.6 Intensity blocking

When the shadows at RL are calculated the next step in the Unicom model consists of blocking the intensity of FFIs at RL in exactly those grid points that are contained in the shadows of one or multiple Unicom profiles. To this end the coordinates of vertices in shadows can be used to construct simple polygons that describe the area shaded by a single Unicom finger in a specific FFI:

$$F_{i,j,k,p}(\mathbf{d}) = \text{Polygon}\left(\left\{\begin{pmatrix}\mathbb{X}^r_{i,j,k,1,q}(\mathbf{d})\\ \mathbb{X}^r_{i,j,k,2,q}(\mathbf{d})\end{pmatrix}\middle| q = 1 + a(k)(p-1)\ldots a(k)p\right\}\right), \tag{5.14}$$

here $F_{i,j,k,p}(\mathbf{d})$ is the polygon obtained for $\text{FFI}_{i,j}$ by linearly connecting the adjacent (the vertices are assumed to be structured such that adjacent vertices share an edge), as well as the first and the last, vertices of the shadow on RL belonging to the profile of the p-th finger in the k-th Unicom profile for finger movements specified by $\mathbf{d}$ and taking the interior of the closed loop, and the two indices added to $\mathbb{X}^r_{i,j,k}(\mathbf{d})$ indicate the row and the column of the matrix respectively to obtain a single x or y coordinate for one vertex. Each finger, p, is described by $a(k)$ vertices, which are given by $a(k)$ adjacent columns in $\mathbb{X}^r_{i,j,k}(\mathbf{d})$, thus the columns indexed by q can be used to construct a polygon of each finger. By subsequently taking the union over all M Unicom profiles and all $N(k)$ fingers, the shaded area of a $\text{FFI}_{i,j}$ at RL can be obtained:

$$A_{i,j}(\mathbf{d}) = \bigcup_{k=1}^{M}\bigcup_{p=1}^{N(k)} F_{i,j,k,p}(\mathbf{d}), \tag{5.15}$$

with $A_{i,j}(\mathbf{d})$ the shaded area of $\text{FFI}_{i,j}$ at RL for finger insertions specified by $\mathbf{d}$. This formulation of the shaded areas can then be used to decide where in each FFI the intensity at RL should be set to zero because the path of the light from the PFM towards that region is blocked by the Unicom fingers at UL:

$$\mathbb{I}^{\mathbf{d}}_{i,j,v,w} = \mathbb{I}^{\mathbf{0}}_{i,j,v,w} \cdot (1 - \mathbb{1}_{A_{i,j}(\mathbf{d})}(x_v, y_w)), \tag{5.16}$$

where $\mathbb{I}^{\mathbf{d}}_{i,j,v,w}$ is the intensity value at the pixel in the i-th column and j-th row of the bitmap pupil at the v-th x- and w-th y-position of the grid points of the slit after interpolation with the effect of the Unicom (insertion of fingers described by $\mathbf{d}$) by blocking a part of the illumination taken into account, $\mathbb{I}^{\mathbf{0}}_{i,j,v,w}$ is the intensity of the same pixel with the Unicom fingers fully extracted, which is obtained after interpolation of the slit and $\mathbb{1}_{A_{i,j}(\mathbf{d})}(x_v, y_w)$ is the indicator function (see Appendix A) and x_v and y_w give the x and y-coordinate of the grid points of the slit after interpolation respectively. After this procedure, the modeling of the effects of the Unicom on static pupils is done.

5.7 Pupil integration

Since the main goal of this thesis entails the development of a model to predict the impact of the Unicom on scanning pupils, making a connection between static pupils and scanning pupils may allow the necessary insight to construct a scanning Unicom model.

Trapezoidal method

One of the straightforward ways to transform a set of static pupils into a set of scanning pupils is by using numerical integration to integrate pixels in the pupil in the y-direction of the slit. Numerical integration can be performed by using the trapezoidal method to obtain a y-integrated pupil which should approximate a scanning pupil:

$$\mathbb{J}^{\mathbf{d}}_{i,j,v} = \sum_{w=1}^{N_y}(y_w - y_{w-1})\frac{\mathbb{I}^{\mathbf{d}}_{i,j,v,w-1} + \mathbb{I}^{\mathbf{d}}_{i,j,v,w}}{2}, \tag{5.17}$$

with $\mathbb{J}^{\mathbf{d}}_{i,j,v}$ the intensity of the pixel in the i-th column and j-th row of the y-integrated bitmap pupil at the v-th location in the grid of the interpolated slit for finger insertions specified by $\mathbf{d}$. Note that to get a good approximation of scanning pupils by integrating static pupils, the dose produced by the source during measurements of static pupils at two neighboring grid points and the dose produced during the scan over the interval of the slit enclosed by these points, should have a constant ratio for all grid points. Therefore, because the scanning velocity is constant during scanning pupil measurement and

thus the dose produced at each interval of the slit scan be assumed approximately constant, the dose produced during each static measurement should be the same. Information about the dose produced during measurements was available but differences in dose between different static measurements were small. However, limiting the numerical integration to the trapezoidal method might not necessarily result in the most accurate transformation of static pupils into integrated pupils that resemble the measured scanning pupils. In practice some differences between the shapes of the pupil spots in the integrated pupils and in the measured scanning pupils were observed. Hence a more flexible approach based on ordinary least squares, OLS for short, optimization was also investigated.

OLS optimization

To allow for more flexibility in the way that static pupils are summed to form integrated pupils the latter can be represented as a general weighted sum:

$$\mathbb{J}^{\mathbf{d}}_{i,j,v} = \sum_{w=1}^{N_y} \tau_w \cdot \mathbb{I}^{\mathbf{d}}_{i,j,v,w}, \tag{5.18}$$

where τ_w is the weight of the w-th static measurement in the y-direction. By stacking all columns of bitmap pixel intensities of $\mathbb{J}$ on top of each other for a specific v, the bitmap pupil can be vectorized to $\boldsymbol{\psi}$. By repeating the same stacking for all static bitmap pupils for the same v in $\mathbb{I}$, N_y vectors ϕ_w can be obtained. Placing each ϕ_w in its corresponding column in a matrix, the $N_{\sigma^x} \cdot N_{\sigma^y} \times N_y$ matrix $\boldsymbol{\Phi}$ is obtained. The OLS cost function, $\mathcal{L}(\boldsymbol{\tau})$, for the parameters τ_w in the linear regression model described by Equation 5.18 is now given by:

$$\mathcal{L}(\boldsymbol{\tau}) = ||\boldsymbol{\psi} - \boldsymbol{\Phi}\boldsymbol{\tau}||_2^2, \tag{5.19}$$

with $||\cdot||_2$ the L_2 norm (see Appendix A. Since the N_y vectors ϕ_w belong to static pupil measurements at different locations in the slit and have $N_{\sigma^x} \cdot N_{\sigma^y} >> N_y$ entries, they are readily linearly independent. Hence $\boldsymbol{\Phi}$ has full rank and the solution to the OLS optimization can be found as:

$$\hat{\boldsymbol{\tau}} = \arg\min_{\boldsymbol{\tau} \in \mathbb{R}^{N_y}} \mathcal{L}(\boldsymbol{\tau}) = (\boldsymbol{\Phi}^\intercal \boldsymbol{\Phi})^{-1} \boldsymbol{\Phi}^\intercal \boldsymbol{\psi}, \tag{5.20}$$

where $\text{argmin}_{\boldsymbol{\tau} \in \mathbb{R}^{N_y}}$ indicates that the value for $\boldsymbol{\tau} \in \mathbb{R}^{N_y}$ is picked that minimizes the cost function. The vector $\boldsymbol{\tau}$ and Equation 5.18 can then be used to not only integrate the static pupils at the v-th x-position in the slit, but also at all the other x-positions in the slit.

The data that can be used to obtain the $\boldsymbol{\tau}$ vector should consist of scanning as well as static pupil measurements for an identical pupil and machine with the Unicom fingers fully extracted in order to capture the full y-length of the slit. The calculated $\boldsymbol{\tau}$ can then be used to transform the output of the static Unicom model from static pupils to integrated pupils. Note that if the trapezoidal method would minimize the cost function, the obtained τ_w values would simply consist of the weights of the trapezoidal method, hence this method is contained in this optimization.

Possible additional modifications to the OLS optimization include thresholding to filter out pixels with an intensity below a certain value by setting entries in $\boldsymbol{\psi}$ and $\boldsymbol{\Phi}$ temporarily to zero in Equation 5.20 when determining $\boldsymbol{\tau}$. When followed by using Equation 5.18 with the original intensities this means that low intensity values, supposedly values due to noise, are ignored in the optimization process. A second modification also entails similar thresholding but for pixels where the magnitude of the residuals of the integration, $\boldsymbol{\psi} - \boldsymbol{\Phi}\boldsymbol{\tau}$, remain above a certain intensity value after OLS optimization of the parameter $\boldsymbol{\tau}$. Again setting corresponding points to zero, in a second round of optimization new values for $\boldsymbol{\tau}$ are obtained where the dependence on the pixels with the largest remaining residuals was filtered out. This means that misalignment of pupil spots, causing the illuminated pixels in both used measurements to differ, are ignored.

Equation 5.18 might also be altered to include the squared intensity values of $\mathbb{I}$ and perform regression with linear as well as quadratic features. By including quadratic features, higher order effects may also be captured by the transformation from static to integrated pupils if needed. To this end the new sum will become:

$$\mathbb{J}^{\mathbf{d}}_{i,j,v} = \sum_{w=1}^{N_y} \tau_w \cdot \mathbb{I}^{\mathbf{d}}_{i,j,v,w} + \sum_{w=N_y+1}^{2N_y} \tau_w \cdot \left(\mathbb{I}^{\mathbf{d}}_{i,j,v,w}\right)^2. \tag{5.21}$$

The matrix $\mathbf{\Phi}$ will then have N_y additional columns consisting of vectors ϕ_w^2 and the rest of the optimization process stays identical. In this regression with higher order features as well, either of the thresholding modifications might be utilized. Note that if either method of OLS optimization is chosen to transform static pupils into integrated pupils, it is important to verify if the weights $\boldsymbol{\tau}$ found for a specific x-position in the slit generalize to a transformation that is also suited to the other x-positions.

5.8 Tricks to obtain speedups

In order to speedup the Unicom model several trick can be employed to remove redundant calculations.

Circular bitmaps
Bitmaps obtained from measurements consist of square grids which are slightly wider and taller than the pupils which are circular and limited to a radius of 1 in σ-space. Therefore, by only performing calculations for pixels within the unit circle in σ-space, redundant calculations can be removed. The indices of pixels within this unit circle can be found by checking which grid points (pixels) in the bitmap satisfy the following inequality:

$$\sqrt{(\sigma_i^x)^2 + (\sigma_j^y)^2} \leq 1. \tag{5.22}$$

Fingertips
When calculating which of the slit's grid points fall within the shadows of the Unicom fingers on RL, full descriptions of the polygons of the fingers are often redundant. Assuming Unicom fingers consist of a shaped tip followed by a part of constant width and that only these two parts of the finger can be inserted into the slit, simply treating only the vertices of the tips of the fingers suffices. The tip of the finger is the primary decision boundary that divides the slit into a part that is shaded by the finger and a part where all light passes as illustrated in Figure 5.5. Two secondary decision boundaries are also required to determine if grid points are located in a finger's shadow in the x-direction. Since the second inserted part of the finger has constant width, the secondary decision boundaries simply consist of vertical lines through the edge vertices of the fingertip so no additional vertices are needed to create them. Instead of first creating shaded polygons for each finger and finger profile and then creating a shaded area for each FFI as was done in Equation 5.14 and Equation 5.15 respectively, now first a check for the primary and then for the secondary decision boundaries can be performed to determine if grid points are contained in the shaded area. To begin the decision boundary setup, the primary decision boundary for a finger profile k is obtained by linear interpolation of all vertices at RL of the separate fingertips:

$$\Omega_{i,j,k}^{\mathbf{d}}(x) = \Gamma_{\text{lin}}(\widetilde{\mathbb{X}}_{i,j,k}^r(\mathbf{d})), \tag{5.23}$$

where $\Omega_{i,j,k}^{\mathbf{d}}(x)$ is the function describing the primary decision boundary for $\text{FFI}_{i,j}$ of the k-th Unicom profile at RL which depends on the amount of insertion for each finger, $\Gamma_{\text{lin}}(\cdot)$ indicates linear interpolation is performed over a matrix containing (x, y) coordinate pairs in each column which are ordered to monotonically increase in x and $\widetilde{\mathbb{X}}_{i,j,k}^r(\mathbf{d})$ is similar to $\mathbb{X}_{i,j,k}^r(\mathbf{d})$ but only contains vertices that are part of the fingertips. The secondary decision boundaries are obtained as:

$$\begin{aligned} x_{i,j,k,p}^L &= \widetilde{\mathbb{X}}_{i,j,k,1,q}^r(\mathbf{d}) \quad \text{for } q = (p-1)\cdot b(k) + 1 \\ x_{i,j,k,p}^R &= \widetilde{\mathbb{X}}_{i,j,k,1,q}^r(\mathbf{d}) \quad \text{for } q = p \cdot b(k) \end{aligned}, \tag{5.24}$$

with $x_{i,j,k,p}^L$ and $x_{i,j,k,p}^R$ the left and right secondary decision boundary for finger p in Unicom profile k for $\text{FFI}_{i,j}$ respectively and $b(k)$ the number of vertices in the tip of a Unicom finger for Unicom profile k. Checking if (x, y) at RL is contained between the two secondary decision boundaries of a finger can be done by only considering the x-coordinate because the grid points in x at RL are independent of y. Hence, the set of x coordinates within the width of the shadow of at least one Unicom finger can be constructed:

$$B_{i,j,k} = \bigcup_{p=1}^{N(k)} \left\{ x_v \,\middle|\, x_{i,j,k,p}^L \leq x_v \leq x_{i,j,k,p}^R \text{ for } v = 1, 2, \ldots, N_v \right\} \tag{5.25}$$

For grid points like the one shown in Figure 5.5 the output of the Unicom model can now be determined by pixel intensity attenuation as:

$$\mathbb{I}^{\mathbf{d}}_{i,j,v,w} = \begin{cases} 0 & \text{if} \quad \Omega^{\mathbf{d}}_{i,j,k}(x_v) \geq y_w \ \wedge \ x_v \in B_{i,j,k} \\ \mathbb{I}^{\mathbf{0}}_{i,j,v,w} & \text{Otherwise} \end{cases}, \tag{5.26}$$

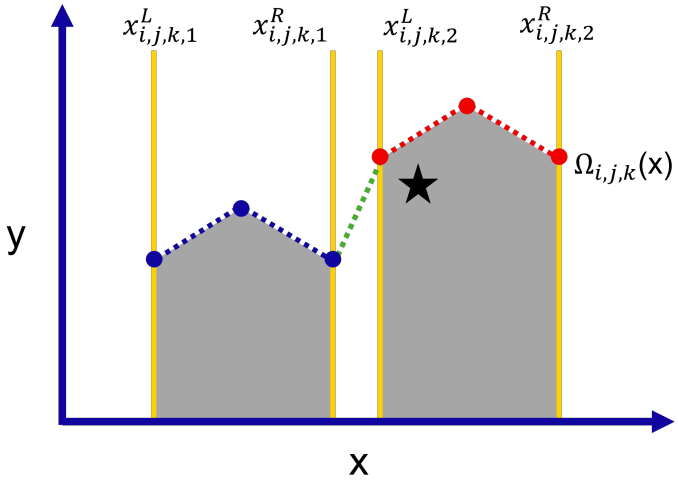

Fig. 5.5: Illustration of the primary (dotted line) and secondary (yellow vertical lines) decision boundaries for two Unicom fingers. The grey area is shaded by the fingers and thus the light at the grid point (star) is blocked.

Intensity thresholding
A Unicom model should predict the impact of the Unicom fingers on the pupil, but the impact on pupil spots is far more interesting than the impact on the areas between these spots. Therefore, an argument can be made to only perform calculations for the pixels which in at least one of the static measured pupils surpass a certain intensity threshold. This way, calculations are only performed for FFIs belonging to pixels in an area which is illuminated by a pupil spot and calculations for FFIs corresponding to pixels with only stray light and measurement noise are omitted. In the end a decision can be made either keep the input intensity or force the intensity to zero for the pixels with omitted calculations. Note that this method can be used to gain quite a significant speedup because pupil fill is sparse, but this does come with a trade off: all stray light is either included or blocked in the final pupils. This means that the total energy in the bitmap pupil that needs to be distributed over all spots in by the parcellation algorithm changes and where the intensity is added or removed will depend on (σ^x, σ^y). Hence, this method might have adverse effects on the parcellated pupils that can be obtained by supplying the bitmap pupil output of the static Unicom model to the parcellation algorithm.

Symmetry exploitation
The σ-coordinates in the bitmap pupil as well as the x-coordinates of the grid of the slit at RL are symmetrical around 0. Since the functions sin, arcsin, tan and arctan are odd functions and cos is an even function these symmetries in grid points can be exploited to perform calculations for half grids instead of the complete grid and subsequently copy them for the other half of the grid (after multiplication with -1 for odd functions). Using this trick fewer trigonometric calculations would have to be performed without trade off in accuracy.

Linearization of trigonometric functions
Apart from exploiting symmetry of trigonometric functions, some of the trigonometric functions might also be linearizable by using approximations like $\sin(\theta) = \theta$. However, care should be taken to check that this does not introduce large errors in angles but also distances calculated in the model. For

instance $\arcsin(x) = x$ in Equation 5.6 might on its own be a decently accurate approximation. When considering that in Equation 5.4 CRAO is added to the approximated angle and a distance is calculated by multiplying the tangent of this sum by Δz, it becomes clear that small errors in angles can lead to larger errors in calculated distances.

5.9 Algorithm pipelines

Here the algorithm pipeline of both the static Unicom model as well as its adoption in a scheme to correct scanning pupils will be presented. To this end, the processing steps and blocks previously described will be put together. Not all steps ended up being used in the final Unicom model because some steps were found to have adverse or no significant effects on the model's performance.

The static Unicom model

The algorithm pipeline of the static Unicom model that is the first result of this thesis, $\mathcal{M}$, is depicted in Figure 5.6. Here all previously presented processing blocks are used in the order in which they were mentioned. Note that in the data pre-processing block two zero forcing steps are present, one before and one after the slit interpolation. The first zero forcing step is to make sure that the interpolation is not based on non-physical negative intensities in the measurements, the second to filter out any negative intensities the interpolation method might have produced.

Multiple processing steps and speedup tricks were not elected for placement in $\mathcal{M}$. For most of these excluded steps this decision was based on investigations with previous iterations of the static Unicom model, during which the processing steps did not lead to better predictions by the model. Data filtering was excluded because including measurement points at the edges of the slit allows for predictions for the entire slit size without introducing the need for extrapolation. Advanced projection was chosen over simple projection because it is believed to more closely resemble the machine's design and produced better predictions. The speedup using intensity thresholding was excluded because in previous iterations using this method lead to lower accuracy when comparing predicted static pupils to measured static pupils after integrating and subsequently parcellating. This lower accuracy may be due to the spatially dependent change in the amount of energy contained in the space of the pupil between spots. Symmetry was not yet implemented due to time constraints combined with the fact that optimizing the speed of the model falls outside of the scope of this thesis.

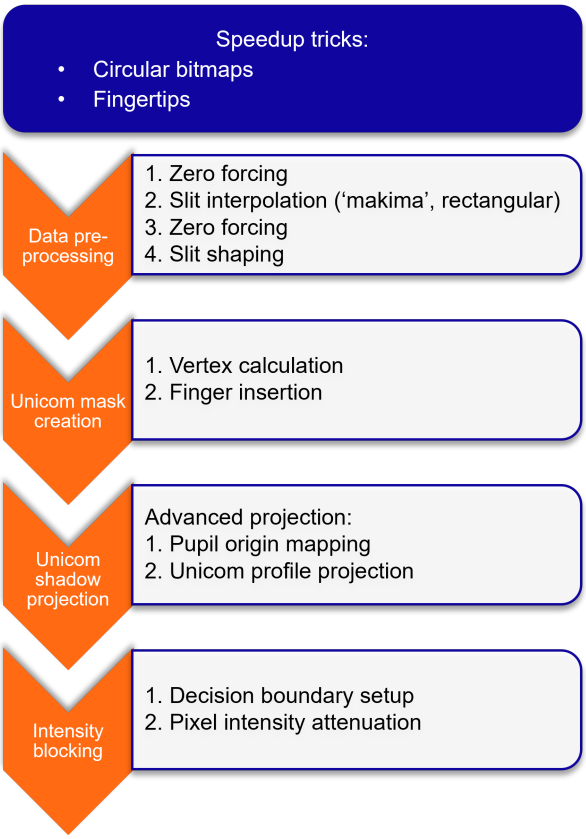

Fig. 5.6: Algorithm pipeline of the static Unicom model containing its processing blocks with their processing steps in order of execution. Speedup tricks used by the model are shown in the blue box on top.

Input of $\mathcal{M}$ consists of:

- A static bitmap pupil measurement $\mathbb{I}^{\mathbf{0}}$.
- A vector $\mathbf{u}$ with the measurement locations in the x-direction in the slit without its curvature.
- A vector $\mathbf{w}$ with the measurement locations in the y-direction in the slit without its curvature.
- A vector $\mathbf{d}$ with the Unicom finger positions.
- A machine data parameter with the machine-type, magnification $1/M_x$ and $1/M_y$ from RL to WL and the NA.
- A parameter to choose the interpolation method ('makima' for $\mathcal{M}$).
- A parameter, ω, to specify the number of times grid steps are halved during interpolation.
- CRAO (optional, assumed from machine type if not supplied).
- Parameter to switch interpolation off (optional, by default interpolation is performed).
- A parameter to supply results of a previous round of interpolation including the interpolation grid (optional).

Output of $\mathcal{M}$ consists of:

- A matrix of x-values of the grid points in the slit after interpolation and slit shaping.
- A matrix of y-values of the grid points in the slit after interpolation and slit shaping.
- The predicted Static bitmap pupils $\mathbb{I}^{\mathbf{d}}$.
- The intensities resulting from interpolation.

$\mathcal{M}$ in scanning predictions

The second result of this thesis is a scheme with which the effect of the Unicom on scanning pupils can be predicted. This scheme, depicted in Figure 5.7, utilizes $\mathcal{M}$ to obtain correction maps for parcellated pupils by comparing $\mathcal{M}$'s input and output after both have been integrated, parcellated and then normalized to a total intensity of one for each pupil. By subsequently dividing the model prediction, ${}_{\mathcal{M}}\mathbb{j}^{\perp\mathbf{d}}$ by the model input, $\mathbb{j}^{\perp\mathbf{0}}$, correction maps for parcellated integrated pupils are obtained. Here the superscript $^{\perp}$ is added to indicate that pupils have been normalized to contain a total intensity of one, which is necessary when comparing two different sets of pupils since their total intensity might be different. The preceding ${}_{\mathcal{M}}$ subscript is used to show that pupils result from using $\mathcal{M}$ directly. In the case of parcellated pupils, these correction maps are the vectors $\boldsymbol{\alpha}_v$ with n entries describing the correction for the corresponding pupil spot in the pupil at the v-th x-location in the slit. By multiplying these correction maps with normalized scanning pupil measurements with fingers fully extracted, the normalized parcellated scanning pupils, $\mathbb{j}^{\perp\mathbf{d}}$, for the finger insertions $\mathbf{d}$ that were supplied to $\mathcal{M}$ can be obtained.

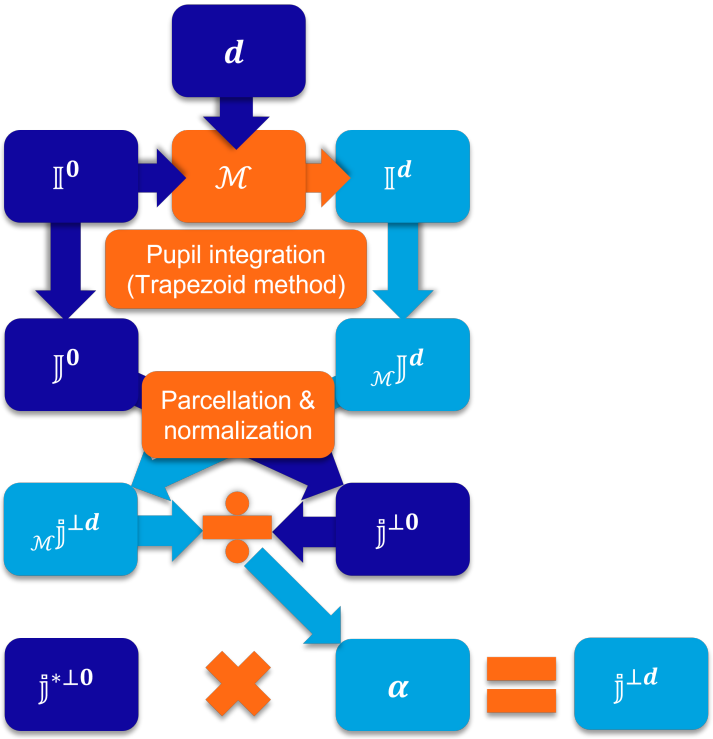

Fig. 5.7: Scanning Unicom prediction scheme to obtain normalized Unicom corrected scanning pupils, $\mathbb{j}^{\perp\mathbf{d}}$, from normalized scanning measurements with fully extracted fingers, $\mathbb{j}^{*\perp\mathbf{0}}$. Depicted are model steps (orange), $\mathcal{M}$ independent data (dark blue) and $\mathcal{M}$ dependent data (light blue). An overview of notation can be found in Chapter 1.

Here the trapezoid method was used to perform the integration step, because during investigations, the OLS optimization methods were found to have insufficient positive effect on the agreement between $\mathbb{j}^{\perp\mathbf{0}}$ and $\mathbb{j}^{*\perp\mathbf{0}}$ to utilize the OLS method which would come with the risk of over fitting to the data that was used. The * superscript indicates that scanning pupils are measured in stead of obtained after integration.

Note that ${}_{\mathcal{M}}\mathbb{j}^{\perp\mathbf{d}}$ and $\mathbb{j}^{\perp\mathbf{d}}$ are predictions that try to describe the same type of pupils, namely normalized parcellated scanning pupils. Hence a case could be made to try and use the former instead of the latter to perform scanning pupil predictions, but this was found to introduce larger prediction errors. These larger errors are the result of the difference that in the former prediction, only static measurements are used, whilst the latter also utilizes scanning measurements. Since static and scanning measurements are different, comparing predictions solely based on static measurements to scanning measurements is sure to introduce errors due to the difference in measurement type. To make an attempt to mitigate

these errors, the influence of scanning measurements can be increased whilst decreasing the influence of static measurements by only creating the correction map based on static measurements and letting the uncorrected input depend on scanning measurements. Furthermore, this creates the opportunity to input newer scanning measurements when they become available to update the prediction.

An attempt was made to create a direct transformation from static bitmap measurements, $\mathbb{I}^{\mathbf{0}}$, to scanning bitmap measurements, $\mathbb{J}^{*\perp\mathbf{0}}$, by use of OLS optimized integration. This method was unsuccessful both with and without the two types of thresholding and both with quadratic features and without them. The observed differences between the prediction after integrating, $\mathbb{J}^{\perp\mathbf{0}}$, and the measurement, $\mathbb{J}^{*\perp\mathbf{0}}$, consisted of the pupil spots in the former having increased width but decreased peak intensity when compared to the latter. The size of both scanning and static pupil spots is limited by the size of the pinhole at the (x, y)-position in the slit at RL at which the measurement is conducted. As the size of this pinhole is constant for both types of measurements an explanation is needed for the observed difference in integrated spot size. One explanation is that the differences might be due to the effects of random noise on the locations of spots in the pupil. This noise may be induced by slight variations in the plasma's position in the source and drifts in positions of mechanical components in the machine. Next, how such random noise might affect the size of pupil spots is explained.

Let Y be probability distribution for random noise vectors $\boldsymbol{\eta}$ that describe the displacement of the (σ^x, σ^y) coordinates from their mean. Then, if random noise causes the observed discrepancies between static and scanning pupil spots, effects may be visible due to the much longer duration of the static measurement routine compared to the scanning measurement routine. For the shorter scanning routine roughly one realization, $\boldsymbol{\eta}_0$, of the effect of the noise might be observed, whilst in the static measurements multiple realizations, for instance $\boldsymbol{\eta}_1$, $\boldsymbol{\eta}_2$ and $\boldsymbol{\eta}_3$, are observed over time. If the displacements of spots due to noise, $\boldsymbol{\eta}_i$, are centered around a constant mean location for the pupil spot, this might lead to the observed increased width and decreased peak intensity of the spots. For different realizations of $\boldsymbol{\eta}$, the observed spot is still likely to always illuminate the point with zero displacement noise as illustrated in Figure 5.8. When added, the observed spots in Figure 5.8 have a lower peak value after normalization compared to their individual peak values due to the increased width of the collectively illuminated area.

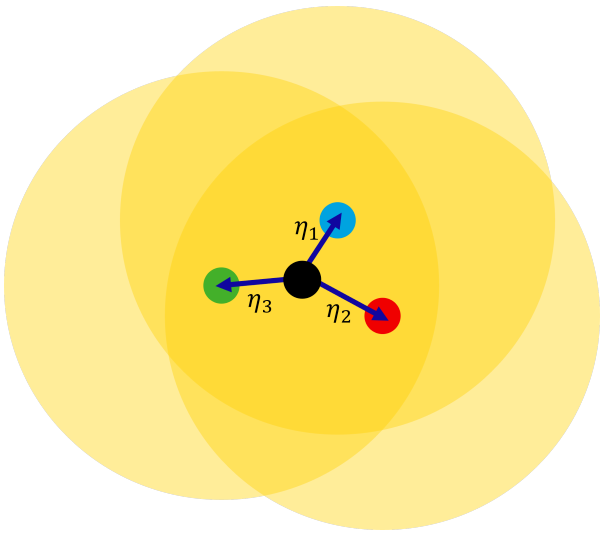

Fig. 5.8: Illustration of three realizations of the random displacement of equally sized pupil spots (yellow) from the noiseless position of the spot (black). Centers of pupil spots are given by the dots (blue, green, red) and realizations of the noise $\eta_{n\eta}$ by the vectors.

The choice to first parcellate model output and then obtain correction maps to apply to parcellated pupils instead of calculating correction maps for bitmaps is a deliberate one. Correction maps for bitmaps could be applied to the scanning bitmap measurements and the resulting prediction could be parcellated afterwards. However, when using bitmaps the effects of slightly different positions of pupil spots in the measurements used to calculate the correction map and the scanning measurement to which the correction map is applied has greater impact. This is the result of the higher spatial resolution in bitmaps. When parcellation is performed first, misalignment of the spots in the two measurements

becomes less influential because the intensities of multiple pixels are grouped into one spot. Parcellated pupil correction maps were observed to outperform their bitmap based counterparts.

5.10 Verification methods and parameter optimization

To verify the performance of the static Unicom model and the scanning pupil prediction scheme, two methods to quantify model errors are used. Although they are called model errors, some emphasis needs to be put on the fact that a part of the errors is due to the comparison of pupil measurements and predictions which are being derived from different measurements. When comparing two different measurements some error would always be present, even if the placement of the Unicom fingers was identical for both measurements. Sources contributing to this error are for instance measurement uncertainty but also drifts in source location or of the orientation of mirrors. Therefore, the errors quantified here are not solely the effects of modeling errors in predicting the Unicom effects accurately.

Intensity error

The first verification method consists of calculating the L_2 error when comparing predictions by the model or scheme to their measured counterpart. For the static bitmap pupil predictions by $\mathcal{M}$ this takes the following form:

$$\mathcal{S}({}_{\mathcal{M}}\mathbb{J}^{\perp\mathbf{d}}, \mathbb{J}^{\perp\mathbf{d}}) = ||{}_{\mathcal{M}}\mathbb{J}^{\perp\mathbf{d}} - \mathbb{J}^{\perp\mathbf{d}}||_{\mathrm{F}}^2, \tag{5.27}$$

where $\mathcal{S}(\cdot,\cdot)$ is the L_2 error, which is to be calculated as a matrix norm over all entries (see Appendix A), and normalized bitmaps are used to ensure errors are due to the distribution of intensity in the pupil and not to differences in total intensity. For the results $\mathbb{j}^{\perp\mathbf{d}}$ of the scanning pupil prediction scheme the comparison would be with the measurement $\mathbb{j}^{*\perp\mathbf{d}}$. Both errors can then be compared to their counterparts without using predictions based on the Unicom, $\mathcal{S}(\mathbb{J}^{\mathbf{0}}, \mathbb{J}^{\mathbf{d}})$ and $\mathcal{S}(\mathbb{j}^{*\perp\mathbf{0}}, \mathbb{j}^{*\perp\mathbf{d}})$ respectively, to quantify the effects of utilizing the static Unicom model or the scanning pupil prediction scheme on the corresponding errors of predictions. Additionally, to investigate the maximum absolute deviation of predictions from measurements $\mathcal{S}^{\infty}$ can be used:

$$\mathcal{S}^{\infty}({}_{\mathcal{M}}\mathbb{J}^{\perp\mathbf{d}}, \mathbb{J}^{\perp\mathbf{d}}) = ||{}_{\mathcal{M}}\mathbb{J}^{\perp\mathbf{d}} - \mathbb{J}^{\perp\mathbf{d}}||_{\max}^2, \tag{5.28}$$

with $||\cdot||_{\max}$ the L_∞ norm (see Appendix A).

Parameter optimization

Based on $\mathcal{S}$ a scalar parameter c, that adds an equal displacement in the y-direction to the design position of all fingers, was optimized. Optimization was performed to a single measurement $\mathbb{I}^{\perp\mathbf{d}}$ with the corresponding $\mathbf{d}$ supplied to the model. The method of optimization was grid search since for a scalar parameter this only involves points on a single line. Furthermore, $\mathcal{S}$ can be expected to increase rapidly for values of c that either extract the fingers too much or insert them too much as this would change the distribution of intensity in pupils at every FP. Once found, the value of c is simply added to all entries of the vector $\mathbf{d}$ that is supplied to $\mathcal{M}$:

$$\tilde{\mathbf{d}} = \mathbf{d} + c \cdot \mathbf{e}_{N_v}, \tag{5.29}$$

where $\tilde{\mathbf{d}}$ is the vector of Unicom finger positions that is used by the model in all calculations.

Changes in c can be thought of as moving the entire Unicom towards or away from the illumination beam. For large values of c the 'extracted' position of the fingers will be moved further into the slit, for small values of c the 'extracted' position will be place further away from the slit. Variations in the location of all the Unicom fingers in the y-direction might be the result of the manufacturing process of an EUV machine's components, their assembly or of calibrations of the zero position of Unicom fingers.

PQF deltas

The second method of error quantification consists of the calculation of δ^{PQF} defined as:

$$\boldsymbol{\delta}_v^{\mathrm{PQF}}({}_{\mathcal{M}}\mathbb{j}^{\perp\mathbf{d}}, \mathbb{j}^{\perp\mathbf{d}}) = \mathbf{PQF}_v({}_{\mathcal{M}}\mathbb{j}^{\perp\mathbf{d}}) - \mathbf{PQF}_v(\mathbb{j}^{\perp\mathbf{d}}), \tag{5.30}$$

where $\boldsymbol{\delta}_v^{\mathrm{PQF}}(\cdot,\cdot)$ is the $7 \times m$ matrix containing the 7 PQF deltas for m different pitches at grid point v in the x-direction and $\mathbf{PQF}_v(\cdot)$ is the $7 \times m$ matrix containing the PQF values. Important to note

is that PQF values 1 through 4 are calculated in a way that already condenses information of different FPs to a single PQF value for each pitch. Therefore in the remainder of this report, values of PQF 1 through 4 at each FP will be considered to be identical to the condensed values over all FPs. In this way, the same calculations can be applied to each PQF value without altering results.

To arrive at a single error value for each PQF parameter the maximum over pitch and FP can be taken:

$$\boldsymbol{\varepsilon}({}_{\mathcal{M}}\mathbb{j}^{\perp\mathbf{d}}, \mathbb{j}^{\perp\mathbf{d}}) = \max_{v} \max_{\text{pitch}} |\boldsymbol{\delta}_{v}^{\text{PQF}}({}_{\mathcal{M}}\mathbb{j}^{\perp\mathbf{d}}, \mathbb{j}^{\perp\mathbf{d}})|, \tag{5.31}$$

with $\boldsymbol{\varepsilon}(\cdot,\cdot)$ the vector with its 7 entries the maximum absolute PQF error over FPs and pitch and the absolute value is taken element wise. For the predictions by the scanning pupil prediction scheme, the errors are calculated as $\boldsymbol{\varepsilon}(\mathbb{j}^{\perp\mathbf{d}}, \mathbb{j}^{*\perp\mathbf{d}})$. To investigate the effect of applying the Unicom model or prediction scheme, the calculated errors are compared to $\boldsymbol{\varepsilon}(\mathbb{j}^{\perp\mathbf{0}}, \mathbb{j}^{\perp\mathbf{d}})$ and $\boldsymbol{\varepsilon}(\mathbb{j}^{*\perp\mathbf{0}}, \mathbb{j}^{*\perp\mathbf{d}})$ respectively.

6 Model results

In this chapter the results from investigations into the performance of the static Unicom model and the scanning pupil prediction scheme are presented. First the results of optimization of the model's parameter are presented. Second, the performance of the static Unicom model is elaborated upon. Third, the same performance indicators are examined for the scanning pupil prediction scheme. This chapter is concluded with a table giving a condensed overview of the performance of the static Unicom model and the scanning pupil prediction scheme in combination with a discussion of the presented results.

6.1 Parameter optimization

In order to optimize the free parameter of the model, c, grid search was performed using a single pair of static bitmap measurements. One of the two measurements, $\mathbb{I}^{\mathbf{0}}$, with Unicom fingers extracted was used as input for $\mathcal{M}$. The other measurement, $\mathbb{I}^{\mathbf{d}_1}$, was used for verification and contained measurements with the Unicom fingers inserted by the amounts specified by $\mathbf{d}_1$. Subsequently, the accuracy of the model supplied with finger movements $\mathbf{d}_1$ and $\omega = 3$ (the grid refinement parameter for interpolation) was quantified using the cost function S defined in Equation 5.27. $\omega = 3$ was chosen because, as will be presented at the end of this section, execution times of the model begin to rise more quickly for $\omega = 4$ and investigations of PQF with $\omega = 4$ did not lead to improved model performance. The evaluation of S was performed with 100 steps for $c \in [-5, 2]$ after which the domain where S was minimized was investigated for a second time with 50 steps and $c \in [-2, -1.7]$ to find a minimum at $c = -1.84$. The curves of S as a function of c resulting from this process are shown in Figure 6.1.

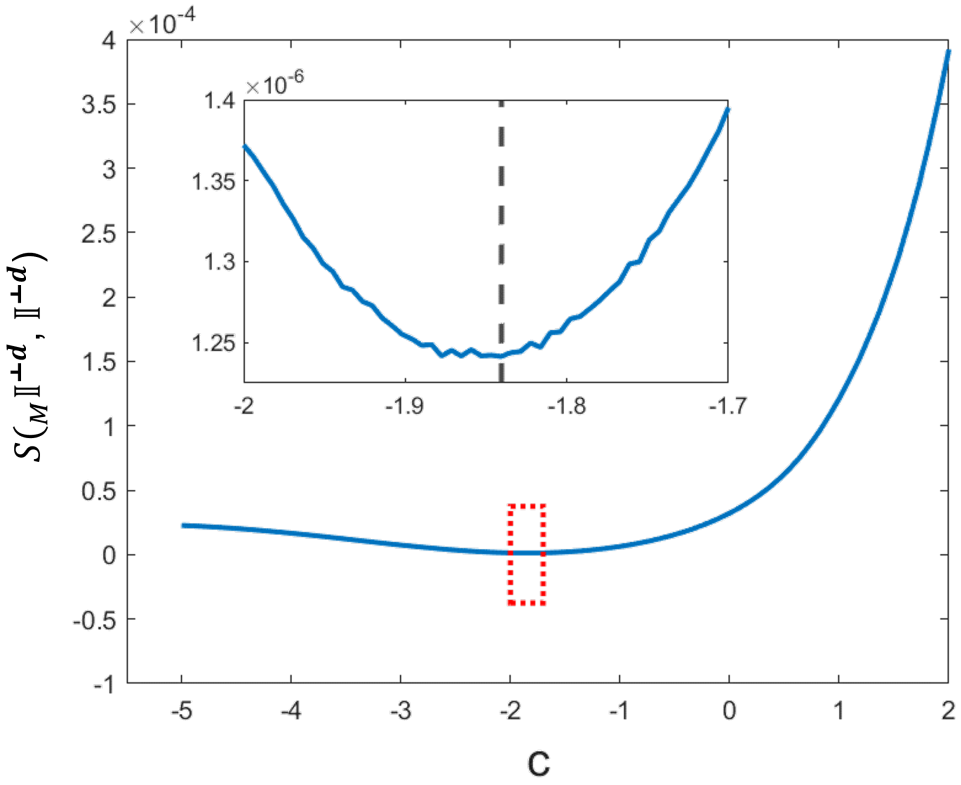

Fig. 6.1: Graph of the cost function $S({}_{\mathcal{M}}\mathbb{I}^{\perp\mathbf{d}}, \mathbb{I}^{\perp\mathbf{d}})$ as a function of model parameter c. The insert shows S on a finer grid in the neighborhood (red dotted box) of its minimizing c-value (black dashed line).

On the coarse grid, the cost function $\mathcal{S}$ is quite smooth and starts at a higher value, which first decreases as c is increased and then quickly ramps up. This behavior is expected because for small values the

model simulates the fingers as not inserted and for high values almost all light gets blocked. Hence, when comparing the intensity predicted by the model to the measurement, the cost function should increase to both sides of the optimum for c. The fact that at large values of c the cost function blows up is due to the normalization of the total intensity of each bitmap pupil to 1. As c becomes too large (fingers are inserted further), not only do the errors in intensity increase due to the excessive blockage of light, but these errors also get more weight attached to them because the total intensity of the not yet normalized bitmap decreases.

On the refined grid, the cost function appears to be not completely smooth. The value of $\mathcal{S}$ with $-1.9 \leq c \leq -1.8$ shows some jumps, though these jumps comprise less than 1% of the value of $\mathcal{S}$. Had observed jumps in $\mathcal{S}$ been larger then it might have been advisable to first fit the curve of $\mathcal{S}$ with for instance a polynomial to be less dependent on the sudden jumps during optimization of c. These jumps can be explained by the fact that moving all Unicom fingers by the same amount will lead to quantized changes in blocked intensity. Intensity can only be blocked per pixel in the bitmap pupils, hence $\mathcal{S}$ will not be completely smooth. Although it seems that with a slight perturbation of $\mathcal{S}$ with $-1.9 \leq c \leq -1.8$, the optimum c could be found anywhere within this interval, changes of 0.1 for c are small compared to the entire movement range of the Unicom fingers.

Furthermore, c only captures a single fixed displacement of all Unicom fingers, which means that changes in $\mathcal{S}$ due to displacements of individual fingers or due to slight offsets in the propagation angles of the EUV light can only be compensated for to a coarse degree. Around the optimal c-value, changes in c can be expected to give a trade-off between some modelled fingers blocking more and some fingers blocking less light than they do in reality. In this sense the Unicom model is not extremely sensitive to the exact value of c that is used, as long as c is located near the optimum value that minimizes $\mathcal{S}$. Additional parameters could be added to the Unicom model to capture other effects that might influence $\mathcal{S}$ such as the individual displacements of Unicom fingers. However, when additional parameters are used to tune the model, care should be taken to prevent overfitting these parameters to the data used during optimization because this would worsen the model's accuracy when predicting for different pupils and Unicom settings.

A possible explanation of why adding the amount c to all entries of $\mathbf{d}$ in the model results in better performance is that the relative y-position, with respect to the slit, of the Unicom fingers in the setup of the model was different from the position in the actual machine. This difference may be the result of a combination of factors such as: specifications of design positions in slightly misaligned coordinate systems and deviations of the Unicom from the design due to the manufacturing or assembly process. Another contributor to a non-zero optimum c could be a deviation in the other fixed parameters in the model, such as CRAO, which would move the light closer towards the Unicom.

6.2 Performance of the static Unicom model

With c fixed to -1.84 and $\omega = 3$, the performance of the static Unicom model was calculated by using the metric S for its intensity and ε for its PQF. For completeness, here the time required for running the model for a few use cases will also be presented. Results presented here are for the specific positions of the Unicom fingers, $\mathbf{d}_1$, which correspond to a stairs shaped insertion pattern. This pattern of Unicom fingers was chosen because it corresponds to the setup used to obtain the only suitable static measurement available. Thus, the finger on the left edge of the slit is fully inserted and the finger on the right edge is fully extracted with a constant decrease of insertion for the fingers between them, as illustrated in Figure 6.2.

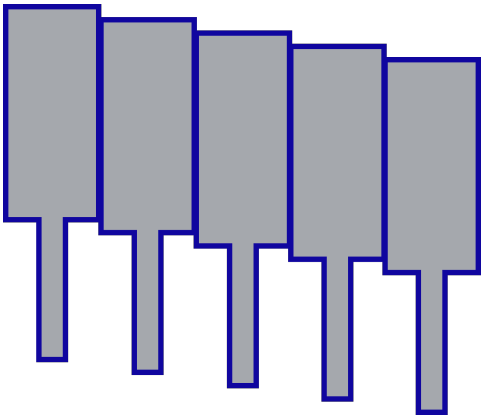

Fig. 6.2: Illustration of the pattern of Unicom finger insertion specified by $\mathbf{d}_1$ for a few fingers, ignoring slit curvature.

Intensity

By including $\mathcal{M}$ when using static integrated pupils without Unicom finger insertions, $\mathbb{J}^{\mathbf{0}}$, to predict static integrated pupils with Unicom pattern $\mathbf{d}_1$, $\mathbb{J}^{\mathbf{d}_1}$, an error reduction of 73.9% was realized for $\sqrt{\mathcal{S}}$ with normalized pupils. Here the square root of $\mathcal{S}$ is taken to obtain metrics for the error in the same units of intensity as obtained through the measurements. Additionally, the maximum absolute deviation within normalized pupil predictions, $\sqrt{\mathcal{S}^\infty}$, and the maximum absolute deviation within non-normalized pupils dropped by 76.7% and 90.3% respectively, as shown in Table 3. This implies that, using $\mathcal{M}$, both the actual intensity, as well as the distribution of intensity throughout a pupil which is impacted by the Unicom, can be predicted with far higher accuracy than was previously possible without a Unicom model.

	$\sqrt{\mathcal{S}\left(\mathbb{J}^{\perp\mathbf{0}}, \mathbb{J}^{\perp\mathbf{d}}\right)}$	$\sqrt{\mathcal{S}\left({}_{\mathcal{M}}\mathbb{J}^{\perp\mathbf{d}}, \mathbb{J}^{\perp\mathbf{d}}\right)}$	Error reduction [%]
$\mathbf{d}_1$	$4.73 \cdot 10^{-3}$	$1.23 \cdot 10^{-3}$	73.9
	$\sqrt{\mathcal{S}^\infty\left(\mathbb{J}^{\perp\mathbf{0}}, \mathbb{J}^{\perp\mathbf{d}}\right)}$	$\sqrt{\mathcal{S}^\infty\left({}_{\mathcal{M}}\mathbb{J}^{\perp\mathbf{d}}, \mathbb{J}^{\perp\mathbf{d}}\right)}$	Error reduction [%]
$\mathbf{d}_1$	$3.15 \cdot 10^{-4}$	$7.34 \cdot 10^{-5}$	76.7
	$\sqrt{\mathcal{S}^\infty\left(\mathbb{J}^{\mathbf{0}}, \mathbb{J}^{\mathbf{d}}\right)}$	$\sqrt{\mathcal{S}^\infty\left({}_{\mathcal{M}}\mathbb{J}^{\mathbf{d}}, \mathbb{J}^{\mathbf{d}}\right)}$	Error reduction [%]
$\mathbf{d}_1$	$1.56 \cdot 10^{3}$	152	90.3

Table 3: Square root values of the $\mathcal{S}$ and $\mathcal{S}^\infty$ errors for predictions without and with use of $\mathcal{M}$ and the reduction of errors by using $\mathcal{M}$. Predictions and measurements were performed for $\mathbf{d} = \mathbf{d}_1$.

It is necessary to keep in mind that these results for static pupils were obtained under the most favorable circumstances for the model: both the input measurement and verification measurement were of the static type and measured closely after each other on the same machine. Furthermore, the model parameter c was optimized to obtain a minimal value for $\mathcal{S}$ when using $\mathbb{I}^{\perp\mathbf{d}_1}$ as verification measurement, from which $\mathbb{J}^{\perp\mathbf{d}_1}$ is derived. Therefore, the model is to some extent specifically tailored to obtain a large reduction in $\sqrt{\mathcal{S}}$ for this particular instance. However, the majority of the model's components were setup only using design information about the Unicom and the light path within the machine. Hence, even though part of the model is fitted to these verification measurements, the model will likely generalize well to predicting different static measurements on the same machine when still using $c = -1.84$. Whether or not trying to predict different static measurements on the same machine actually has significant impact on model performance can only be tested if more static measurements are performed on the same machine.

Nevertheless, the $\sqrt{\mathcal{S}^\infty}$ error reductions shown in Table 3, to which c was not optimized, hint that the model performs well in multiple different ways. Moreover, use of $\mathcal{M}$ in SPPS to predict parcellated scanning pupils with multiple different finger positions also gave significantly more accurate predictions

as will explained in Section 6.3. Additionally, applying $\mathcal{M}$ lead to high gains in accuracy of PQF values of static pupil predictions.

PQF

The use of $\mathcal{M}$ consistently lead to significant ϵ-error reductions for the static pupil measurements with finger insertions $\mathbf{d}_1$. Error reduction percentages varied between 47.3% to 86.4% as shown in the top left block of Table 7. The left most column of errors is calculated between the PQF of the measured static pupil with extracted Unicom fingers and the PQF of the measured static pupil with insertion corresponding to $\mathbf{d}_1$, thus $\boldsymbol{\varepsilon}^{\mathbf{0}}(\mathbf{d}_1) = \boldsymbol{\varepsilon}(\mathbb{J}^{\perp\mathbf{0}}, \mathbb{J}^{\perp\mathbf{d}_1})$. The middle column contains the same kind of errors but calculated between the static pupil prediction by the model for $\mathbf{d}_1$ and the static pupil measured with $\mathbf{d}_1$, $\boldsymbol{\varepsilon}^{\mathcal{M}}(\mathbf{d}_1) = \boldsymbol{\varepsilon}({}_{\mathcal{M}}\mathbb{J}^{\perp\mathbf{d}_1}, \mathbb{J}^{\perp\mathbf{d}_1})$. From the first and the second column the error reduction is calculated as $(\boldsymbol{\varepsilon}^{\mathbf{0}} - \boldsymbol{\varepsilon}^{\mathcal{M}})/\boldsymbol{\varepsilon}^{\mathbf{0}} \cdot 100\%$ where computations are performed element-wise.

Although the ε-errors offer a concise view of how accurate a prediction method is, the actual δ^{PQF}-values give a more complete description of prediction accuracy over a range of pitches. In Figure 6.3 the second values of $\boldsymbol{\delta}^{\mathrm{PQF}}({}_{\mathcal{M}}\mathbb{j}^{\perp\mathbf{d}_1}, \mathbb{j}^{\perp\mathbf{d}_1})$ as well as of $\boldsymbol{\delta}^{\mathrm{PQF}}(\mathbb{j}^{\perp\mathbf{0}}, \mathbb{j}^{\perp\mathbf{d}_1})$ are depicted for a range of pitches. As can be seen, the ε shrinks when using $\mathcal{M}$ and δ^{PQF} becomes more smooth over then entire range of pitches, although this does not necessarily mean that the delta is smaller for every pitch.

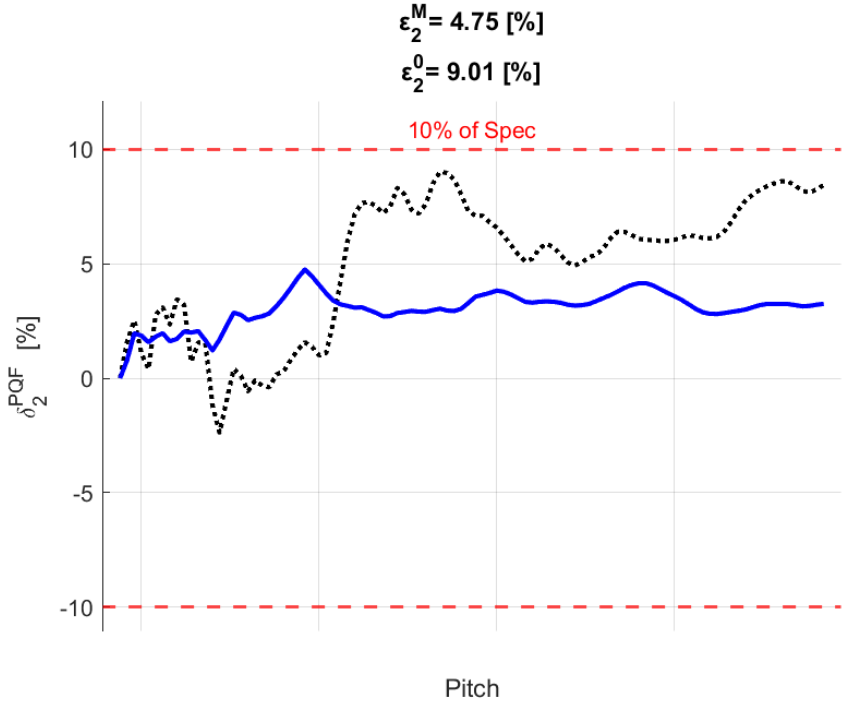

Fig. 6.3: Plot of $\boldsymbol{\delta}_2^{\mathrm{PQF}}({}_{\mathcal{M}}\mathbb{j}^{\perp\mathbf{d}_1}, \mathbb{j}^{\perp\mathbf{d}_1})$ (blue) over a range of pitches. $\boldsymbol{\delta}_2^{\mathrm{PQF}}$ without using $\mathcal{M}$ at each pitch is depicted in black (dotted). $\boldsymbol{\delta}$-s are given as a percentage of the machine's spec with the 10% deviation from zero shown as red dashed lines.

However, for the second δ^{PQF} the model reduces the errors the least. An example of one of the δ^{PQF}-values, the sixth, that decreases more significantly is shown in Figure 6.4. For each of the FPs used in calculations $\delta^{\mathrm{PQF}}({}_{\mathcal{M}}\mathbb{j}^{\perp\mathbf{d}_1}, \mathbb{j}^{\perp\mathbf{d}_1})$ is shown. For $\delta^{\mathrm{PQF}}(\mathbb{j}^{\perp\mathbf{0}}, \mathbb{j}^{\perp\mathbf{d}_1})$ the area between the maximum and minimum values over all FPs is shaded in gray. Clearly, the maximum absolute deviation from 0%, no error, when considering all FPs becomes smaller when using $\mathcal{M}$ regardless of the pitch considered. Again, the delta curves become quite smooth, though some patterns in the errors still seem to remain. These remaining patterns might be due to the effect of the Unicom but could also exist due to the effects other parts of the machine have on the two measurements involved in the comparison.

In general, for all 7 PQF-values using $\mathcal{M}$ resulted in smoother δ^{PQF}-s, which for most pitches were smaller than their counterparts when directly using measurements with the Unicom fingers extracted as a prediction. In particular, all the worst errors became significantly smaller as indicated by decreases in ε.

Combined with the decreases in $\mathcal{S}$ for intensity this indicates that the static Unicom model likely works well for predicting the Unicom's effects on static pupils. Verification with additional measurements would however be advisable to investigate if the same error reductions are obtained for measurements that are not used during the optimization of c. These verifications would also give a further indication if $\mathcal{M}$ does not just by chance capture effects that are not due to the Unicom. Results of verification using scanning measurements will be presented next after a short summary of the running time required by $\mathcal{M}$.

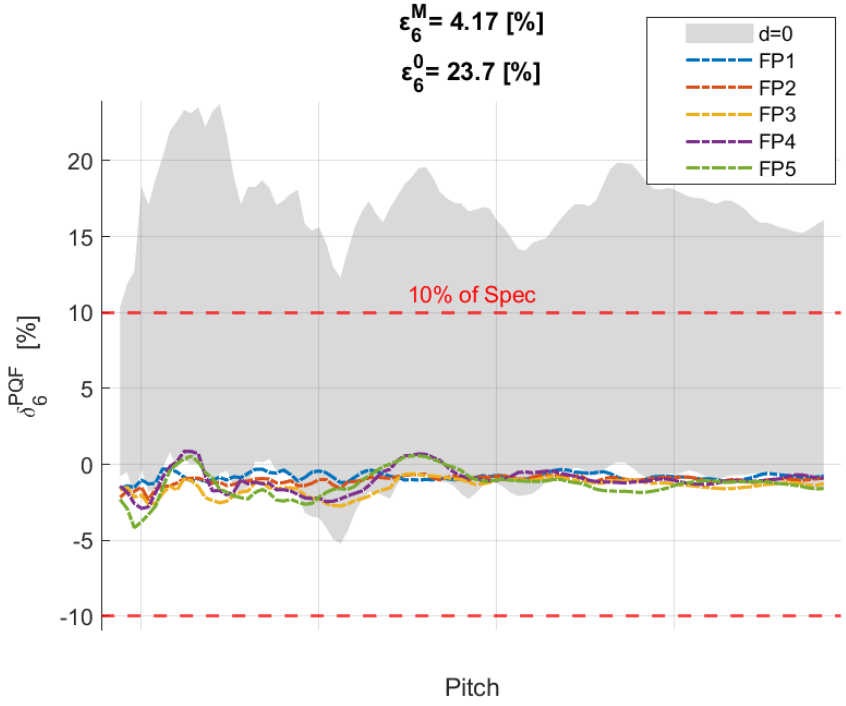

Fig. 6.4: Plot of $\boldsymbol{\delta}_6^{\mathrm{PQF}}({}_{\mathcal{M}}\mathbb{j}^{\perp\mathbf{d}_1}, \mathbb{j}^{\perp\mathbf{d}_1})$ for 5 FPs (dot-dashed lines) over a range of pitches. The area between the maximum and minimum of $\boldsymbol{\delta}_6^{\mathrm{PQF}}$ for the same 5 FPs without using $\mathcal{M}$ at each pitch is depicted in grey. $\boldsymbol{\delta}$-s are given as a percentage of the machine's spec with the 10% deviation from zero shown as red dashed lines.

Speed

During the investigation presented in this thesis $\mathcal{M}$ was run on a laptop with an 11th Gen Intel Core i5 2.60GHz processor and 16GB of RAM. The model, coded in MATLAB, can be executed in a couple of different scenarios: with varying numbers of grid refinement, ω, during interpolation and with or without supplying pre-calculated interpolation results. Execution times for some scenarios are given in Table 4. Presented running times, T_{avg}, were calculated as the arithmetic mean execution time of 10 consecutive runs.

ω	interpolation	T_{avg} [s]	interpolation	T_{avg} [s]
0	during	8.78	pre-calculated	6.22
1	during	12.4	pre-calculated	6.69
2	during	24.6	pre-calculated	9.64
3	during	62.0	pre-calculated	25.9
4	during	274	pre-calculated	491

Table 4: Average running time of 10 consecutive runs of $\mathcal{M}$, for various values of ω with and without pre-calculated interpolated intensities.

Even though the model was not yet optimized for execution speed, running times are fairly short for up

to 3 times mesh refinement, especially considering that new predictions for setting Unicom fingers to new settings on the machine can be calculated using pre-calculated interpolation results from previous runs. Noteworthy is that for $\omega = 4$, pre-calculated interpolation is slower than interpolation during the model run, which might be the result of inefficiencies in trying to keep input and working data in memory at the same time.

Currently, interpolation is also performed with grid refinement in both the x- and y-direction. This is mainly interesting when the changes of pupils throughout the entire slit are being investigated or if the effect of the Unicom on the slit is also examined. However, if for PQF calculations only pupils at a limited number of FPs are needed, only performing interpolation in the y-direction would suffice if input measurements already contain these FPs. Thus for this use case, interpolation in x-direction could be removed to speed up the model by decreasing the number of grid points by 2^{ω}, in addition to using the speed up tricks mentioned in Chapter 5.

6.3 Performance of the scanning pupil prediction scheme

In this section the performance of SPPS with c fixed to -1.84 and $\omega = 3$ is quantified by using the metric S for its intensity and ε for its PQF. Results were obtained for three different Unicom settings, $\mathbf{d}_2$, $\mathbf{d}_3$ and $\mathbf{d}_4$, where fingers were uniformly inserted as illustrated in Figure 6.5. These Unicom setups were chosen because they were used to obtain the only suitable scanning measurements available.

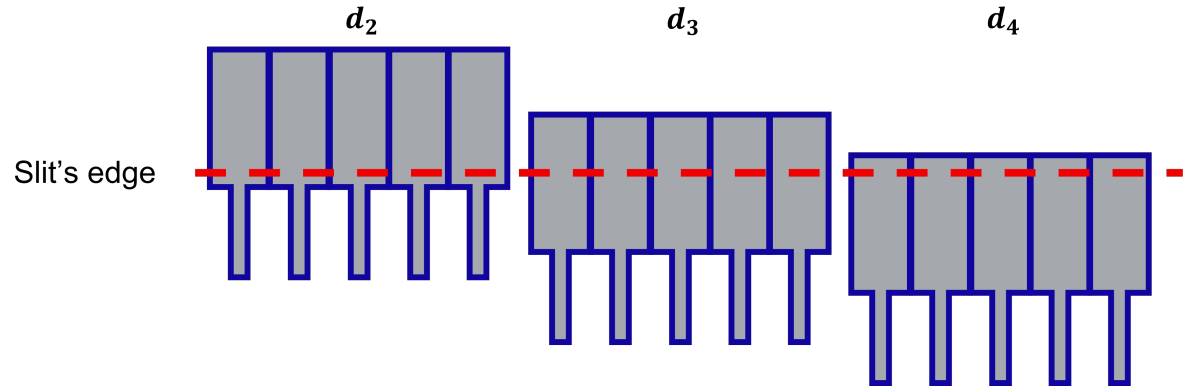

Fig. 6.5: Illustration of the patterns of Unicom finger insertion specified by $\mathbf{d}_2$, $\mathbf{d}_3$ and $\mathbf{d}_4$ for a few fingers, ignoring slit curvature.

Intensity

By including SPPS when using parcellated scanning pupils without Unicom finger insertions, $\mathbb{j}^{*\perp\mathbf{0}}$, to predict parcellated scanning pupils with Unicom pattern $\mathbf{d}_2$, $\mathbf{d}_3$ and $\mathbf{d}_4$, $\mathbb{j}^{*\perp\mathbf{d}}$, error reductions of 79.1%, 56.5% and 15.3% respectively were realized for $\sqrt{\mathcal{S}}$ with normalized parcellated pupils. The maximum absolute deviation within normalized pupil predictions, $\sqrt{\mathcal{S}^{\infty}}$, changed by 76.9%, 71.6% and 43.7% respectively, as shown in Table 5.

The fact that both S and S^{∞} decreased for each tested finger configuration indicates that SPPS effectively increases the prediction accuracy for the intensity distribution of scanning pupils, whilst at the same time reducing the maximum errors that are made. This means that on average predicted pupils are more similar to their measured counterpart and the largest differences between these pupils are also smaller.

Most important, as the S error reductions show, SPPS consistently lead to decreased errors when predicting the entire pupil. In combination with the fact that the parameter c was optimized to static data and not the scanning data used here, this implies that $\mathcal{M}$ generalizes quite well to predicting the Unicom's impact on different pupil measurements of the same pupil on the same machine. This result should not come as a surprise because $\mathcal{M}$ was setup with the design of the machine and not the exact data in mind. Another notable, yet expected characteristic of SPPS, and thus likely also of $\mathcal{M}$, is that attained error reductions are larger when the Unicom fingers are inserted deeper into the slit. Since SPPS predicts the Unicom's impact and corrects the error between two scanning measurements based

	$\sqrt{\mathcal{S}\left(\mathbb{j}^{\perp \mathbf{0}}, \mathbb{j}^{*\perp \mathbf{d}}\right)}$	$\sqrt{\mathcal{S}\left(\mathbb{j}^{\perp \mathbf{d}}, \mathbb{j}^{*\perp \mathbf{d}}\right)}$	Error reduction [%]
$\mathbf{d}_2$	$3.02 \cdot 10^{-2}$	$6.30 \cdot 10^{-3}$	79.1
$\mathbf{d}_3$	$1.18 \cdot 10^{-2}$	$5.12 \cdot 10^{-3}$	56.5
$\mathbf{d}_4$	$5.77 \cdot 10^{-3}$	$4.88 \cdot 10^{-3}$	15.3
	$\sqrt{\mathcal{S}^{\infty}\left(\mathbb{j}^{\perp \mathbf{0}}, \mathbb{j}^{*\perp \mathbf{d}}\right)}$	$\sqrt{\mathcal{S}^{\infty}\left(\mathbb{j}^{\perp \mathbf{d}}, \mathbb{j}^{*\perp \mathbf{d}}\right)}$	Error reduction [%]
$\mathbf{d}_2$	$3.14 \cdot 10^{-3}$	$7.25 \cdot 10^{-4}$	76.9
$\mathbf{d}_3$	$1.49 \cdot 10^{-3}$	$4.22 \cdot 10^{-4}$	71.6
$\mathbf{d}_4$	$7.23 \cdot 10^{-4}$	$4.07 \cdot 10^{-4}$	43.7

Table 5: Square root values of the $\mathcal{S}$ and $\mathcal{S}^{\infty}$ errors for predictions without and with use of SPPS and the reduction of errors by using SPPS. Predictions and measurements were performed for $\mathbf{d} = \mathbf{d}_1$.

on this prediction, it is logical that a bigger part of the error can be accounted for if the Unicom causes a bigger part of this error relative to other error sources. When the Unicom fingers are inserted further into the slit they block more light, which leads to an increased difference between measurements with and without the fingers inserted.

PQF

PQF errors given in $\boldsymbol{\varepsilon}$ dropped by between 32.1% to 76.0%, -15.9% to 57.9% and -21.3% to 40.2% for $\mathbf{d}_2$, $\mathbf{d}_3$ and $\mathbf{d}_4$ respectively when using SPPS as shown in Table 7. Using SPPS lead to a decrease or equivalence in errors in all cases except for the third PQF-parameter, for which errors increased by 15.9% and 21.3% for $\mathbf{d}_3$ and $\mathbf{d}_4$ respectively. Again, SPPS generally achieves larger error reductions when fingers are inserted further into the slit.

The comparison between the fifth type of PQF deltas with and without SPPS for $\mathbf{d}_2$ are shown in Figure 6.6.

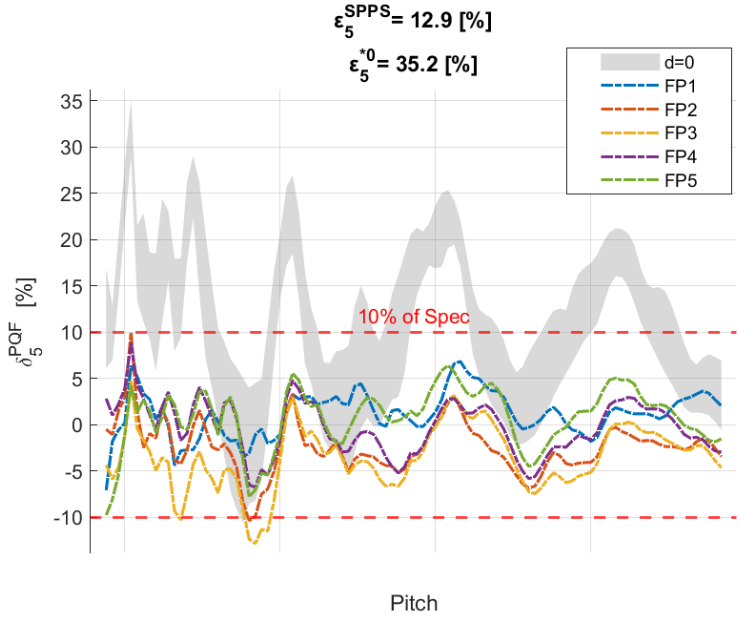

Fig. 6.6: Plot showing $\boldsymbol{\delta}_5^{\mathrm{PQF}}(\mathbb{j}^{\perp \mathbf{d}_2}, \mathbb{j}^{*\perp \mathbf{d}_2})$ for 5 FPs (dot-dashed lines) over a range of pitches. The area between the maximum and minimum of $\boldsymbol{\delta}_5^{\mathrm{PQF}}$ for the same 5 FPs without using SPPS at each pitch is depicted in grey. $\boldsymbol{\delta}$-s are given as a percentage of the machine's spec with the 10% deviation from zero shown as red dashed lines.

Not only does the difference between $\varepsilon^{*0} = \varepsilon(\mathbb{j}^{*\perp\mathbf{0}}, \mathbb{j}^{*\perp\mathbf{d}_2})$ and $\varepsilon^{\mathrm{PQF}} = \varepsilon(\mathbb{j}^{\perp\mathbf{d}_2}, \mathbb{j}^{*\perp\mathbf{d}_2})$ show that the maximum absolute deviation of the delta from zero decreases, clearly the deltas when using SPPS are also much closer to zero for almost all pitches. This squeezes the prediction errors from well outside the bound of 10% of machine spec to mostly inside the desired accuracy again.

The exceptional case where the ε-error increases by 21.3% is depicted in Figure 6.7. As can be seen there, the impact using SPPS has on δ^{PQF} seems somewhat preserve the patterns that are present in the delta without SPPS but amplify those for some pitches. This behavior for the third PQF-parameter warrants future investigation into the behavior PQF-parameters in general to uncover how they might be impacted by certain changes in pupils. Although for $\mathbf{d}_3$ and $\mathbf{d}_4$ prediction accuracy for this parameter decreased, for $\mathbf{d}_2$ SPPS increased prediction accuracy. This gives rise to two possibilities, either SPPS does not capture the Unicom's effects on this PQF parameter well enough to reduce the deltas, or the remaining deltas for $\mathbf{d}_3$ and $\mathbf{d}_4$ are caused to a large extent by measurement to measurement differences which are not caused by the Unicom. Since the increased ε-error concerns $\mathbf{d}_3$ and $\mathbf{d}_4$ with moderate and little Unicom finger insertion, if for one of some of the measurements the largest fraction of initial errors was due to non-Unicom related effects, it would likely be these measurement. Therefore, a case can be made that remaining errors are due to both the corrections of SPPS that do not capture effects on this PQF-parameter in a completely accurate manner and due to measurement to measurement differences unrelated to the Unicom. However, to be certain about how large non-Unicom related variations between measurements are, collecting a collection of a few different measurements with the Unicom fingers extracted and different times between measurements would be advisable.

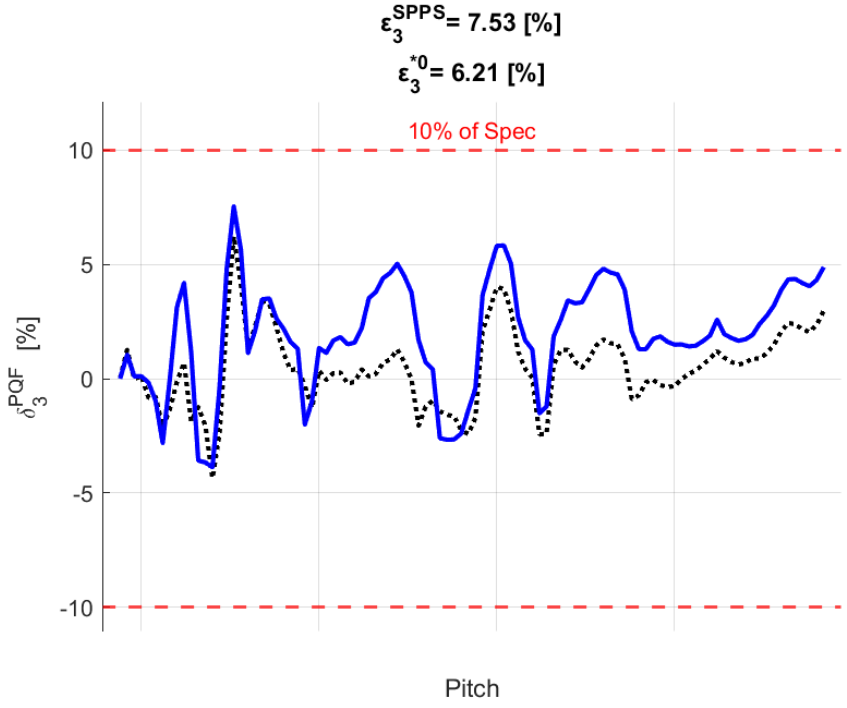

Fig. 6.7: Plot of $\boldsymbol{\delta}_3^{\mathrm{PQF}}(\mathbb{j}^{\perp\mathbf{d}_4}, \mathbb{j}^{*\perp\mathbf{d}_4})$ for 5 FPs (dot-dashed lines) over a range of pitches. The area between the maximum and minimum of $\boldsymbol{\delta}_3^{\mathrm{PQF}}$ for the same 5 FPs without using SPPS at each pitch is depicted in grey. $\boldsymbol{\delta}$-s are given as a percentage of the machine's spec with the 10% deviation from zero shown as red dashed lines.

Speed

Similar to the execution time of $\mathcal{M}$, the execution times of SPPS are reasonably short until $\omega = 4$, for which the required time rapidly ramps up as shown in Table 6. Again the average running time was calculated from 10 consecutive runs with pre-calculated interpolation results and parcellated pupils in cache. This situation with pre-calculated interpolated slits and parcellated pupils is realistic in most cases as the static input and scanning input pupils for SPPS can be measured once and then used to

calculate results for many different Unicom configurations.

ω	interpolation	T_{avg} [s]
0	pre-calculated	8.70
1	pre-calculated	9.42
2	pre-calculated	12.5
3	pre-calculated	31.4
4	pre-calculated	540

Table 6: Average running time of 10 consecutive runs of SPPS, for various values of ω with pre-calculated interpolated intensities.

6.4 Performance overview

Here a brief overview of the performance of the static Unicom model, $\mathcal{M}$, and the scanning pupil prediction scheme, SPPS, are presented, see Table 7. The ε-errors denote the maximum absolute difference in PQF of the predicted and the measured pupils. The left most column in each block of Table 7 gives the errors without using $\mathcal{M}$ or SPPS, the middle column represents the errors whilst using $\mathcal{M}$ or SPPS. The top left block shows values regarding static pupil measurements with finger insertion $\mathbf{d}_1$. The remaining three blocks give the errors for scanning pupil predictions with insertions $\mathbf{d}_2$ (top right), $\mathbf{d}_3$ (bottom left) and $\mathbf{d}_4$ (bottom right).

	$\varepsilon^{\mathbf{0}}(\mathbf{d}_1)$	$\varepsilon^{\mathcal{M}}(\mathbf{d}_1)$	Error reduction [%]	$\varepsilon^{*\mathbf{0}}(\mathbf{d}_2)$	$\varepsilon^{\mathbf{SPPS}}(\mathbf{d}_2)$	Error reduction [%]
1	12.1	3.83	68.3	38.4	9.21	76.0
2	9.01	4.75	47.3	26.1	7.94	69.6
3	14.7	7.02	52.2	22.1	13.1	40.7
4	19.7	5.78	70.7	24.0	16.3	32.1
5	27.2	3.69	86.4	35.2	12.9	63.4
6	23.7	4.17	82.4	30.4	7.36	75.8
7	17.6	2.77	84.3	27.6	11.3	59.1
	$\varepsilon^{*\mathbf{0}}(\mathbf{d}_3)$	$\varepsilon^{\mathbf{SPPS}}(\mathbf{d}_3)$	Error reduction [%]	$\varepsilon^{*\mathbf{0}}(\mathbf{d}_4)$	$\varepsilon^{\mathbf{SPPS}}(\mathbf{d}_4)$	Error reduction [%]
1	12.8	5.39	57.9	12.3	7.35	40.2
2	10.4	7.04	32.3	12.0	9.55	20.4
3	6.92	8.02	-15.9	6.21	7.53	-21.3
4	11.7	11.7	0.00	4.91	3.92	20.2
5	10.6	8.88	16.2	12.3	8.03	34.7
6	10.9	6.16	43.5	9.03	5.43	39.9
7	14.2	11.7	17.6	11.8	11.8	0.00

Table 7: Values of the ε-errors of predicting static pupils (top left) without $\mathcal{M}$, with $\mathcal{M}$ and the reduction in error obtained by using $\mathcal{M}$. Similarly ε-errors for scanning pupils ($\mathbf{d}_2$ top right, $\mathbf{d}_3$ bottom left, $\mathbf{d}_4$ bottom right) with and without SPPS and the associated error reduction.

The ε-errors Table 7 were remained constant or decreased for all but one of the PQF-parameters when adapting predictions by using $\mathcal{M}$ for static pupils and SPPS for scanning pupils. This means that in most cases correcting for the Unicom's effects on pupils by using $\mathcal{M}$ or SPPS is beneficial to increase the accuracy with which PQF-values for pupils can be predicted. In combination with the improved S values in Table 3 and Table 5 showing that in the same cases, significant improvements in predicting the intensity distribution within pupils are obtained, the results indicate that incorporating the Unicom model constructed in this thesis in most cases has serious benefits to prediction accuracy. Furthermore, as Table 4 and Table 6 show, incorporating a Unicom model should not pose difficulties due to time constraints as even the not yet speed optimized model requires little running time, in particular considering that a Unicom model could likely be ran with pre-calculated interpolation and pre-parcellated pupils whilst EUV machines are processing wafers.

In Table 7 as well as in Table 5 larger accuracy improvements are achieved for setups in which the

unicom fingers are inserted further into the slit. Especially for $\mathbf{d}_1$, $\mathbf{d}_2$ and $\mathbf{d}_3$, significant improvements in prediction accuracy were obtained. That the obtained accuracy gains are larger when the Unicom fingers are inserted deeper into the slit is quite logical. The Unicom model is build to correct pupil predictions for the effects of the Unicom. When the Unicom fingers are inserted deeper into the slit the Unicom will cause a larger difference between a measurement with and without inserted fingers. If the differences between both measurements introduced by other sources of error remain roughly constant, this means that with deeper insertion of the fingers a larger fraction of the total difference between both measurements will be due to the Unicom. Therefore, a larger fraction of the prediction error for pupils can be corrected when the Unicom fingers are inserted deeper into the slit.

The 15.9% and 21.3% increases in $\varepsilon^{\mathbf{SPPS}}(\mathbf{d}_3)$ and $\varepsilon^{\mathbf{SPPS}}(\mathbf{d}_4)$ respectively in Table 7 together with the remaining deltas with and without SPPS shown in Figure 6.7, are likely to be indicative of a combination of a limited capability of the Unicom model to capture the Unicom's effects on the third PQF-parameter and of differences contained in the measurements used which are not Unicom related. Thus, to verify how large the expected differences between measurements are without the Unicom involved, identical measurements with extracted Unicom fingers could be repeated over a longer period of time. Not only would these measurements serve to quantify expected variation between measurements, but they would also give an indication as to for how long an executed measurement would still represent the current machine state to high accuracy. In turn, because these measurements are obtained without the Unicom involved, they might be used to estimate how large the prediction errors due to the Unicom are and thus to what degree it would be reasonable to expect a Unicom model to correct for these errors.

6.5 Future work

The physics based Unicom model constructed in this thesis is highly dependent on the physical dimensions of the Unicom fingers, their location in the machine and the path of light through the machine. Therefore, obtaining a deeper understanding of these physical properties of the machine would enable further improvements of the model. The description of conic propagation of light through the machine for instance might be investigated in more detail in the future as currently the description of the spatially dependent divergence of slits seems to assume a single point of convergence for all FFIs. This assumption might not exactly hold because in reality the FFIs originate from different PFMs and are not perfectly aligned at RL. Effects that are of minor influence but might be interesting to add to the model include: up and down movement of the Unicom fingers when they are inserted further into the slit; thermal expansion of the Unicom fingers; and slight perturbations of Unicom finger dimensions due to the manufacturing process.

Additional measurement data would be needed to determine an upper bound for how big the potential accuracy gains are that could be obtained by further improvements of the Unicom model. By performing multiple measurements of identical pupils with extracted Unicom fingers at set moments in time, valuable insight into measurement to measurement variations could be acquired. These insights could be used to determine which fraction of difference between two measurements that is due to the Unicom and could thus potentially be corrected for using a Unicom model. Further investigation into the validity of the Unicom model for additional static measurements, to which the model parameter is not optimized, and using scanning measurements from different machines could also give valuable insight into how well the model generalizes.

As the model is based in large part on machine design, the author expects the model to generalize quite well, at least when using measurements as input that are obtained from the same machine for which predictions are made, though re-optimization of the free model parameter might be required. However, enriching the current study of the performance of the Unicom model with verification using measurements from additional machines would be advisable if the model is to be used on multiple machines. The first step in applying the model to a new machine would consist of knowing exactly which design of Unicom fingers is installed on that machine.

The most direct future implementation of the Unicom model would be to incorporate it into the algorithm that predict pupils from a set of measured basis pupils to enable the algorithm to account for effects of the Unicom. Additional future implementations of the Unicom model could be used in: predictions of 2D attenuation by the Unicom throughout the slit that does account for possible overlap of fingers and could be used to find optimal finger positions; a combined study of PQF and SU to

find Unicom finger settings that balance both; studies of the effects of changes to the shapes of the Unicom fingers or their position on pupils and the slit or, equivalently studies investigating the effects of a changed light path. For a more data driven approach of improving the model, additional free parameters could be added to heights of the Unicom fingers or angles of the light path in the model and optimized to multiple measurements. Such additional parameters could then also be adjusted along with the shape of the Unicom fingers in the model to study the impact of changes to the Unicom's design or the effects of fabrication errors on pupils and the slit.

7 Conclusion

In this thesis, a model to predict the effects of inserting Unicom fingers into the beam of light of EUV lithography machines was constructed. Supplied with static pupil measurements for fully extracted Unicom fingers and the desired insertion of each finger, this model predicts the static pupil as it would be measured with the desired finger insertions. The model calculates predictions through custom ray-tracing using the physical properties of the EUV machines. To allow for some flexibility, the model contains one free parameter which can be optimized to a single measurement to adjust for machine to machine differences.

Including the static Unicom model when predicting pupils with inserted Unicom fingers from pupils with extracted fingers, increased prediction accuracy by 73.9% to 90.3% and by 47.3% to 86.4% when considering the intensity and PQF-parameters respectively of the pupils contained in the static measurements used in this study. These significant accuracy gains were obtained despite the fact that the measurements used for verification of the prediction accuracy and the measurements supplied to the model as input also differ from each other due to non-Unicom related effects. Execution times of the model averaged 62 s and 25.9 s for first use and repeated (with some data pre-processed) use respectively and as such should not pose significant challenges when including the model in quick routines, especially since the model can easily be adapted to be even faster for specific use cases.

Using the developed static Unicom model, a scanning pupil prediction scheme, SPPS, was designed. This scheme utilizes the differences between the input and the output of the static Unicom model to attenuate a scanning pupil measurement with extracted Unicom fingers. The elegance of this method lies in the possibility to obtain scanning pupil predictions for each possible configuration of the Unicom whilst only requiring to measure the static pupil once. By updating the input scanning pupil measurement with extracted Unicom fingers as new measurements become available, the scheme accounts for effects such as collector contamination and mirror degradation that affect a machine over time.

Predictions made for scanning pupils with inserted Unicom fingers from scanning pupils with extracted Unicom fingers showed 15.3% to 79.1% and -21.3% to 76.0% increases in accuracy for the intensity distribution and PQF-parameters respectively when using SPPS for three different Unicom configurations. When Unicom fingers were inserted further into the slit and the impact of the Unicom was larger, more accuracy could be gained by enlisting SPPS. Overall, accuracy gains for some PQF-parameters were quite substantial even when only a small part of the Unicom fingers was inserted into the slit. Apart from a single PQF-parameter, for which prediction accuracy became worse for two of the three tested Unicom configurations, all investigated parameters indicated that using SPPS predictions of equivalent or significantly increased accuracy can be achieved. Why accuracy decreased for only this single PQF-parameter, remains a topic for future investigations. The average execution time of SPPS was 31.4 s for repeated use and thus does not limit the use of SPPS in an environment where scanning pupils are already parcellated for other procedures.

Although the created Unicom model and SPPS do not always succeed in reducing prediction errors to within 10% of the spec for PQF, in many cases prediction errors are improved form out of spec to in spec. Furthermore, in almost all cases significant prediction improvements are attained using the model and SPPS at little computational cost. Therefore, the author recommends including the Unicom model in calculating pupil predictions if improved accuracy is desired.

Future investigations delving deeper into the exact path of the light through the EUV machine might enable a more complete description of the effects of the Unicom on pupils. This more complete description might lead to Unicom model with even better accuracy. The current model could already be incorporated into algorithms that predict pupils, or in algorithms which use a prediction of the attenuation of the slit by the Unicom to position the Unicom fingers. However, before enlisting the Unicom model in such algorithms for use on many machines, enriching the current study of the Unicom model's performance based using measurements from multiple additional machines would be advisable as the needed data was available for only one machine at the time the current study was performed.

References

[1] M. Stickel and F. Tardo. Cloud computing, 5g, metaverse, electric vehicles among the most important areas of technology in 2023, says new ieee study. (accessed: Aug. 7, 2023). [Online]. Available: https://www.ieee.org/about/news/2022/news-release-2022-survey-results.html?_gl=1*ricbsz*_gcl_au*MTkyNDQ2MzE1OS4xNjkxNDEyNDcz*_ga*MTE2MjYwNDgwNC4xNjkxNDEyNDcz*_ga_H0YHKP362D*MTY5MTQxMjQ3My4xLjEuMTY5MTQxMjcyNi42MC4wLjA.&_ga=2.55214760.2025009200.1691412473-1162604804.1691412473

[2] A. Pirati *et al.*, "Euv lithography performance for manufacturing: status and outlook," vol. 9776, International Society for Optics and Photonics. SPIE, Mar. 2016, p. 97760A. [Online]. Available: https://doi.org/10.1117/12.2220423

[3] W. Allan. Installed base management opportunity. (accessed: Oct. 26, 2023). [Online]. Available: https://www.asml.com/en/investors/investor-days/2021

[4] B. Dassen, "Detecting Abnormal Behavior in Lithography Machines," M.S. thesis, Dept. Math. Comput. Sci., Eindhoven Univ. Tech., Netherlands, 2019. [Online]. Available: https://research.tue.nl/en/studentTheses/detecting-abnormal-behavior-in-lithography-machines

[5] W. Cheng, Y. Zhang, J. Zhu, B. Yang, A. Zeng, and H. Huang, "Programmable uniformity correction by using plug-in finger arrays in advanced lithography system," *Opt. Commun.*, vol. 392, pp. 77–85, 2017. [Online]. Available: https://doi.org/10.1016/j.optcom.2017.01.023

[6] S. Gong, B. Yang, and H. Huang, "Illumination uniformity correction by using dynamic gray filters in a lithography system," *Appl. Opt.*, vol. 61, no. 10, pp. 2706–2714, Apr. 2022. [Online]. Available: https://opg.optica.org/ao/abstract.cfm?URI=ao-61-10-2706

[7] P. Ginestra, M. Madou, and E. Ceretti, "Production of carbonized micro-patterns by photolithography and pyrolysis," *Precis. Eng.*, vol. 55, pp. 137–143, Jan, 2019. [Online]. Available: https://www.sciencedirect.com/science/article/pii/S0141635918303477

[8] P. van Gerven. Asml for beginners. (accessed: Oct. 2, 2023). [Online]. Available: https://bits-chips.nl/artikel/asml-for-beginners/

[9] F. Balestra, M. Graef, Y. Hayashi, H. Ishiuchi, T. Conte, and P. Gargini. International roadmap for devices and systems. (accessed: Oct. 2, 2023). [Online]. Available: https://irds.ieee.org/images/files/pdf/2021/2021IRDS_ES.pdf

[10] C. Mack, *Fundamental Principles of Optical Lithography: The Science of Microfabrication*. Chichester, England: Wiley, 2007.

[11] A. Nordmann. Wave diffraction in the manner of huygens and fresnel. (accessed: Oct. 4, 2023). [Online]. Available: https://en.wikipedia.org/wiki/Huygens%E2%80%93Fresnel_principle#/media/File:Refraction_on_an_aperture_-_Huygens-Fresnel_principle.svg

[12] ASML. Euv lithography systems. (accessed: Oct. 12, 2023). [Online]. Available: https://www.asml.com/en/products/euv-lithography-systems

[13] A. Pirati *et al.*, "The future of euv lithography: enabling moore's law in the next decade," vol. 10143, International Society for Optics and Photonics. SPIE, Mar. 2017, p. 101430G. [Online]. Available: https://doi.org/10.1117/12.2261079

[14] R. Voelkel, "Micro-optics: enabling technology for illumination shaping in optical lithography," vol. 9052, International Society for Optics and Photonics. SPIE, Mar. 2014, p. 90521U. [Online]. Available: https://doi.org/10.1117/12.2046116

[15] "Internal communications," ASML.

[16] R. C. Zimmerman, "Double EUV Uniformity Correction System and Method," U.S. Patent 9,134,620 B2, Apr. 13, 2011. [Online]. Available: https://patentimages.storage.googleapis.com/44/8b/35/03cefc151b0b8a/US9134620.pdf

[17] J. Nath emphet al., "Lithographic apparatus and illumination uniformity correction system," U.S. Patent 11,656,555 B2, May 23, 2023. [Online]. Available: https://patentimages.storage.googleapis.com/8b/c6/58/db7825a4f057da/US11656555.pdf

[18] "Internal communications," ASML.

[19] "Internal communications," ASML.

[20] "Internal communications," ASML.

[21] "Internal communications," ASML.

[22] K. Jeong, A. B. Kahng, C.-H. Park, and H. Yao, "Dose map and placement co-optimization for timing yield enhancement and leakage power reduction," in *Proc. 45th Annu. Des. Automat. Conf.*, 2008, p. 516–521. [Online]. Available: https://doi-org.tudelft.idm.oclc.org/10.1145/1391469.1391600

[23] J.M.D. Stoeldraijer and J.W.R. Ten Cate and F.H.A.G. Fey and J. Sytsma, "Lithographic apparatus with filters for optimizing uniformity of an image," U.S. Patent 6,404,499 B1, June 11, 2002. [Online]. Available: https://patentimages.storage.googleapis.com/c7/93/c4/81f95aa3efe22c/US6404499.pdf

[24] Y. He, T. Xing, W. Lin, Z. Liao, and W. Liu, "Method for illumination uniformity correction in the illumination system of lithography," *Optik*, vol. 228, Feb. 2021. [Online]. Available: https://doi.org/10.1016/j.ijleo.2020.166172

[25] "Internal communications," ASML.

[26] "Internal communications," ASML.

[27] R. Voelkel and K. J. Weible, "Laser beam homogenizing: limitations and constraints," in *Opt. Fabr., Test., Metrol. III*, 2008, p. 71020J. [Online]. Available: https://doi.org/10.1117/12.799400

[28] H. Le *et al.*, "Effects of top-hat laser beam processing and scanning strategies in laser micro-structuring," *Micromachines*, vol. 11, no. 2, Feb. 2020. [Online]. Available: https://doi.org/10.3390/mi11020221

[29] N. C. Giglio, H. M. Grose, and N. M. Fried, "Comparison of fiber-optic linear beam shaping designs for laparoscopic laser sealing of vascular tissues," *Opt. Eng.*, vol. 61, no. 2, Feb. 2022. [Online]. Available: https://doi.org/10.1117/1.OE.61.2.026112

[30] Y. E. B. Vidhya and N. J. Vasa, "Enhancement in Photoconductivity of a-Si thin Films by Annealing and Texturing Technique with the Third Harmonic Output from a Pulsed Nd3+:YAG Laser," in *44th North Amer. Manuf. Res. Conf.*, 2016, pp. 734–746. [Online]. Available: https://doi.org/10.1016/j.promfg.2016.08.060

[31] Ansys. Zemax optics software. (accessed: Nov. 5, 2023). [Online]. Available: https://www.zemax.com/

[32] COMSOL. Comsol multiphysics software. (accessed: Nov. 5, 2023). [Online]. Available: https://www.comsol.com/

[33] MathWorks. Documentation: griddedinterpolant. (accessed: Nov. 28, 2023). [Online]. Available: https://nl.mathworks.com/help/matlab/ref/griddedinterpolant.html

[34] H. Akima, "A method of bivariate interpolation and smooth surface fitting based on local procedures," *Commun. ACM*, vol. 17, no. 1, p. 18–20, Jan. 1974. [Online]. Available: https://doi.org/10.1145/360767.360779

[35] C. Ionita. Makima piecewise cubic interpolation. (accessed: Oct. 30, 2023). [Online]. Available: https://blogs.mathworks.com/cleve/2019/04/29/makima-piecewise-cubic-interpolation/

[36] "Internal communications," ASML.

A Mathematical definitions

This appendix defines some mathematical operators used in this thesis and elaborates on of few key properties of these operators.

The Heaviside step function
The Heaviside step function is defined as:

$$H(x) \coloneqq \begin{cases} 1 & \text{if} \quad x \geq 0 \\ 0 & \text{otherwise} \end{cases}. \tag{A.1}$$

By combining two shifted Heaviside step functions the function of a single square impulse of width T can be created:

$$u(x) \coloneqq H\left(x + \frac{T}{2}\right) - H\left(x - \frac{T}{2}\right). \tag{A.2}$$

The Dirac delta function
The Dirac delta function can be defined using the Heaviside step function as:

$$\delta(x) \coloneqq \frac{dH(x)}{dx}. \tag{A.3}$$

The Dirac delta function can be thought of as zero everywhere except at $x = 0$ where it is infinite. Using $\delta(x)$ a Dirac comb with spacing 2T can be defined:

$$v(x) \coloneqq \sum_{j=-\infty}^{\infty} \delta\left(x - j2T\right). \tag{A.4}$$

The Fourier transform
The Fourier transform is an operator which maps inputted functions to corresponding functions that describe the frequencies contained in the input function. For an integrable function $g : \mathbb{R} \to \mathbb{C}$ the Fourier transform can be defined as:

$$\mathcal{F}_{1D}\{g\}(f_x) \coloneqq \int_{-\infty}^{\infty} g(x) e^{-2\pi i x f_x}\, dx, \tag{A.5}$$

with $\mathcal{F}_{1D}\{\cdot\}$ the 1D Fourier transform, i defined by $i^2 \coloneqq -1$ and f_x the independent variable of the function corresponding to g representing frequency in the x-direction. Similarly, the more general 2D Fourier transform is defined for an integrable function $h : \mathbb{R}^2 \to \mathbb{C}$ as:

$$\mathcal{F}\{h\}(f_x, f_y) \coloneqq \int_{-\infty}^{\infty} \int_{-\infty}^{\infty} h(x, y) e^{-2\pi i (f_x x + f_y y)}\, dx\, dy, \tag{A.6}$$

with $\mathcal{F}\{\cdot\}$ the 2D Fourier transform and f_y the independent variable of the function corresponding to g representing frequency in the y-direction.

The inverse of a Fourier transform, denoted $\mathcal{F}^{-1}$ is the transform that, with $u : \mathbb{R}^n \to \mathbb{C}$, $n \in \mathbb{N}\backslash 0$, an L^1 integrable function, for almost every $\mathbf{x} \in \mathbb{R}^n$ satisfies the relationship:

$$\mathcal{F}^{-1}\{\mathcal{F}\{u\}\}(\mathbf{x}) = u(\mathbf{x}). \tag{A.7}$$

For the 1D Fourier transform the inverse is obtained as:

$$\mathcal{F}^{-1}\{G\}(x) = \int_{\infty}^{\infty} G(f_x) e^{2\pi i f_x x}\, df_x. \tag{A.8}$$

The Fourier transform satisfies the convolution theorem, thus if $u, v : \mathbb{R}^n \to \mathbb{C}$ with $n \in \mathbb{N}\backslash 0$ are L^1 integrable functions the following holds:

$$(u * v)(\mathbf{x}) = \mathcal{F}_n^{-1}\{\mathcal{F}_n\{u\} \cdot \mathcal{F}_n\{v\}\}(\mathbf{x}), \tag{A.9}$$

where $\mathcal{F}_n$ and $\mathcal{F}_n^{-1}$ are the n-dimensional Fourier transform and its inverse respectively and $*$ denotes the convolution of the two functions:

$$(u * v)(\mathbf{x}) \coloneqq \int_{\mathbb{R}^n} u(\tau)v(\mathbf{x} - \tau)\, d\tau. \tag{A.10}$$

Now again considering u and v the functions defined in Equation A.2 and Equation A.4 the function of an infinite square wave with period 2T and duty cycle, the fraction of the total time which is spent in the high part of the wave, of 0.5 can be defined as:

$$w(x) \coloneqq (u * v)(x). \tag{A.11}$$

Note that $w(x)$ is a description of a 1D pattern of equal lines-and-spaces. The Fourier transforms of u and v are frequently used and present in many tables of Fourier transform pairs such as found in [10]. The transform of u is given by:

$$\mathcal{F}\{u\}(f_x) = T\text{sinc}(Tf_x), \tag{A.12}$$

with $\text{sinc}(x) \coloneqq \sin(\pi x)/(\pi x)$. The Fourier transform of v is:

$$\mathcal{F}\{v\}(f_x) = \frac{1}{2T} \sum_{j=-\infty}^{\infty} \delta\left(f_x - \frac{j}{2T}\right). \tag{A.13}$$

By applying the convolution theorem and subsequently substituting the Fourier transforms of both u and v, the Fourier transform of $w(x)$ can be found:

$$\begin{aligned} \mathcal{F}\{w\}(f_x) &= (\mathcal{F}\{u\} \cdot \mathcal{F}\{v\})(f_x) \\ &= T\text{sinc}(Tf_x) \cdot \frac{1}{2T} \sum_{j=-\infty}^{\infty} \delta\left(f_x - \frac{j}{2T}\right) \\ &= \frac{1}{2}\text{sinc}(Tf_x) \cdot \sum_{j=-\infty}^{\infty} \delta\left(f_x - \frac{j}{2T}\right). \end{aligned} \tag{A.14}$$

The resulting Fourier transform consists of delta pulses at frequencies that are a multiple of $1/(2T)$. Each of these delta pulses is scaled with the value of $(1/2)\text{sinc}(Tf_x)$ corresponding its location in the frequency domain. From the Fourier transform of w it becomes apparent that when the period, 2T, of a square wave becomes smaller, the delta pulses of its Fourier transform will be spread further apart. Since the square wave describes a pattern of equal lines-and-spaces this means that shrinking the size of the lines and spaces will result in diffraction orders, delta pulses, that have more distance between them.

Another property used in this thesis is the frequency shift property of the Fourier transform, this property can directly be derived from the definition of the Fourier transform:

$$\begin{aligned} \mathcal{F}\{he^{2\pi i(f'_x x + f'_y y)}\}(f_x, f_y) &= \int_{-\infty}^{\infty}\int_{-\infty}^{\infty} h(x,y)e^{2\pi i(f'_x x + f'_y y)}e^{-2\pi i(f_x x + f_y y)}\, dx\, dy \\ &= \int_{-\infty}^{\infty}\int_{-\infty}^{\infty} h(x,y)e^{-2\pi i((f_x - f'_x)x + (f_y - f'_y)y)}\, dx\, dy \\ &= \mathcal{F}\{h\}(f_x - f'_x, f_y - f'_y) \end{aligned}, \tag{A.15}$$

with f'_x and f'_y the frequency shift in the f_x- and f_y-direction respectively.

The Kronecker product

The Kronecker product, $\otimes$, for a $m \times n$ matrix $\mathbf{A}$ and a $k \times l$ matrix $\mathbf{M}$ is defined as:

$$\mathbf{A} \otimes \mathbf{M} = \begin{pmatrix} a_{1,1}\mathbf{M} & \cdots & a_{1,n}\mathbf{M} \\ \vdots & \ddots & \vdots \\ a_{m,1}\mathbf{M} & \cdots & a_{m,n}\mathbf{M} \end{pmatrix}, \tag{A.16}$$

where $a_{i,j}$ is the entry in the i-th row and j-th column of $\mathbf{A}$ and the resulting matrix is $mk \times nl$.

The indicator function
The indicator function, $\mathbb{1}$, equals 1 if a condition is satisfied and 0 elsewhere. Let A be a set, then the indicator function that checks if an element, x, is contained in this set is defined as:

$$\mathbb{1}_A(x) = \begin{cases} 1 & \text{if} \quad x \in A \\ 0 & \text{if} \quad x \notin A \end{cases}. \tag{A.17}$$

The entry-wise L_p matrix norm
For a $m \times n$ matrix $\mathbf{A}$ the entry-wise L_p matrix norm can be defined as:

$$||\mathbf{A}||_p \coloneqq \left(\sum_i^m \sum_j^n |a_{i,j}|^p \right)^{\frac{1}{p}}. \tag{A.18}$$

For $p = 2$ this becomes the Frobenius norm:

$$||\mathbf{A}||_{\mathrm{F}} \coloneqq \sqrt{\sum_i^m \sum_j^n |a_{i,j}|^2}. \tag{A.19}$$

When considering the difference between two real matrices, $\mathbf{A}$ and $\mathbf{B}$, of equal dimension $m \times n$, then the Frobenius norm is related to the root-mean-square-error, RMSE, if all entries of matrix $\mathbf{B}$ should be approximated by the corresponding entry in $\mathbf{A}$:

$$\begin{aligned} ||\mathbf{A} - \mathbf{B}||_{\mathrm{F}} &= \sqrt{\sum_i^m \sum_j^n (a_{i,j} - b_{i,j})^2} \\ &= \sqrt{mn} \sqrt{\frac{1}{mn} \sum_i^m \sum_j^n (a_{i,j} - b_{i,j})^2} \\ &= \sqrt{mn}\, \mathrm{RMSE}(\mathbf{A}, \mathbf{B}). \end{aligned} \tag{A.20}$$

When using higher order tensors a generalization of the above norm can be used, where summations over additional indices are included. For $p = \infty$ the norm takes the maximum absolute value of all entries:

$$||\mathbf{A}||_{\max} = \max_{i,j} |a_{i,j}|. \tag{A.21}$$

B Previous model iterations

This appendix contains the algorithm pipelines of 4 previous model iterations called $\mathcal{M}_1$, $\mathcal{M}_2$, $\mathcal{M}_3$ and $\mathcal{M}_4$ in chronological order. The final model iteration, $\mathcal{M}$, succeeds $\mathcal{M}_4$ after the implementation of two speed up tricks and can be seen in Figure 5.6. The changes made between different iterations of the model either improved the accuracy or the speed of the model.

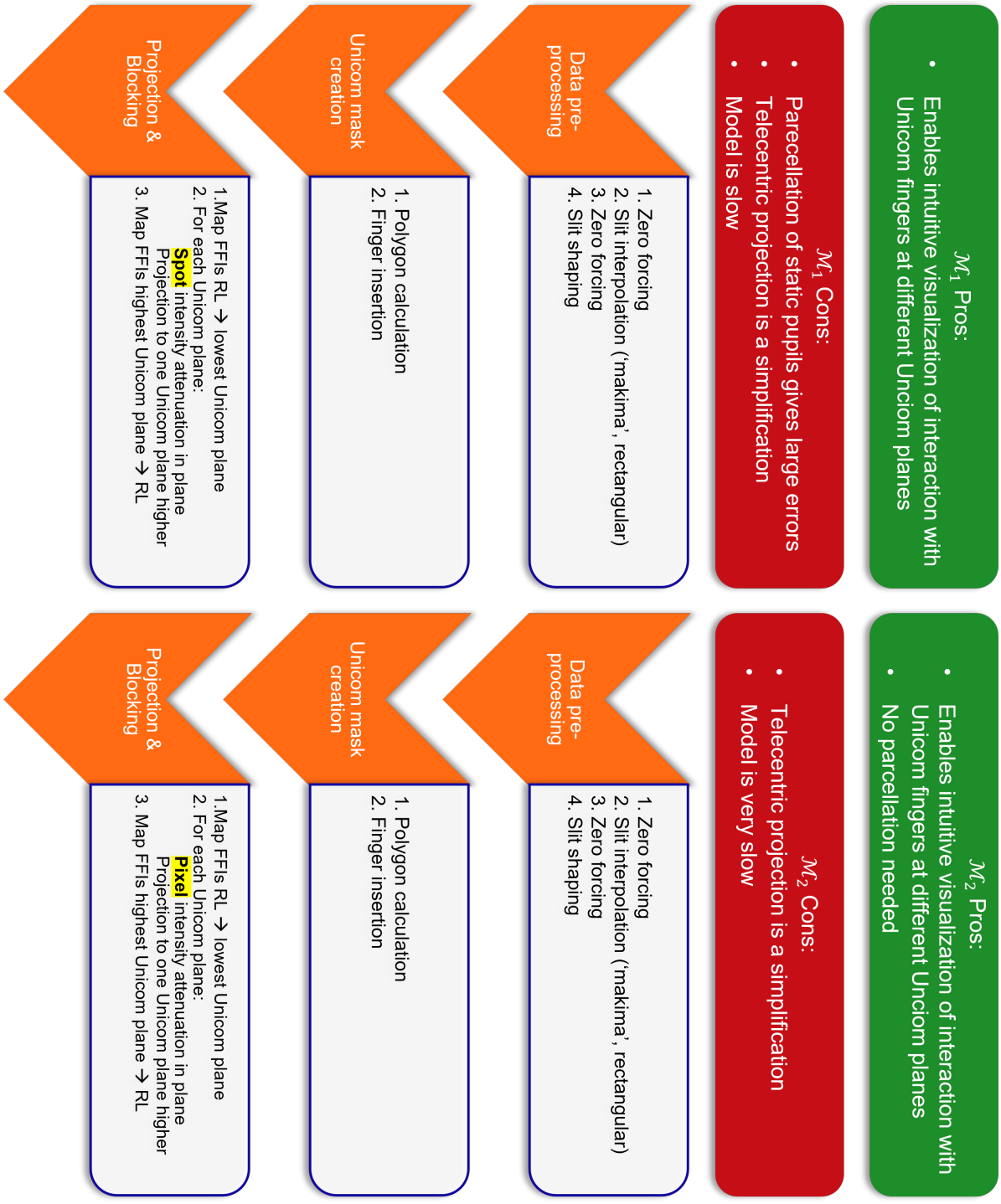

Fig. B.1: Algorithm pipelines of $\mathcal{M}_1$ and $\mathcal{M}_2$, changes are marked in yellow. Pros and cons of both model iterations are shown in the green and red boxes respectively.

In Figure B.1 the algorithm pipelines of $\mathcal{M}_1$ and $\mathcal{M}_2$ are shown. In $\mathcal{M}_1$ input data is assumed to

consist of parcellated static pupils, but parcellation is ill-suited for static pupils and thus introduces large errors into model predictions. Therefore, $\mathcal{M}_2$ works with the more accurate but more data dense static bitmap pupils instead. To speed up the model, $\mathcal{M}_3$ shown in Figure B.2 replaces calculating the blocking of light at each Unicom level with projecting the shadow of the Unicom onto RL. $\mathcal{M}_4$, also shown in Figure B.2, introduces realistic non-telecentric effects in the projection of shadows enabling better predictions. $\mathcal{M}$ improves upon $\mathcal{M}_4$ by adopting two speed up tricks.

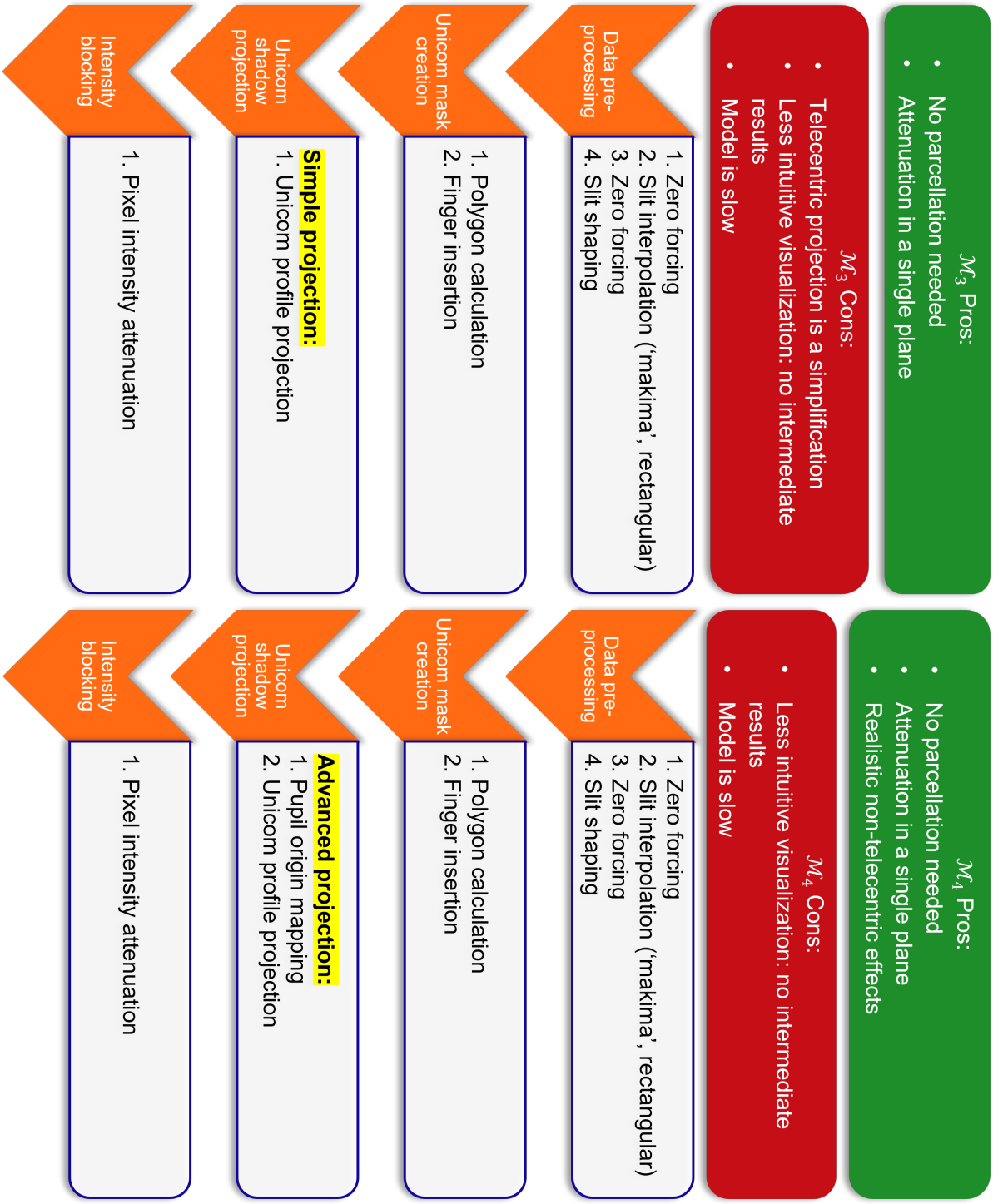

Fig. B.2: Algorithm pipelines of $\mathcal{M}_3$ and $\mathcal{M}_4$, changes are marked in yellow. Pros and cons of both model iterations are shown in the green and red boxes respectively.

C Pupil Predictor's Unicom implementation

Since Pupil Predictor is closed off software delivered by a supplier of ASML, the exact method used to account for the Unicom's effects in Pupil Predictor is unknown. However, even when considering Pupil Predictor as a black box model, by analyzing the output of Pupil Predictor for a couple of scenarios, an educated guess can be made as to how the effects of the Unicom were implemented. Because the Unicom is designed by ASML and its placement in the EUV machine depends on assembly by ASML, it is very likely that the supplier had limited knowledge of the geometrical properties of the Unicom.

The main predictions performed by Pupil Predictor include predictions of static pupils at any (x, y) position in the slit as well as scanning pupils for any x-position, both without taking the effects of the Unicom into account. Additionally, Pupil Predictor predicts scanning pupils if Unicom effects need to be considered and requires one input of a y-position of the Unicom finger per x-position for which scanning pupil predictions should be produced. Therefore, the author hypothesizes that Pupil Predictor assumes that at a certain x-position all light at RL is blocked in the part of the slit where the y-position is smaller than the supplied y-position of the Unicom finger. A simple implementation of this would be to pick the first ny-index associated to the blocked area on RL as the starting index of a numerical integration scheme similar to Equation 5.17. This would create a method to obtain scanning pupil predictions with inserted Unicom fingers from Pupil Predictor's static pupil predictions with extracted Unicom fingers. Such a method would not only be straightforward, but also be one of the few viable options when knowledge about the Unicom is limited.
To investigate if Pupil Predictor assumes the supplied y-position of the Unicom finger marks the boarder shaded area of the slit, the trapezoid method was used to first create a baseline result with extracted Unicom fingers and subsequently calculate a prediction with the Unicom fingers inserted until the middle of the slit in y-direction. In this investigation only the total intensity in the slit is of interest, hence scanning predictions are calculated from Pupil Predictor's static pupil predictions by summing the pupil intensity in the trapezoid method:

$$I^d_{nx} = \sum_{ny=ny^L(d)+1}^{Ny} (y_{ny} - y_{ny-1}) \frac{\sum_{i=1}^{N_{\sigma^x}} \sum_{j=1}^{N_{\sigma^y}} \left(\mathbb{I}^{p\mathbf{0}}_{i,j,nx,ny-1} + \mathbb{I}^{p\mathbf{0}}_{i,j,nx,ny} \right)}{2}, \tag{C.1}$$

where I^d_{nx} is the numerically integrated slit intensity at the x-position corresponding to index nx, d is the y-position of the Unicom finger supplied to Pupil Predictor, $ny^L(d)$ is the highest ny-index belonging to a y-position with a y-value lower than the supplied value for d and the $\mathbb{I}^{p\mathbf{0}}_{i,j,nx,ny}$s are the intensities predicted by Pupil Predictor for static pupils with extracted Unicom fingers. The baseline was calculated by simply setting $ny^L(d)$ to 1 in Equation C.1 such that the resulting intensity I^0_{nx} is obtained by numerically integrating Pupil Predictor's static pupil predictions through the entire slit in the y-direction for a fixed x-position.

Since Pupil predictor is a black box model it is not possible to be sure about the width of the slit in y-direction that it considers during calculations. Therefore, the assumption was made that Pupil Predictor uses the entire width of the slit for which it calculates static pupils in its calculations of scanning pupils. The investigation accounted for this uncertain slit width, by using the output of Pupil Predictor for y-values up to 2 times the width of the design slit away from the middle of the slit in y-direction.

In Figure C.1, for a single pupil, the y-integrated slit profile for extracted Unicom fingers calculated using Equation C.1 and subsequently multiplying by 100, is compared to the slit profile obtained by summing the spot intensities of scanning pupil predictions by Pupil Predictor. The scanning pupil predictions were obtained by supplying Pupil Predictor with a y-position of the Unicom finger that extracts the Unicom finger by a distance of 10 times the width of the slit. Multiplication by 100 of the result obtained with Equation C.1 was empirically determined to match the obtained slit profiles for every available pupil in Pupil Predictor to the scanning predictions by Pupil Predictor. This multiplication might be needed due to conversion of results in Pupil Predictor to standard SI units. The x-axis in both plots display the x-coordinates as a fraction of the nominal length of the slit in x-direction used for illumination in EUV machine.

The difference between Figure C.1a and Figure C.1b, which is of the order 10^{-5}, is shown in Figure C.2. ΔI is calculated by subtracting the Pupil Predictor profile from the profile found by using Equation C.1. Although the difference is non-zero, the difference fluctuates around zero for the portion

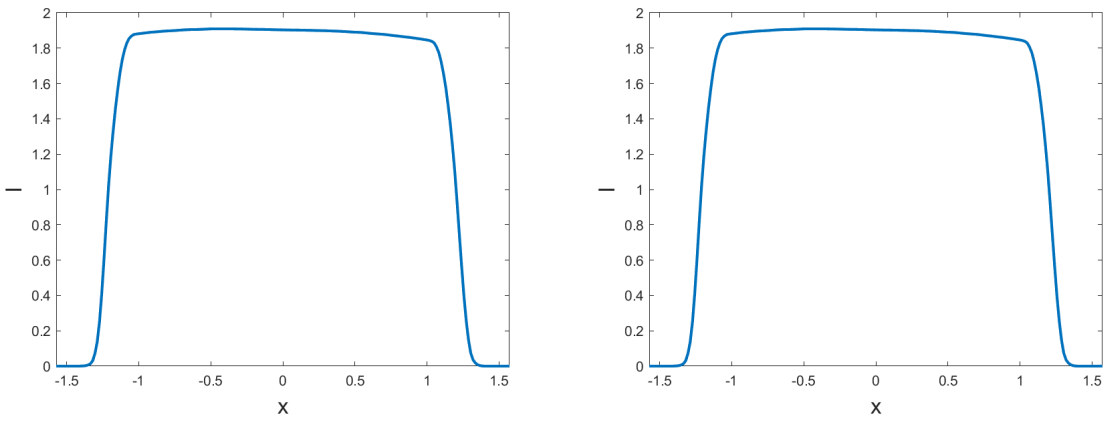

(a) Numerical integration. **(b)** Pupil Predictor.

Fig. C.1: y-integrated slit intensity profiles with extracted Unicom fingers predicted by numerically integrating Pupil Predictor's static pupil predictions (a) and directly predicted by Pupil Predictor (b). The x-axes are normalized to the size of the nominal illumination slit.

of the slit used for illumination. Only at the x-edges of the slit where the intensity profiles drop to zero some large differences occur. These large differences are likely due to artifacts in the calculations by Pupil Predictor for (x, y)-coordinates that are usually outside of the interesting portion of the slit for real applications. Thus, using Equation C.1 does not produce a perfect match to the internal calculations by Pupil Predictor to predict scanning results, but this method does provide a match of up to order 10^{-6} for the largest part of the slit.

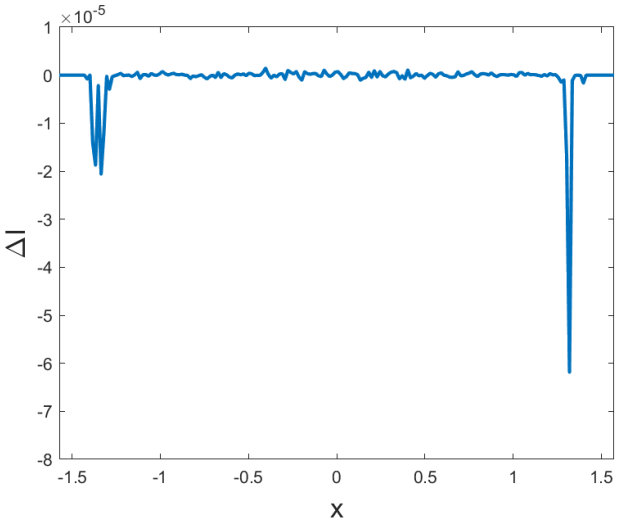

Fig. C.2: ΔI: the y-integrated slit profile with Unicom fingers fully extracted, predicted by using numerical integration minus the slit profile predicted directly by Pupil Predictor. The x-axis is normalized to the size of the nominal illumination slit.

With the baseline of the difference between the numerically integrated static pupil predictions and the scanning predictions by Pupil Predictor, the implementation of the Unicom in Pupil Predictor can be investigated further. If the hypothesis about the implementation of the Unicom is correct, supplying a value for d to Pupil Predictor that inserts the fingers until the middle of the slit and changing $ny^L(d)$ in Equation C.1 accordingly should result in two predictions with a difference of the same order of magnitude as previously obtained for $d = 0$. In case this difference stays roughly constant when accounting for the Unicom, the remaining difference is likely still caused by the choice of numerical

integration scheme in combination with a mismatch in which grid-points are used for the numerical integration and by Pupil Predictor internally.

In Figure C.3 the y-integrated slit profiles for Unicom fingers inserted until the middle of the slit are shown. Care was taken to account for the CRAO by shifting the slit produced by Pupil Predictor by $\tan(\text{CRAO})(z^{RL} - z^{UL})$.

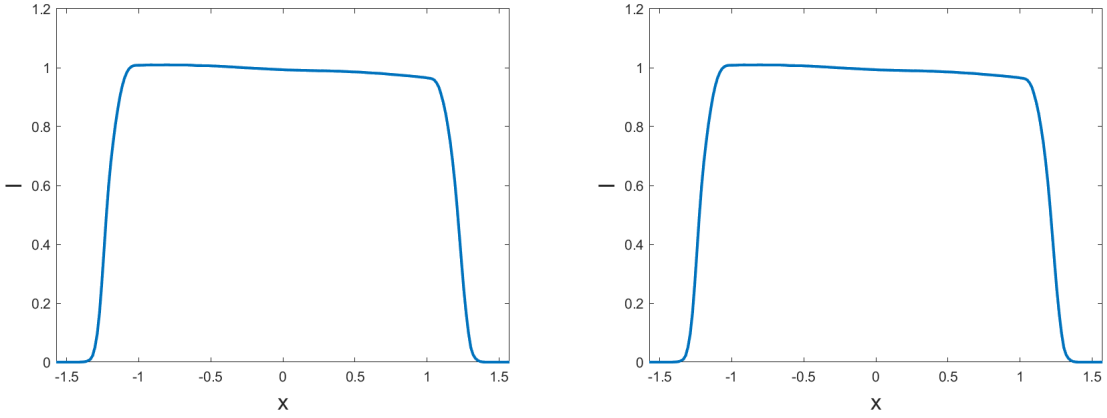

(a) Numeric integration. **(b)** Pupil Predictor.

Fig. C.3: y-integrated slit intensity profiles with Unicom fingers inserted until the middle of the slit, predicted by numerically integrating Pupil Predictor's static pupil predictions (a) and directly predicted by Pupil Predictor (b). The x-axes are normalized to the size of the nominal illumination slit.

The difference between Figure C.3a and Figure C.3b is shown in Figure C.4. ΔI is calculated by subtracting the Pupil Predictor profile from the profile found by using Equation C.1. Again for the part of the slit used for illumination, the difference has order of magnitude 10^{-6} and the same differences at the edge of the slit of order of magnitude 10^{-5} still remain. ΔI in Figure C.4 and ΔI in Figure C.2 are not completely identical. However, the small differences are well within the order of magnitude of ΔI in Figure C.2, thus the hypothesis about the way the Unicom is implemented in Pupil Predictor seems account for the output of Pupil Predictor quite well.

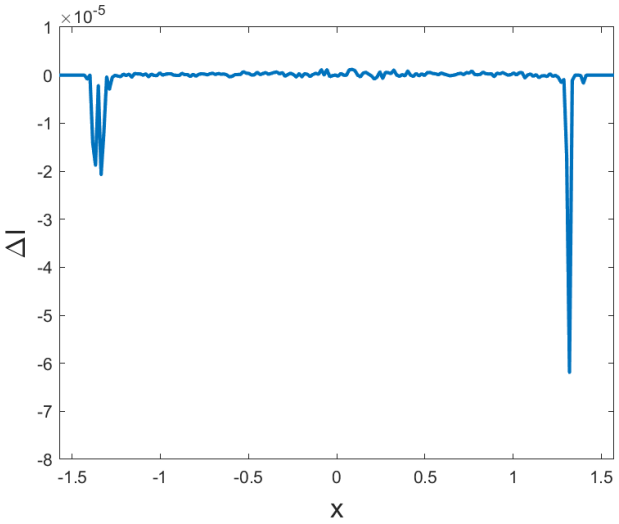

Fig. C.4: ΔI, the y-integrated slit profile with Unicom fingers inserted until the middle of the slit, predicted by using numerical integration minus the slit profile predicted directly by Pupil Predictor. The x-axis is normalized to the size of the nominal illumination slit.

An implementation of the Unicom in a model based on supplying a y-position of a Unicom finger for

each x-position in the slit, which is directly used as the boarder of the blocked part of the slit on RL is straightforward but it has some limitations. All limitations stem from the fact that the Unicom fingers are not 2D and situated at RL but instead 3D and located at two different planes around UL. Therefore, to accurately account for the projection of the Unicom fingers onto RL a ray-tracing based model would be needed to map the actual profile of the Unicom fingers to RL. Additionally, even if the projection of the Unicom profiles onto RL would be available, the model would not be able to account for the effects of the Unicom on pupils and would predict discrete blocking of intensity at the transition of the shaded area of the slit, whereas in reality a gradual change would be observed.